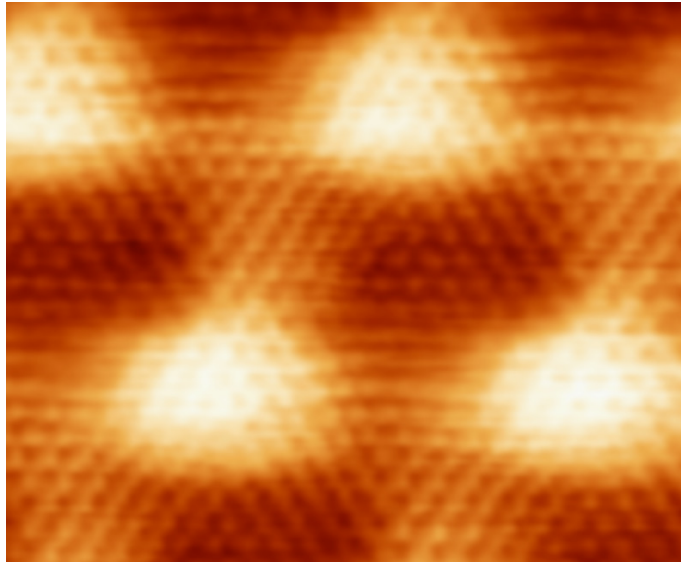


---

**Scanning Tunneling Microscopy and Spectroscopy  
investigations of  
Graphene on Ru(0001) and (CO+O) on Rh(111)**

---



Fakultät für Chemie und Pharmazie  
Ludwig-Maximilians-Universität München

Stefano Marchini

2007

Dissertation zur Erlangung des Doktorgrades  
Der Fakultät für Chemie und Pharmazie  
Der Ludwig-Maximilians-Universität München

Scanning Tunneling Microscopy and Spectroscopy investigations  
of graphene on Ru(0001) and (CO+O) on Rh(111)

Stefano Marchini

aus

Casalmaggiore (Italien)

2007

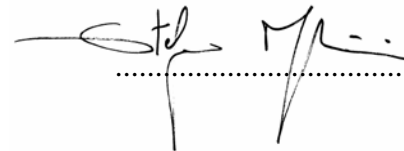
## Erklärung

Diese Dissertation wurde im Sinne von § 13 Abs. 3 bzw. 4 der Promotionsordnung vom 29. Januar 1998 von Herrn Prof. Dr. Joost Winterlin betreut.

## Ehrenwörtliche Versicherung

Diese Dissertation wurde selbständig, ohne unerlaubte Hilfe erarbeitet.

München, am 06 August 2007



Dissertation eingerichtet am 07 August 2007

1. Gutachter Prof. Dr. Joost Winterlin
2. Gutachter Prof. Dr. A. Hartschuh

Mündliche Prüfung am 23 Oktober 2007

Ai miei genitori



# Index

<b>Introduction</b>	<b>1</b>
<b>Chapter 1</b>	
<b>Introduction to Scanning Tunneling Microscopy and Spectroscopy</b>	<b>7</b>
1.1 Scanning Tunneling Microscopy .....	7
1.2 Voltage dependent images .....	10
1.3 Scanning Tunneling Spectroscopy .....	11
<b>Chapter 2</b>	
<b>Experimental setup</b>	<b>15</b>
2.1 The UHV chamber .....	15
2.2 Scanning Tunneling Spectroscopy .....	16
2.2.1 Setup .....	17
2.2.2 Noise problem .....	20
2.2.3 Data analysis .....	22
<b>Chapter 3</b>	
<b>Graphene on Ru(0001)</b>	<b>27</b>
3.1 The Ru(0001) surface and the sample preparation procedure .....	27
3.2 Graphene .....	31
3.2.1 Formation of the ordered superstructure .....	31
3.2.2 Identification of the chemical species responsible for the formation of the superstructure .....	33
3.2.3 Geometry of the superstructure .....	38
I Partial coverage .....	38
II Total coverage .....	40
III Atomic structure of the graphene layer .....	42
IV The two different C atoms in the graphene unit cell ..	49
V The corrugation of the moiré .....	53
VI Discussion .....	55
3.2.4 Electronic Structure .....	56
I Voltage dependent images .....	56
II Scanning tunneling spectroscopy measurements .....	60
IIa Graphene versus metal .....	60
IIb STS at different locations of the graphene layer	63
III Decay length .....	65

3.3 Gold deposition .....	72
3.3.1 Evaporator .....	73
3.3.2 Gold on clean ruthenium .....	75
3.3.3 Gold on the surface partially covered with graphene .....	76
<b>Chapter 4</b>	
<b>CO poisoning of O/Rh(111)</b>	<b>81</b>
4.1 Oxygen saturation coverage of Rh(111): 0.25 or 0.5 ML? .....	81
4.2 The Rh(111) surface and the sample preparation procedure .....	83
4.3 (2x1) and (2x2) oxygen structures .....	84
4.4 Oxygen adsorption in the presence of contaminants .....	88
4.5 Discussion .....	93
4.6 Conclusion .....	93
<b>Conclusions and outlook</b>	<b>95</b>
<b>Appendix A</b>	
Ru(0001) contamination at low temperature: the “gray atoms” .....	99
<b>References</b>	<b>109</b>

---

## Acronyms and symbols

ADC	Analog to Digital Converter
AES	Auger Electron Spectroscopy
CDW	Charge Density Waves
CITS	Current Imaging Tunneling Spectroscopy
DAC	Digital to Analog Converter
DFT	Density Functional Theory
fcc	face centered cubic
hcp	hexagonal closed packed
HREELS	High Resolution Electron Energy Loss Spectroscopy
LEED	Low Energy Electron Diffraction
QMS	Quadrupole Mass Spectrometer
STM	Scanning Tunneling Microscopy
STS	Scanning Tunneling Spectroscopy
TDS	Thermal Desorption Spectroscopy
UHV	Ultra High Vacuum
UPS	Ultraviolet Photoelectron Spectroscopy
XPS	X-ray Photoelectron Spectroscopy
$E_F$	Fermi Energy
$I_t$	Tunneling current
$K$	Inverse decay length
$\vec{k}_{//}$	Wave vector component parallel to the tunneling junction
ML	Monolayer, 1 ML = one adsorbate per one substrate atom
U	Tunneling voltage
$\Theta$	Coverage, number of adsorbates per unit cell
$\Phi$	Work function
Å	Ångström, 1 Å = 0.1 nm = $10^{-10}$ m
e	Electron charge, $e = -1.602176487 \cdot 10^{-19}$ C
eV	Electronvolt, 1 eV = $1.602176487 \cdot 10^{-19}$ J
ħ	Reduced Plank constant, $\hbar = 1.054571628 \cdot 10^{-34}$ J·s = $6.5821189 \cdot 10^{-16}$ eV·s
L	Langmuir, 1 L = $1 \cdot 10^{-6}$ Torr·s
m	Electron mass, $m = 9.1093826 \cdot 10^{-31}$ Kg

---

## Elements properties

**Ruthenium** Atomic number 44

Electronic configuration [Kr]4d<sup>7</sup>5s<sup>1</sup>

Lattice constant  $a_{\text{Ru}} = 2.706 \text{ \AA}$ ,  $c_{\text{Ru}} = 4.282 \text{ \AA}$ , hcp

Melting point 2607 K

Ru(0001) surface Lattice constant  $a = 2.706 \text{ \AA}$

$$\text{Steps height } h = \frac{c_{\text{Ru}}}{2} = 2.141 \text{ \AA}$$

$$1 \text{ ML} = 1.57 \cdot 10^{15} \frac{\text{atoms}}{\text{cm}^2}$$

**Carbon** Atomic number 6

Electronic configuration 1s<sup>2</sup>2s<sup>2</sup>2p<sup>2</sup>

Graphite Lattice constant  $a_{\text{graphite}} = 2.464 \text{ \AA}$ ,  $c_{\text{graphite}} = 6.711 \text{ \AA}$

$$\text{Interlayer distance} = \frac{c_{\text{graphite}}}{2} = 3.355 \text{ \AA}$$

Graphene Lattice constant  $a = 2.464 \text{ \AA}$

$$\text{C-C distance} = \frac{\sqrt{3}}{3} a = 1.422 \text{ \AA}$$

**Rhodium** Atomic number 45

Electronic configuration [Kr]4d<sup>8</sup>5s<sup>1</sup>

Lattice constant  $a_{\text{Rh}} = 3.803 \text{ \AA}$ , fcc

Melting point 2237 K

Rh(111) surface Lattice constant  $a = \frac{\sqrt{2}}{2} a_{\text{Rh}} = 2.689 \text{ \AA}$

$$1 \text{ ML} = 1.60 \cdot 10^{15} \frac{\text{atoms}}{\text{cm}^2}$$





## **Introduction**

One of the major problems related to the operation of heterogeneous catalysis is the catalyst loss of activity over time, usually referred to as “deactivation”. This process is both of chemical and physical nature and it occurs simultaneously with the main reaction. Deactivation is inevitable, all catalysts decay over time, but it is possible to slow down the process or to find operating conditions that minimize its effects. For this reason it is of primary importance to investigate the fundamental chemical and physical aspects of catalyst deactivation in order to design deactivation-resistant catalysts, to operate industrial chemical reactors in optimum conditions and to establish effective reactivating procedures.

Deactivation occurs by a number of different mechanisms commonly divided into four classes: poisoning, coking, sintering and phase transformation.

Sintering and phase transformation are processes of physical nature, and are generally thermally activated. Phase transformation is a phase transition from a certain crystalline phase into a different one while sintering is a general structural modification of the catalyst.

Poisoning is the loss of activity due to the strong chemisorption of chemical species on sites usually available for catalysis. The effects of poisoning species may be of geometrical or electronic nature. Geometrical effects consist for example in physically blocking the active sites, inducing the reconstruction of the catalyst surface, hindering the diffusion of adsorbed reactants or preventing adsorbate species from interacting with

each other. On the other hand, since the poisoning species is strongly bonded to the substrate, it may modify the electronic structure of several atoms of the catalyst, thereby changing their ability to adsorb or dissociate reactant molecules.

Coking refers in particular to the formation of carbonaceous residues covering the active surface of the catalysts employed for reactions involving hydrocarbons or carbon oxides. The chemical nature of the carbonaceous deposits depends on several parameters, such as pressure, temperature and chemical state of the catalyst but in general it is possible to distinguish between adsorbed atomic carbon, usually reactive, amorphous carbon, carbidic carbon and finally the unreactive crystalline graphitic carbon.

Figure I.1 displays an electron micrograph of a Ni catalyst having undergone extensive carbon deposition during CO disproportionation at 673 K [1].

The question we focused our attention on is: what happens at the atomic level when carbon deposition on an active catalyst surface occurs?

The Scanning Tunneling Microscopy (STM) technique is ideal to investigate surface processes on an atomic level and two model systems were chosen.

The first system selected is the formation of a graphitic layer on the Ru(0001) surface.

Ruthenium is a transition metal of the platinum group and, because of its high catalytic activity, it is used as catalyst for several reactions, for instance for the production of ammonia from natural gas [2], for the production of acetic acid from methanol [3] and in the removal of H<sub>2</sub>S from oil refineries and from other industrial processes [4]. For this reason it has been also widely studied from the fundamental point of view in the field of surface physics and in particular the (0001) surface has been the subject of countless works. It is surprising, though, that, although many studies were focused on the activity and the reaction mechanisms of several processes catalyzed by the ruthenium surface, only few sporadic works deal with the fundamental aspects of poisoning and deactivation of this catalyst.

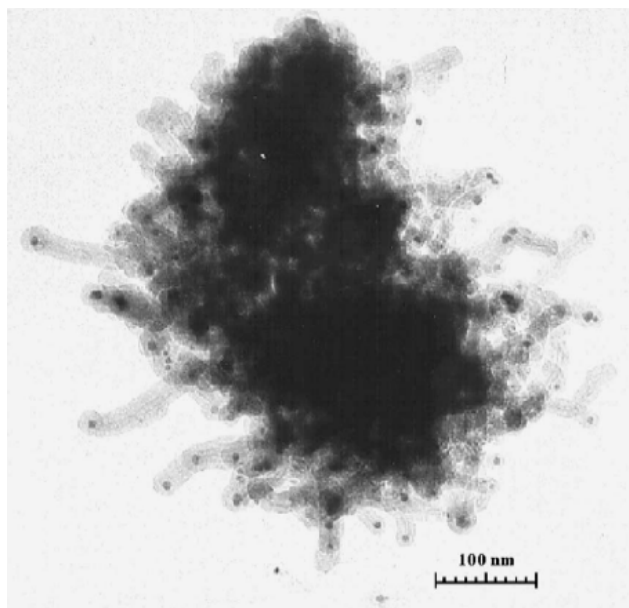


**Figure I.1:** Electron micrograph of 14% Ni/Al<sub>2</sub>O<sub>3</sub> having undergone extensive carbon deposition during CO disproportionation at 673 K (from reference [1]).

The second system is a typical example of undesired poisoning effects by unintentional adsorption of foreign chemical species even in ultra high vacuum. The system investigated is the (111) surface of rhodium with a particular focus on the adsorption of oxygen, one of the typical model systems thoroughly investigated in surface science. Also in this case, systematic investigations of poisoning and deactivation effects are lacking. In this work it will be shown that the unintended adsorption of CO molecules in ultra high vacuum strongly modifies not only the geometrical structure of the O/Rh(111) system, but also its reactivity with respect to the reduction by hydrogen.

Studying the graphitic formation on the Ru(0001) surface has “naturally” led to one of the “hot topics” of solid state physics of the last few years: graphene.

Graphene is a single layer of carbon in the graphitic form and, as a two-dimensional form of carbon, it places itself in the relevant group of carbon allotropes. Surprisingly, while the three dimensional allotropes graphite and diamond have been known since ancient times and the one dimensional nanotubes [5] and the zero dimensional fullerenes [6] have been discovered some 10-20 years ago, graphene as a two dimensional crystal could only be detected in a free state in 2004 [7]. Since then, several groups have tried to study its exceptional electronic [8] and structural [9] properties aiming generally to the application of graphene as basic constituent for a new generation of electronic devices [10]. The main problem connected with the use of graphene remains nonetheless the synthesis of large graphene crystals. The first attempts to isolate graphene consisted in micromechanical cleavage from three-dimensional graphite, but this procedure often results in the deposition of more than a single layer of graphite [11]. A promising approach not yet attempted may be the use of graphene epitaxy on catalytic surfaces followed by deposition of an insulating support on top of graphene and chemical removal of the primary metallic substrate. In this respect, the system consisting of graphene epitaxially grown on the Ru(0001) surface as described in chapter 3 of this work is an ideal candidate because of its structural homogeneity over large areas of the sample and of its high stability under ambient conditions.

Finally, the system consisting of graphene grown on Ru(0001) opens new opportunities in the field of nanotechnology.

In the last few years this field has seen a fast development due to the improvement of several techniques suitable to engineering of nanostructures [12]. There are basically two approaches to nanoengineering: the top-down and the bottom-up approach. The top down approach is based on lithography techniques and consists in shaping objects on a nanometer scale starting from bigger amounts of material [13]. The main limit in this approach is the lateral resolution achievable which, nowadays, is about 100 nm and can be reduced only using photolithography with synchrotron radiation, noticeably increasing the costs [14]. The bottom up approach, on the other hand, overcomes this problem taking advantage of the self-assembly properties of atoms and molecules to create functional molecules and nano-objects. One of the possible ways to drive the assembling of atoms and molecules is by using nanotemplates consisting of nanostructured surfaces with a periodicity on the nanometre scale.

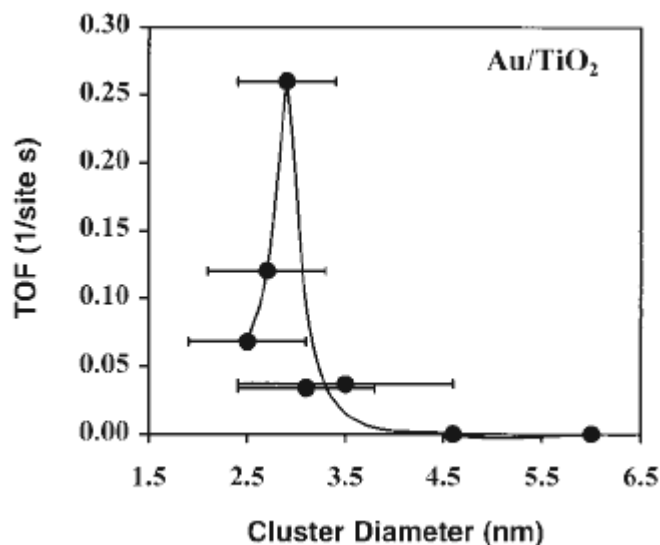


**Figure I.2:** CO oxidation turnover frequencies at 300 K as a function of the average size of the Au clusters supported on a high surface area TiO<sub>2</sub> support (from reference [15]).

This approach has been used for instance in the study of systems suitable for high density data storage. Weiss and co-workers have deposited Co on a stepped gold surface using the periodic pattern formed by the gold steps as a template for growing superlattices of cobalt particles in order to explore the ultimate density limit of magnetic recording [16]. Nanotemplates could play a crucial role also in the field of catalysis. Valden and co-workers have shown that the turnover frequency of CO oxidation by gold particles deposited on a TiO<sub>2</sub> support is dependent on the particles size and displays, in particular, a pronounced maximum for particles with a diameter of 2.7 nm (figure I.2) [15]. Size-dependent activity is a frequent observed – but little understood – effect in heterogeneous catalysis, and catalysis by gold is an extreme example of this effect. For this reason it would be desirable to have a template that allows one to grow Au nanoparticles with controlled sizes and in large arrays in order to obtain a macroscopic catalyst with microscopically defined structure. An ideal nanotemplate for this purpose must fulfil a series of properties: relatively easy preparation procedure, regular nanometer periodicity over large areas, stability under operating conditions and chemical inertness. For these reasons, the system consisting of a graphene layer deposited on the Ru(0001) surface will be shown to be an ideal candidate, and the first preliminary results of gold deposition on this system will be presented.





## **Chapter 1**

### **Introduction to Scanning Tunneling Microscopy and Spectroscopy**

The aim of this chapter is to describe the theoretical background behind the Scanning Tunneling Microscopy (STM) technique with particular emphasis on the spectroscopic effects in the STM images and the related Scanning Tunneling Spectroscopy (STS) technique.

#### **1.1 Scanning Tunneling Microscopy**

The physical phenomena behind the STM technique is the tunneling effect, a quantum mechanical process that accounts for the possibility for particles, in this case electrons, to overcome a potential barrier that would be “classically” forbidden. In the one dimensional case (spatial variable  $z$ ), the wave function of an electron in such a barrier is given by:

$$\Psi(z) = \Psi(0)e^{-Kz} \tag{1}$$

$K$ , the inverse decay length, is defined by the expression:

$$K = \sqrt{\frac{2m(V_B - E)}{\hbar^2}} \quad (2)$$

where  $m$  is the electron mass,  $V_B$  the potential barrier height,  $E$  the electron energy and  $\hbar$  the reduced Plank constant.

The transmission probability, which is proportional to the tunneling current, is given by the square of the wave function, thus:

$$I \propto e^{-2Kz} \quad (3)$$

This shows that the electron has a non vanishing probability to cross the potential barrier giving rise to a tunneling current decaying exponentially with the distance  $z$ .

The STM technique employs this dependence to obtain atomic resolved images of conducting or semi-conducting surfaces [17].

In this case a metallic tip (in general made of Pt-Ir or, as in our case, of W) is approached to the surface at a distance of few Angstroms, and a constant bias voltage  $U$  is applied between the two electrodes. This gives rise to a continuous tunneling current flowing from the electrode at negative voltage to the electrode at positive voltage as schematically shown in figure 1.1 [18].

The general expression for the tunneling current is [19]:

$$I_t = \frac{2\pi e}{\hbar} \sum_{\mu, \nu} \{f(E_\mu)[1 - f(E_\nu + eU)] - f(E_\nu + eU)[1 - f(E_\mu)]\} |M_{\mu, \nu}|^2 \delta(E_\nu - E_\mu) \quad (4)$$

where  $f(E)$  is the Fermi function,  $U$  is the applied voltage,  $M_{\mu, \nu}$  is the tunneling matrix element between the states  $\Psi_\mu$  of the tip and  $\Psi_\nu$  of the sample and  $E_\mu$  and  $E_\nu$  are their energies.

Applying the Bardeen formalism [20] for calculating  $M_{\mu, \nu}$  and describing the tip's states simply as s-states, Tersoff and Hamann [21, 22] showed that this expression, in the limits of low temperature and low applied voltage, becomes:

$$I_t \propto U \cdot \rho_s(E_F, z) \cdot e^{-2Kz} \quad (5)$$

with  $\rho_s(E_F, z)$  representing the density of states of the sample at the Fermi level at the position  $z$  of the tip in front of the surface.

$K$  is the inverse decay length and, in analogy with the one dimensional case (2), is defined by:

$$K = \sqrt{\frac{2m\Phi}{\hbar^2}} \quad (6)$$

where  $\Phi$  is the effective local potential barrier height.

In the general 3D treatment of the tunneling effect, it is necessary to consider not only the total energy  $E$  of the tunneling electron but also the wave vector component  $\vec{k}_{||}$  parallel to the tunneling junction (i.e. parallel to the sample surface) which is conserved in the tunneling process. In this case the general expression of the tunneling current is characterized by an inverse decay length  $K$  given by:

$$K = \sqrt{\frac{2m\phi}{\hbar^2} + k_{||}^2} \quad (7)$$

This means that states with non zero  $\vec{k}_{||}$  decay more strongly in the tunneling barrier and the states with  $\vec{k}_{||} = \vec{0}$  dominate the tunneling current. Only if there are no states with  $\vec{k}_{||} = \vec{0}$  it is possible to observe tunneling from states with large  $\vec{k}_{||}$ .

Equation (5) shows that the images obtained by STM represent a convolution of topographic and electronic effects and their interpretation is thus not straightforward.

Typically, the STM experiments are performed scanning the tip over a sample area and adjusting the tip-sample distance with a feedback loop in order to keep the tunneling current constant: this means that the STM images show the contour of constant density of states (given that  $\Phi$  does not vary).

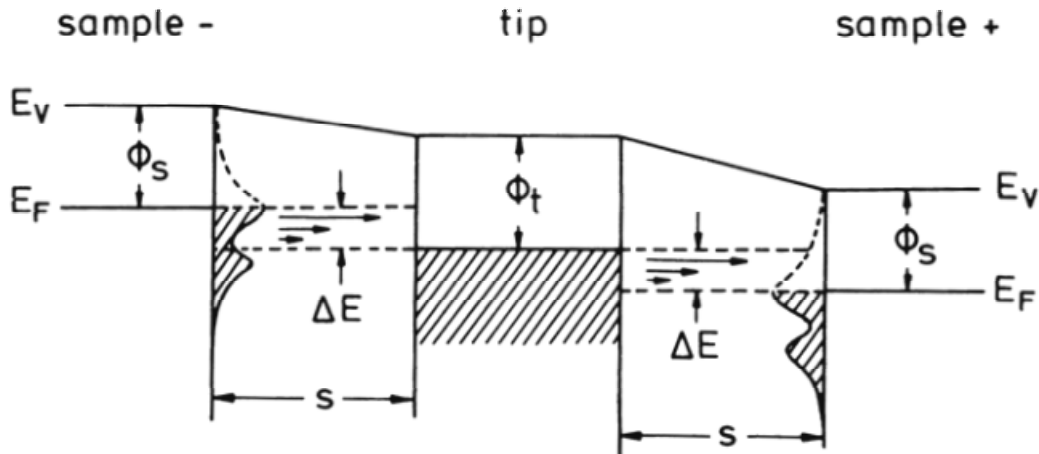


**Figure 1.1** Schematic representation of the tunneling process between sample and tip from ref. [18].

## 1.2 Voltage dependent images

Figure 1.1 [18] illustrates schematically the tunneling process between sample and tip. The density of states of the sample is structured while the tip is assumed to have a constant density of states. The bias voltage  $U$  (indicated in the figure as  $\Delta E$ ) determines an energy window whose states contribute to the tunneling current. The lengths of the arrows show schematically that the states with higher energy have the longest decay length into the vacuum, and are mainly responsible for the tunneling current. When the sample is at a negative voltage compared to the tip, the electrons tunnel from the occupied states of the sample to the tip and the STM measurement is a map of these states. On the contrary, when the sample is at a positive voltage, the electrons of the tip tunnel into the empty states of the sample.

The possibility to measure the empty or the filled states of a sample sometimes results in interesting inversion contrast phenomena in the STM images as shown in figure 1.2 [23]. The two images display the same area of a Si(001) surface measured with opposite bias voltages and showing atomic resolution. The surface has a (2x1) unit cell consisting of pairs of silicon atoms as schematically shown between the two images. The image on the left side is measured with a negative bias voltage, revealing thus the filled states of the sample, and shows bean-shaped structures forming rows separated by deep minima: each structure corresponds to a silicon dimer. On the contrary, the image on the right, measured with positive bias voltage, displays a weak minimum between the dimer rows and a deep minimum between the pairs of atoms forming the dimers. These differences, showing a spatial separation of the filled and empty electronic states of the surface, could be understood considering the electronic structure of the system. The occupied  $\pi$  bonding states lie below the Fermi energy and have a high electron density above the Si-Si bonds. On the contrary, the empty  $\pi^*$  antibonding states, lying above the Fermi energy, have a node in the wave function at the centre of the dimer bond, and this node is responsible for the minima between the pairs of atoms measured at positive voltage.

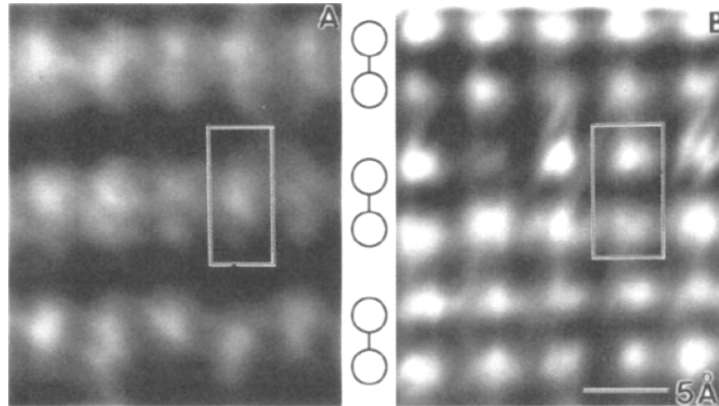


**Figure 1.2:** Constant current STM image of Si(001) at a) negative ( $-1.6$  V) and b) positive ( $+1.6$  V) bias voltage. The (2x1) unit cell is outlined and the relative locations of the dimers are shown in the centre (From ref. [23]).

In this example the electronic structure of the system could be clearly understood considering the STM images but often, and also in the present work, separating the contributions of electronic and geometric structure in the STM images is not straightforward. Typically, the presence of contrast inversion phenomena when measuring the topography with different bias voltages reveals the presence of a complex surface electronic structure that can be investigated with the Scanning Tunneling Spectroscopy technique.

### 1.3 Scanning Tunneling Spectroscopy

Scanning Tunneling Spectroscopy measurements consist in measuring the tunneling current  $I$  as a function of the bias voltage  $V$  applied between tip and sample.

The tunneling current can be expressed as:

$$I(V) = \int_0^{eV} \rho_S(r, E) \rho_T(r, E - V) T(E, eV, r) dE \quad (8)$$

with  $\rho_S$  and  $\rho_T$  the density of states of sample and tip respectively, and  $T$  the transmission probability [24].

Keeping the tip density of states  $\rho_T$  constant and taking the first derivative of (8) with respect to the bias voltage  $V$ :

$$\frac{dI}{dV} = e\rho_T\rho_S(r, eV)T(eV, eV, r) + \int_0^{eV} \rho_S(r, E)\rho_T \frac{dT(E, eV, r)}{dV} dE \quad (9)$$

The constant  $\rho_T$  can be justified for a clean, metallic tip, for which the tunneling current is dominated by s states (because of their stronger contraction d states contribute much less).

The first term in equation (9) is directly proportional to the density of states of the sample, the second term contains the voltage and position dependence of the transmission probability.

At any fixed location  $r$  the transmission factor  $T$  increases monotonically with  $V$  and the contribution of the second term in (9) is then a smoothly varying “background” on which the spectroscopic information is superimposed. Because the increase is smooth and monotonic, structures in  $dI/dV$  as a function of  $V$  can be assigned at a first approximation to changes in the density of states of the sample via the first term.

Equation (9) shows then that from a qualitative point of view the  $dI/dV$  curves give information about the sample density of states and in particular about the presence of local electronic structures and relevant changes.

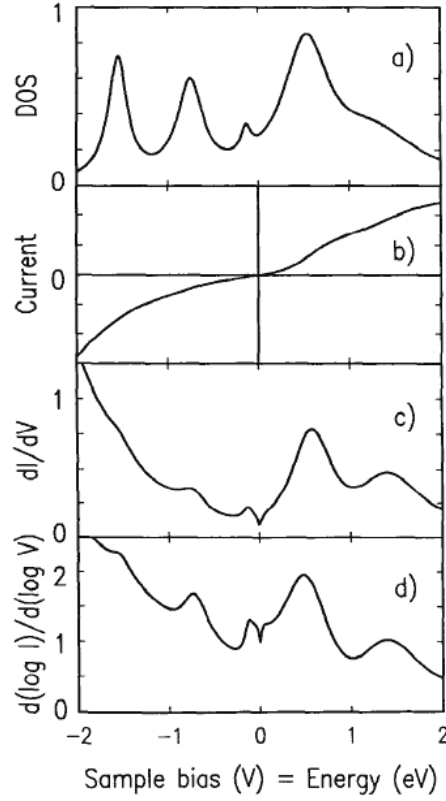


**Figure 1.3:** Numerical simulation of a tunneling  $I$ - $V$  spectrum and normalized results. *a)* Original density of states function. *b)* Tunneling  $I$ - $V$  curve calculated by numerical integration of tunneling equations. *c)* First derivative spectrum. *d)* Normalized derivative spectrum (From ref. [23]).

Extracting quantitative information, though, is more critical and the contribution of the second term in equation (9) and in particular its dependence on the bias voltage and on the position  $r$  must be taken into account.

Feenstra and coworkers have worked on this problem normalizing  $dI/dV$  to the conductance  $I/V$  of the tunneling junction [25]:

$$\frac{dI/dV}{I/V} = \frac{\rho_T \rho_S(r, eV) + \int_0^{eV} \frac{\rho_T \rho_S(r, E)}{T(eV, eV, r)} \frac{d}{d(eV)} [T(E, eV, r)] dE}{\frac{1}{eV} \int_0^{eV} \rho_T \rho_S(r, E) \frac{T(E, eV, r)}{T(eV, eV, r)} dE} \quad (10)$$

Since  $T(E, eV, r)$  and  $T(eV, eV, r)$  appear as ratios in equation (10), their exponential dependences on  $r$  and  $V$  tend to cancel. For positive bias voltages ( $V > 0$ ),  $T(E, eV) \leq T(eV, eV)$  and the maximum transmission occurs at  $E = eV$ . In this case the normalized

curves show the sample density of states together with a slowly varying background. For negative voltages,  $T(E, eV) \geq T(eV, eV)$  and the maximum transmission occurs at  $E = 0$ . In this case the background term at the numerator in (10) has the same order of magnitude as the denominator and they are both larger than the density of states by a factor of  $T(0, eV)/T(eV, eV)$ . The measure of the density of states is thus reduced by this factor and it should be difficult to observe low-lying occupied surface states.

Figure 1.3 shows the results of a numerical simulation of an I-V spectrum [23]. An “artificial” density of states (a) is considered to obtain the I-V curve in (b) according to the Bardeen formalism and considering the density of states of the tip constant. The first derivative  $dI/dV$  of the current in (b) shows the presence of structures (c) but, compared to the density of states in (a) reveals a lack of accuracy in the negative region of the spectrum where the peaks present in the density of states are not visible. This problem is partially overcome in the normalized spectrum in (d) where the presence of the two peaks in the negative region is clear. It is necessary to note, though, that the intensities of the peaks are not proportional to the surface density of states.

Several approaches has been introduced in order to overcome this problem and to get more accurate quantitative data from the scanning tunneling spectroscopy measurements by normalizing the differential conductivity to a fitted asymmetric tunneling probability [26] or including expressions for the density of states of the tip [27].

In this work only the differential conductivity  $dI/dV$  will be analyzed since the aim is to get a qualitative picture of the density of the states of graphene on Ru(0001) around the Fermi level.



## **Chapter 2**

### **Experimental setup**

The aim of this chapter is the description of the experimental chamber used for the measurements with a brief explanation of the various surface science techniques used to characterize the systems. In particular a detailed description of the experimental problems related to Scanning Tunneling Spectroscopy will be given.

#### **2.1 The UHV chamber**

The experiments were performed in an ultra high vacuum (UHV) chamber equipped with several tools to perform surface analysis. The base pressure ( $p < 1 \cdot 10^{-10}$  mbar) is achieved with an ion pump and with a turbomolecular pump coupled to a rotary pump. In addition, the system is equipped with a titanium sublimation pump that minimizes the presence of residual gases in the background. The samples are mounted on a molybdenum sample holder equipped with a chromel-alumel thermocouple that allows the direct measurement of the sample temperature. The sample preparation is performed directly in vacuum by means of a manipulator equipped with several preparation tools.

The manipulator allows placing the sample directly in front of an ion gun suitable to perform argon bombardment at several energies. The sample can be heated by electron bombardment with a filament placed directly on its backside, and it can be cooled to  $\sim 130$  K with a liquid nitrogen flowing system connected to the manipulator by copper wires. The chamber can be backfilled by several gases via leak valves connected directly to a gas line attached to the main chamber. The background pressure is measured with an ionization gauge, and the gas composition is checked with a quadrupole mass spectrometer. The system is equipped with LEED (Low Energy Electron Diffraction) optics and a cylindrical mirror analyzer for AES (Auger Electron Spectroscopy). LEED is a standard technique used to obtain structural information about surfaces. It is used both to check the crystallographic quality of the sample and to obtain information about adsorbate induced structures. AES is a spectroscopic technique applied for the analysis of the surface chemical composition. The system is also equipped with facilities to perform TDS (Thermal Desorption Spectroscopy) that consists in heating the sample in a controlled way while monitoring the desorbing products by the mass spectrometer.

The Scanning Tunneling Microscope is of the beetle type [28, 29] and was built by J. Wintterlin and R. Schuster. It is connected with a liquid helium cryostat that allows cooling the sample down to  $\sim 50$  K, and it is equipped with a heating filament that allows performing scanning tunneling measurements in the entire range of temperatures between 50 K and 500 K. In order to avoid mechanical noise the chamber is decoupled from the floor by a pneumatic system operating with high pressure nitrogen. Atomic resolution with low mechanical noise was routinely achieved.

During my work with the graphene system I have also performed XPS (X-ray photoelectron spectroscopy) measurements in a separate ultra high vacuum chamber [30] using a non-monochromatized Mg  $K\alpha$  source (1253.6 eV). This spectroscopic technique is sensitive to the chemical species present on the surface and to their chemical bonding states.

## 2.2 Scanning Tunneling Spectroscopy

Studying the system formed by a graphene layer grown on the Ru(0001) surface with the Scanning Tunneling Microscopy technique, it was found that the images display strong and reproducible contrast inversion phenomena when measuring the topography with different bias voltages. These interesting spectroscopic effects reveal the presence of a complex surface electronic structure and for this reason I decided to investigate it with the Scanning Tunneling Spectroscopy technique.

Since this kind of measurements has never been performed before in the group, at the beginning of my work it has been necessary to test and characterize systematically the experimental aspects. In particular, it was required to test the electronics and the existing measuring software and to determine the optimal measuring conditions and parameters.

Furthermore, it has been necessary to establish the procedures to analyze the data and to implement the software tools for this purpose.

The following sections are devoted to the description of these aspects.

### 2.2.1 Setup

The Scanning Tunneling Microscopy measurements of surface topography in the constant current mode consist in scanning the surface with a metal tip driven by piezoelectric materials and recording its vertical displacements in order to maintain the tunneling current constant. This is achieved with a feedback circuit that adjusts the tip height while scanning. The scanning tunneling spectroscopy measurements, on the other hand, are based on the measurements of the dependence between the tunneling current and the bias voltage applied between tip and sample and for this reason the tip must be held at fixed lateral and vertical positions on the sample while applying a voltage ramp and recording the tunneling current. With our system we perform CITS (Current Imaging Tunneling Spectroscopy) measurements, measuring simultaneously the topography of a selected area in the constant current mode and several I-V curves by interrupting the scanning signals and the feedback loop at precise and known positions in the scanned area. Table 2.1 lists the parameters that control the spectroscopy measurements.

“x-mesh” and “y-mesh” determine the coordinates of the spectroscopy measurements in pixels, and they allow associating each spectrum with the topographic locations on the surface as indicated in figure 2.1a. The image is schematically formed by 49 pixels by 49 pixels and shows that the spectroscopy is performed on a grid of points separated by “x-mesh” pixels in the x direction and “y-mesh” pixels in the y direction. Each spectrum is then recorded together with its (x,y) coordinates.

“nb of points” is the number of points measured in each spectrum and “repetitions” is the number of spectra measured at the same location. “DC voltage” would give the bias voltage used for the simultaneous measurement of the topography but, in our system, it is set to 0 since the constant bias voltage for the imaging is manually set with the analog controller. “Start voltage” and “End voltage” determine the amplitude in mV of the voltage ramp applied to the sample for each spectroscopy measurement. Usually the ramp is symmetric with respect to 0 (Fermi Level) but this is not mandatory and the signal given by the ramp has to be added to the constant voltage given by the analog controller. The remaining parameters are related to the electronics setup and their effects are schematically shown in figure 2.1b.

x-mesh	End voltage
y-mesh	Delay between points
nb of points	Delay after TTL high
repetitions	Delay before ramp
DC voltage	Delay after ramp
Start voltage	Delay before TTL low

**Table 2.1:** List of parameters required by the measuring program to perform Scanning Tunneling Spectroscopy measurements.

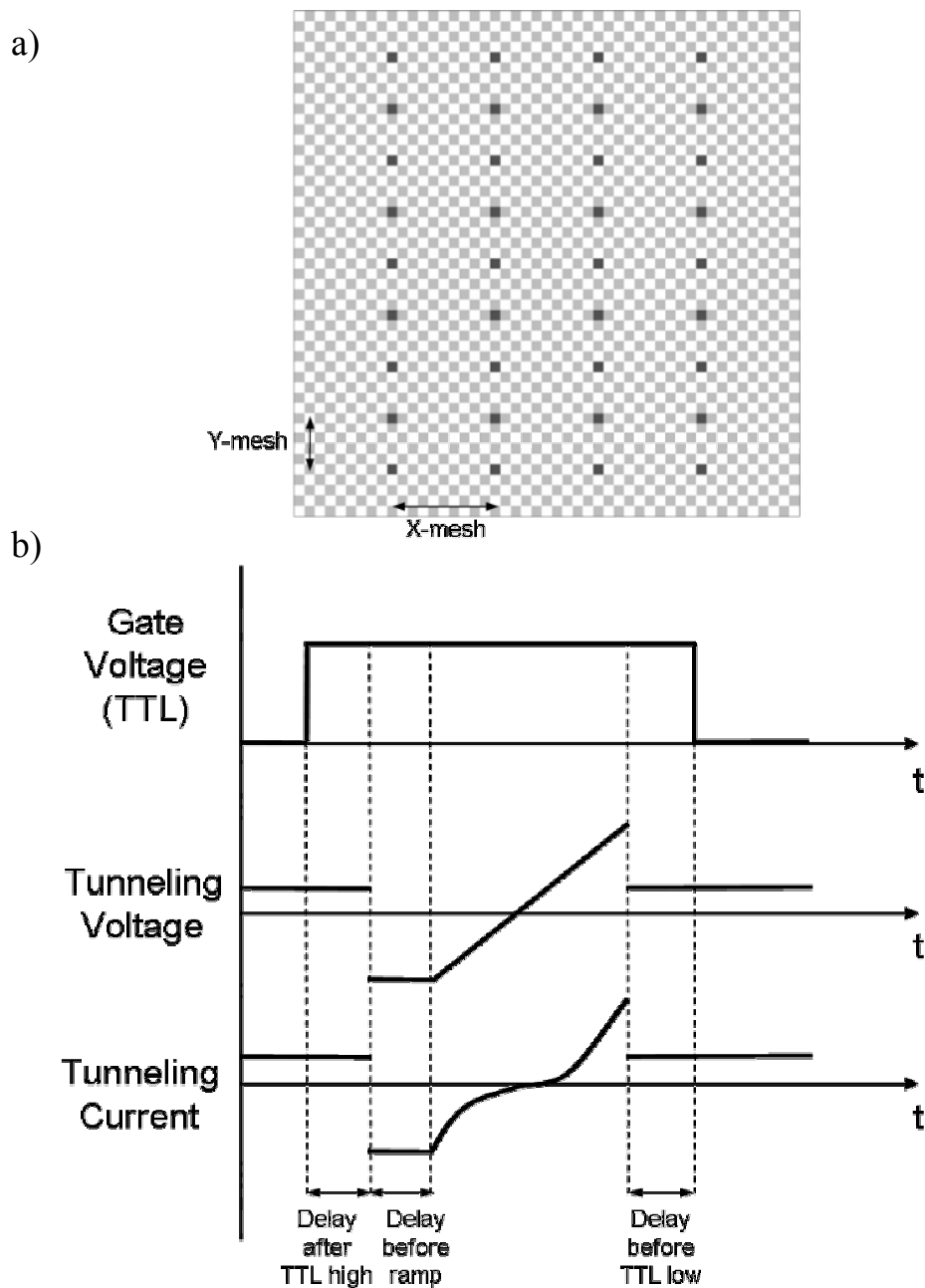


**Figure 2.1:** a) Image formed by 49 pixels  $\times$  49 pixels. The marked pixels represent the points where the spectroscopy measurements are performed and they form a grid with  $x$ -mesh = 10 pixels and  $y$ -mesh = 5 pixels. b) Schematic representation of the parameters “Delay after TTL high”, “Delay before ramp” and “Delay before TTL low”. The top curve represents the TTL signal: when the signal is 0 the feed back loop is activated and the position of the tip adjusted in order to held the tunneling current constant, when the signal is 1 the feed back is deactivated and the tip is held at a fixed vertical and lateral position. The middle and bottom curves display the tunneling voltage applied to the sample and the tunneling current, respectively.

“Delay between points” is the time length of each point measured in a spectrum and it is typically set to 6  $\mu\text{s}$  per point. “Delay after TTL high” is the time interval between the interruption of the feedback loop and the drop of the bias voltage to the “Start voltage” value. “Delay before ramp” is the holding time of the tip at a bias voltage equal to “Start voltage” before running the voltage ramp. When these two values are too short, the spectrum is characterized by spike signals at the beginning due to the sudden change in the bias voltage as shown in figure 2.2 in the top curve. On the other hand, if these values are too high, the tip might vertically drift from its holding position influencing the current measurement. When this happens, however, the topography image simultaneously recorded displays spikes at the locations where the topography is measured and the measurement is discarded. I managed to optimize these values (“Delay after TTL high” = 0, “Delay before ramp” = 100  $\mu\text{s}$ ) so that the images do not show any drift distortion and the spectra only display a single spike (figure 2.2, bottom curve) that is then manually discarded when performing the spectra analysis.

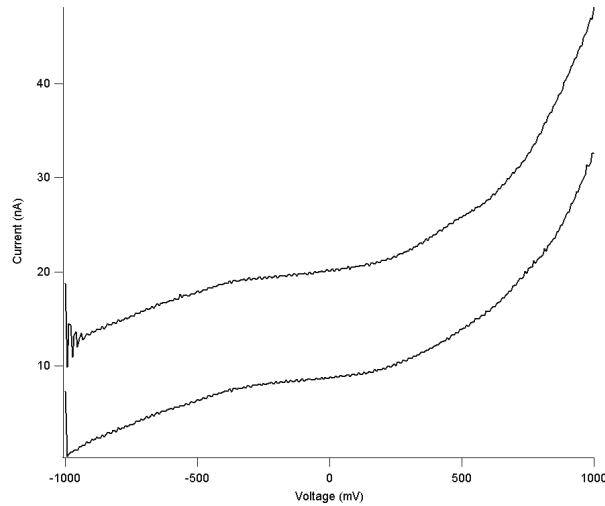


**Figure 2.2:** Comparison between two spectra measured with “Delay after TTL high” = “Delay before ramp” = 0  $\mu\text{s}$  (top curve) and “Delay after TTL high” = 0  $\mu\text{s}$  and “Delay before ramp” = 100  $\mu\text{s}$  (bottom curve). The top curve reveals the presence of spikes at the beginning due to the sudden change in the tunneling voltage. The bottom curve is characterized by the presence of a single spike.

“Delay after ramp” determines the time interval between subsequent spectra measured at the same location when “repetitions” is chosen higher than 1. “Delay before TTL LOW” regulate the time interval between the end of a spectrum and the following topographic measurement. I have never observed any kind of problem setting this value to 0 corresponding to a default time interval between the end of the ramp and the re-enabling of the feed back circuit of 600  $\mu\text{s}$ , while, on the contrary, longer values would cause thermal drift problems as well. Figure 2.3 displays the voltage signals output of the digital to analog converter (DAC) that is added to the tunneling voltage and the TTL signal interrupting the feedback loop.

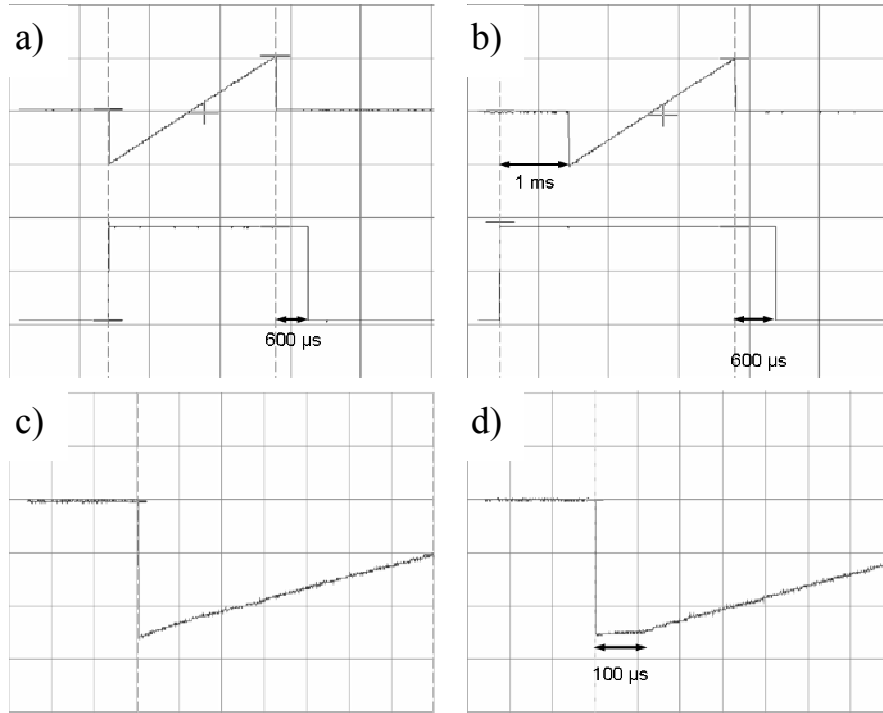


**Figure 2.3** a) Tunneling voltage (top curve) and TTL signal (bottom curve) in the case of “Delay after TTL high” = “Delay before ramp” = “Delay before TTL low” = 0  $\mu$ s. The tunneling ramp and the TTL signal start simultaneously while at the end the TTL signal has the default delay of 600  $\mu$ s. b) Tunneling voltage (top curve) and TTL signal (bottom curve) in the case of “Delay after TTL high” = 1 ms, “Delay before ramp” = 0  $\mu$ s, “Delay before TTL low” = 0  $\mu$ s. c) Tunneling voltage in the case of “Delay before ramp” = 0  $\mu$ s. d) Tunneling voltage in the case of “Delay before ramp” = 100  $\mu$ s.

In (a) the “Delay after TTL high” is set to 0 and the voltage ramp starts simultaneously with the interruption of the feedback circuit causing the presence of the spikes in the spectrum observed in the top curve of figure 2.2. (b) shows the case of a “delay after TTL high” of 1 ms. In both cases the 600  $\mu$ s delay between the end of the voltage ramp and the re-enabling of the feedback circuit is visible. Figures 2.3c and (d) show the effect of the “delay before ramp” parameter. In (c) this parameter is set to 0 and the spectrum starts immediately after the drop in the tunneling voltage, and displays spikes similar to those observed in figure 2.2. In (d) the optimum value of 100  $\mu$ s is shown: the tunneling voltage drops to the “start voltage” value and is kept there for 100  $\mu$ s before starting the voltage ramp and the spectrum measurement.

### 2.2.2 Noise problem

One of the main problems of the STM measurements is noise, both of mechanical and electronic nature, in the signals that are measured [19]. For this reason it is necessary to analyze noise also when performing tunneling spectroscopy measurements. The top curve

in figure 2.4a shows a measurement of the tunneling current when the feedback loop is activated (baseline) and when it is deactivated during the spectroscopy measurements (signal at +1.5 V with respect to the baseline). In both cases the tunneling current is characterized by a 70 kHz noise, and the peak-to-peak amplitude is higher in the case of spectroscopy. This noise is independent on the value of the tunneling current. This frequency is not a problem since it is much higher than the typical frequencies at which topographic structures appear in the scan lines ( $\sim 1$  kHz for a topographic periodicity of  $\sim 3$  Å measured with a typical scan speed of  $3$  Å/ms). Because of the cut-off frequency of the feedback loop of typically 1 kHz this noise signal does not appear in the topographic measurements and for the spectroscopy it can easily be filtered out. The bottom curve of figure 2.4a displays the tunneling current when a 10 kHz pre-filter is applied, and the 70 kHz component is absent.

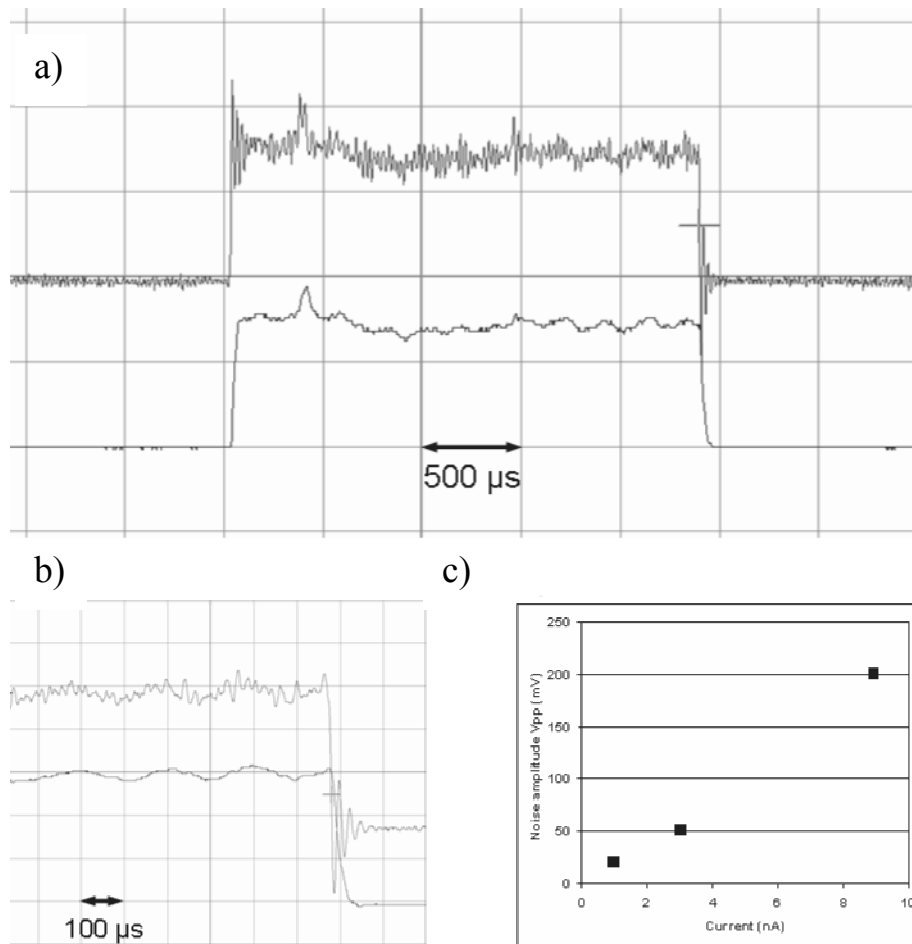


**Figure 2.4:** a) Tunneling current with (top) and without (bottom) 10 kHz pre-filter. The baseline value corresponds to the topography measurement with feedback loop activated, the signal at +1.5 V is measured with feedback loop deactivated during the spectroscopy measurement. The top curve displays both the 70 kHz and the 5 kHz noises while the top curve displays only the 5 kHz component. b) Enlargement of the signals shown in (a). c) Dependence of the 5 kHz noise amplitude on the value of the tunneling current. The signal-to-noise ratio is constant.

Both curves reveal also the presence of a further noise component. The frequency of this noise signal is 5 kHz, and it is possible to mechanically excite its amplitude which is a clear indication that its nature is mechanical. Furthermore, the noise amplitude depends on the tunneling current as shown in figure 2.4c. High currents correspond to a small tip-sample distance and the mechanical oscillations induce big changes in the current; on the contrary, small currents correspond to large tip-sample distances and the effect of the mechanical oscillation is small. As can be seen in figure 2.4c the signal-to-noise ratio is constant.

It is likely that this mechanical noise corresponds to a resonance frequency of the microscope due to the “beetle-type” geometry [31]. A beetle type STM head consists of a solid disk supported by three piezoelectric tube legs. Resonances involve a deformation of these legs and three intrinsic vibrational modes of the disk with respect to the sample holder arise: a horizontal translation, a vertical translation and a rotation around the symmetry axis. The resonance frequencies of these modes depend on the geometrical properties of the system, but they are typically in the range between 4 and 6 kHz [32]. In order to minimize the influence of this signal on the spectroscopy data, spectroscopy measurements were performed with faster voltage ramps, lasting 500÷1000  $\mu$ s, and several spectra were always averaged. The resulting spectra still displaying 5 kHz oscillations were discarded from the analysis.

### 2.2.3 Data analysis

The scanning tunneling spectroscopy data, like every spectroscopy measurements, are additionally characterized by the presence of random noise. This can be simply reduced by measuring the same signal several times and averaging it. In the case of Current Imaging Tunneling Spectroscopy this was achieved by measuring several spectra on equivalent topographical features and averaging them. Typically, in an image formed by 300x300 pixels, the spectroscopy measurements are performed every 10 pixels in both directions, resulting in over 900 spectra. Figure 2.5a displays a single spectrum and the result of the average over 900 spectra measured on equivalent topographical features and it is clearly visible that the amplitude of the noise is strongly reduced while the trend of the signal is not affected.

In the first chapter, it was shown that in order to get information about electronic features of the surface it is necessary to calculate the first derivative ( $dI/dV$ ) of the signal. However, it is commonly observed that differentiation degrades the signal to noise ratio, and even when the noise is not particularly evident in the original signal, it is then more noticeable in the derivative. Figure 2.5b shows the numerical derivative of the averaged signal of figure 2.5a calculated according to the routine described in reference [33]. The curve is characterized by the presence of strong oscillations due to the noise in the original signal, and it is almost impossible to detect significant features related to real spectroscopic properties of the system.

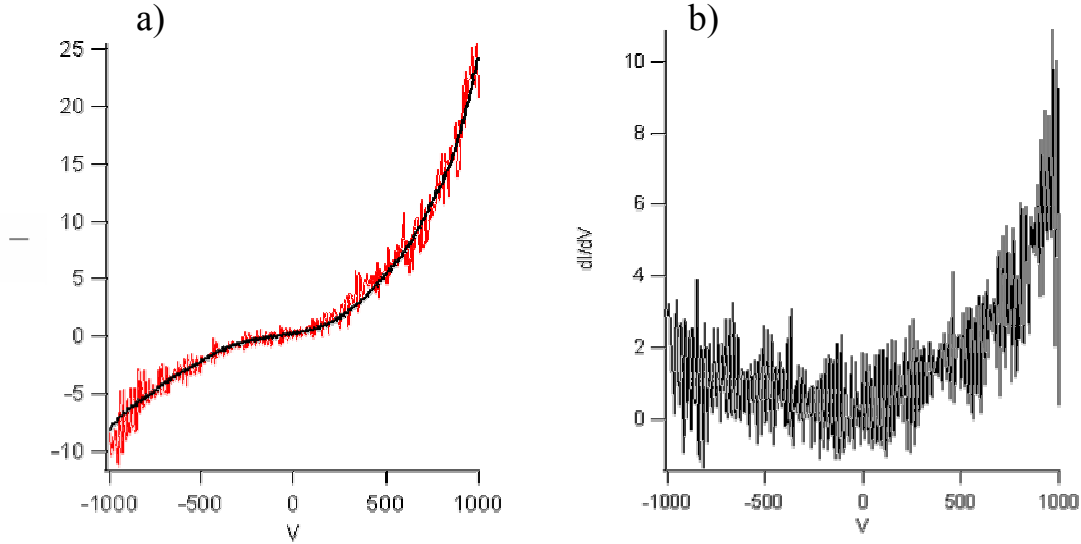


**Figure 2.5:** a) Comparison between a single spectrum (red) and the average (black) over 900 spectra measured on equivalent topographical features. The average procedure reduces the noise amplitude without affecting the trend of the signal. b) Derivative of the signal obtained averaging 900 spectra and revealing the presence of strong oscillations due to the noise in the original signal.

In order to overcome this problem and to extract useful information from the tunneling spectroscopy data, the data were additionally smoothed. The basic idea behind the application of smoothing algorithms is that the true signal will change smoothly as a function of the voltage while the noise consists of rapid, random changes in the amplitude from point to point.

There are several algorithms for smoothing data signals, from the simple “moving average” algorithm to more elaborate interpolating procedures [34-36], and the choice of the most suitable algorithm has to be made considering the information that is necessary to extract from the data.

In the present case the interest lies in a smooth signal containing the tunneling spectroscopy information that is represented by slight changes in the slope of the curve and whose first derivative is also smooth. For these reasons it was decided to apply the smoothing algorithm by spline functions introduced by Christian Reinsch [37].

This algorithm minimizes:

$$\int_{x_0}^{x_N} g''(x) dx$$

among all functions  $g(x)$  such that:

$$\sum_{i=0}^N \left( \frac{g(x_i) - y_i}{\sigma_i} \right)^2 \leq S$$

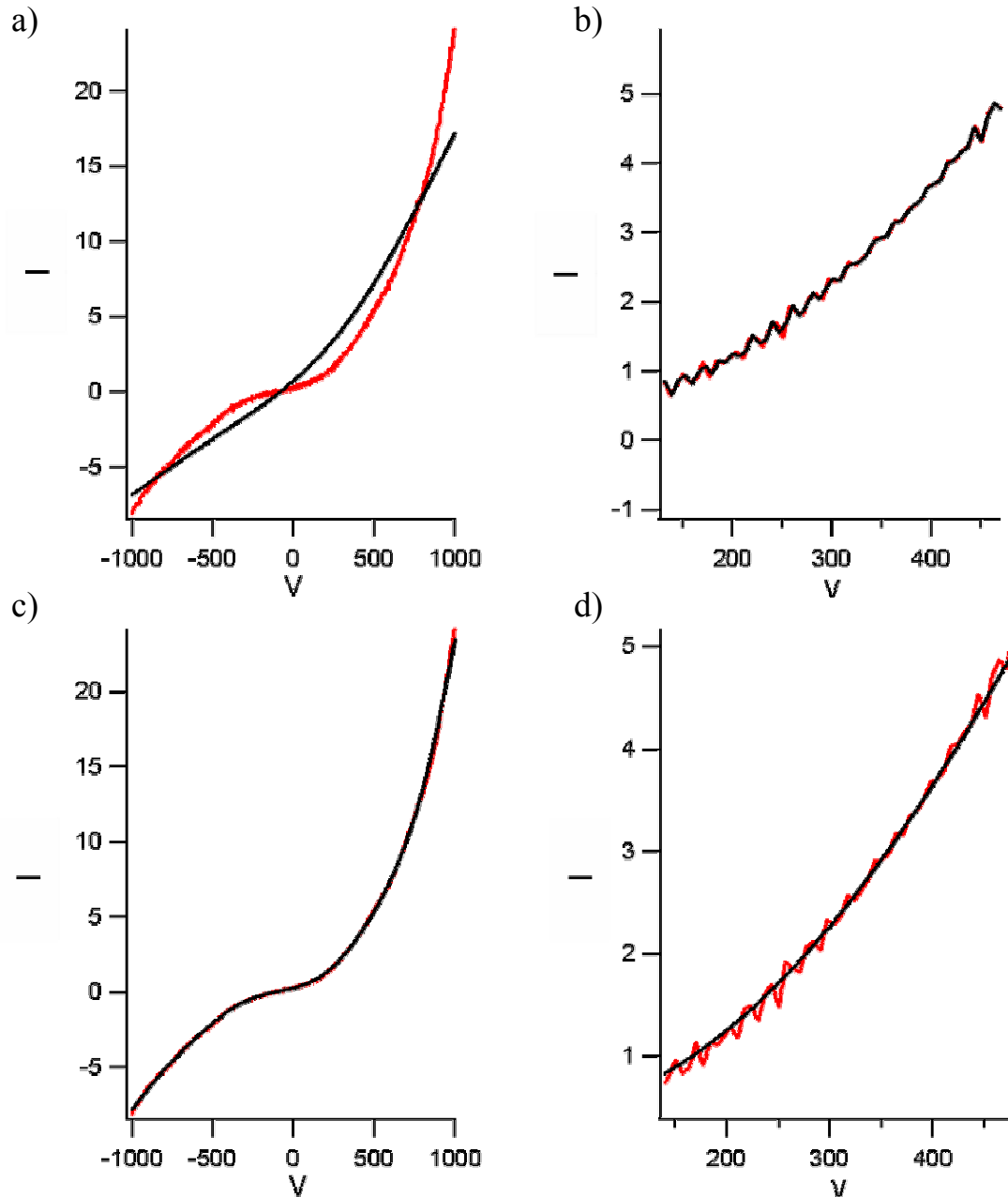


**Figure 2.6:** Comparison between smoothing spline functions obtained for three different values of the smoothing factor  $S$ . The experimental curve is shown in red while the smoothing function is shown in black. a)  $S = 1.0$ . The trend of the smoothing function is different from the original data. b)  $S = 0.001$ . The smoothing function reveals the presence of oscillations due to noise (the graph shows only a portion of the curve enlarged) c)  $S = 0.1$ . The smoothing function has the same trend as the original data and, as can be seen in the enlargement in (d) it does not display oscillations due to the presence of noise.

$N$  is the number of points measured,  $g(x_i)$  is the value of the smooth spline at a given point,  $y_i$  is the measured value at the same point,  $\sigma_i$  is the standard deviation of that point and  $S$  is the smoothing factor.

The result is a function composed of cubic parabolas which join at their common endpoints such that  $g$ ,  $g'$  and  $g''$  are continuous.

The parameter  $S$  controls the extent of the smoothing and it is generally chosen between 0 (corresponding to no smoothing) and 1.0.

The analysis was generally started with a value of  $S$  of 1.0, and then  $S$  was decreased until the smoothing function reproduced the trend of the measured data without showing oscillations due to noise. Figure 2.6 shows the smoothing spline functions calculated for the averaged signal of figure 2.5a with  $S=1.0$ , 0.1 and 0.001, respectively. The trend of the curve obtained with  $S=1.0$  (figure 2.6a) is completely different from the trend of the measured data. On the other hand,  $S=0.001$  (figure 2.6b) is too small and the smoothing curve reveals oscillations that are smaller in amplitude than the oscillations of the original curve but they still display significant noise and do not contain any spectroscopic information.  $S=0.1$  (figure 2.6c and the enlargement in (d)) is in this case the optimal value reproducing the trend of the measured data without displaying oscillations due to the noise.

The derivative [33] of the curve obtained with  $S=0.1$  is shown in figure 2.7: it is smooth and clearly reveals the presence of two spectroscopic features at about -500 mV and +500 mV whose nature will be explained in detail in chapter 3.

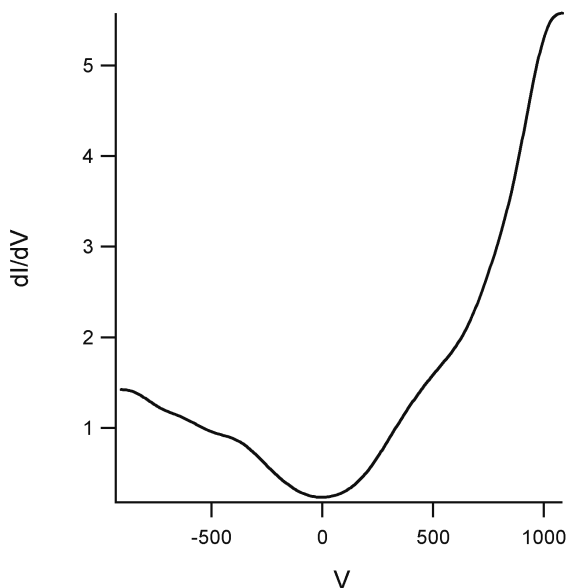


**Figure 2.7:** Derivative of the curve obtained with  $S = 0.1$  in figure 2.6c.



## Chapter 3

### Graphene on Ru(0001)

This chapter describes the results about monolayer graphite grown on the Ru(0001) surface. The initial reason to investigate this system was to study relevant problems related to catalyst poisoning and deactivation. During this study, though, interesting structural and electronic properties of the system graphene/Ru(0001) were observed that, together with the recent excitement about graphene monolayers and the research in the field of nanotechnology, suggested us to expand the study and to investigate possible applications of this system as template to engineer self assembled ordered nanostructures.

#### 3.1 The Ru(0001) surface and the sample preparation procedure

Ruthenium is a transition metal of the platinum group with atomic number 44 and electronic configuration  $[\text{Kr}]4d^75s^1$ . It crystallizes in the hexagonal close-packed (hcp) structure with lattice constants  $a = 2.706 \text{ \AA}$  and  $c = 4.282 \text{ \AA}$ . The (0001) surface is characterized by a triangular lattice with lattice constant  $a = 2.706 \text{ \AA}$  and by the presence of monoatomic steps with a step height  $h = c/2 = 2.141 \text{ \AA}$ . Figure 3.1 displays a model of the surface which will be useful for the structural characterization of the graphene system.

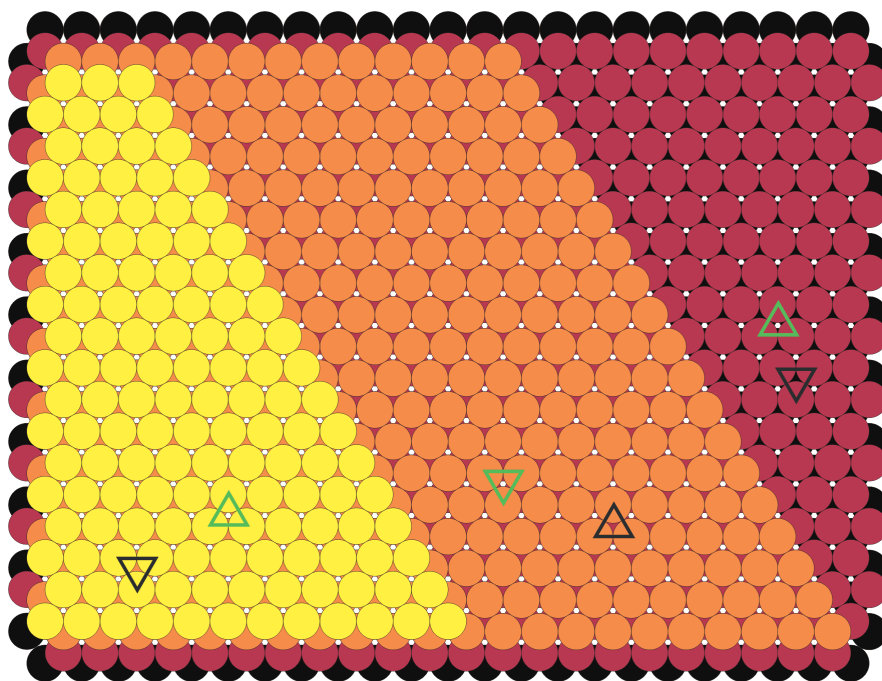


**Figure 3.1:** Model of the Ru(0001) surface. The model displays three terraces separated by monoatomic steps with different colors. The triangles show the threefold hollow sites: in green fcc, in black hcp.

The model displays 4 atomic layers of the metal with the ABA stacking of the hcp structure. On the upper terrace, displayed in yellow, one can distinguish the two types of threefold hollow sites: the fcc sites (green triangle) which do not have a metal atom below and the hcp sites (black triangle) directly above a metal atom of the second layer. The nomenclature pertains to the sites that would be occupied by atoms in an fcc or hcp crystal. The second layer is shown in orange and, since it is displaced horizontally with respect to the upper layer, the symmetry of the threefold hollow sites with respect to the three surrounding atoms is changed. On the upper terrace the three atoms surrounding the fcc sites form a triangle pointing upward, on the contrary, on the second layer, the triangles surrounding the fcc sites point downward. For the hcp sites the situation is reversed. The third layer is depicted in purple, and is in phase with the upper layer. The ABA stacking causes the appearance of two different kinds of monoatomic steps on the (0001) surface: the type I steps, like the one between the yellow and the orange terrace, is characterized by fcc sites on the upper edge of the step, and the type II steps, which is characterized by hcp sites as hollow sites closest to the step. This reflects in different chemical properties of the different steps [38].

For my measurements I have employed two different Ru single crystals with similar properties. The samples have a diameter of 5 mm and a thickness of 1 mm, and are mounted on molybdenum sample holders by tantalum stripes.

The sample was cleaned following standard cleaning procedures for Ru [39] that were optimized by checking the surface conditions by means of XPS, AES, LEED and STM. The first step in the preparation procedure is argon bombardment at room temperature for 10 minutes. To obtain a sputtering current of about 5  $\mu\text{A}$  I worked with 1 keV energy and an Ar pressure in the chamber of  $5 \cdot 10^{-5}$  mbar. Subsequently the sample is slowly annealed to a temperature higher than 1000 K for about 1 minute where a maximum temperature of about 1500 K is reached. The aim of the annealing is twofold: it removes the argon deposited below the surface during the sputtering, and it is necessary to restructure the surface damages caused by the ion bombardment and to create large flat terraces. It is known that the threshold for atom self diffusion on metal surfaces is about 1/3 of the melting temperature of the crystal: in the case of ruthenium this temperature is 2607 K, so it is necessary to reach  $\sim 900$  K to obtain large flat terraces.

The sample is kept at 800 K and the chamber is backfilled with  $2 \cdot 10^{-7}$  mbar of oxygen for 30 minutes in order to remove carbon and finally with  $1 \cdot 10^{-6}$  mbar of hydrogen, again for 30 minutes, to remove the oxygen left on the surface. A final quick flash annealing to 1800 K allows obtaining a clean sample as shown in figure 3.2. The image displays a large area of the metal with six terraces separated by monoatomic steps. The terraces appear flat, without defects and without adsorbate species. Further measurements with LEED and AES confirm the order of the crystal surface and the absence of contaminants. To further characterize the state of the surface on the atomic level, I have tried to reproduce experiments on the dissociation of NO [38]. The results are shown in figure 3.3. Figures (a) and (b) were recorded before and after dosing 0.2 L of NO at room temperature. The image in (b) is thermally drifted down and to the left with respect to (a) as can be seen from the defect marked in both figures. In (a) the surface shows a monoatomic step and 14 defects displayed as black depressions on an area of  $25 \times 25 \text{ nm}^2$  corresponding to a coverage of 0.0014 monolayers. These defects have been reported before [40], and they have been associated with C atoms. After dosing NO (b), two new features appear. At the area close to the step there are dark features displaying a triangular shape that represent slowly diffusing N atoms, second on the entire area there are dark stripes that are due to fast diffusing O atoms. This distribution is explained by the special dissociation mechanism of the NO molecules. NO molecules adsorbing on the surface do not dissociate at the sites where they impinge and first stick on the surface. They diffuse then across the terraces until they find a step where they dissociate into N and O atoms. The N atoms are barely mobile at 300 K, so that most of them are still found at the step. The O atoms are much more mobile, so that they rapidly redistribute across the surface.

This experiment confirms that the cleaning preparation procedure is efficient and that, at room temperature, the sample is not populated by contaminant species that would modify the reactivity of the surface. On the contrary, at very low temperatures the surface collected some oxygen containing contaminant from the gas phase. This aspect does not play a role for the graphene experiments, but the detailed measurements performed to identify the chemical nature of this species are presented in Appendix A.

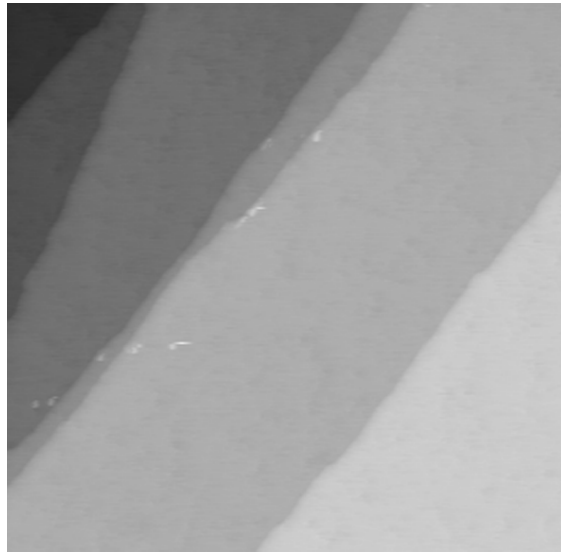
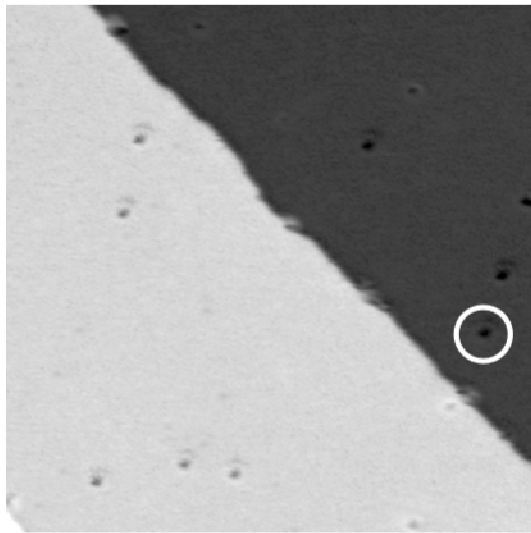


**Figure 3.2:** STM image taken at room temperature showing a large area of the sample after the optimized cleaning procedure.  $100\text{ nm} \times 100\text{ nm}$ ,  $I_t = 1\text{ nA}$ ,  $U = +0.5\text{ V}$ .

a)



b)

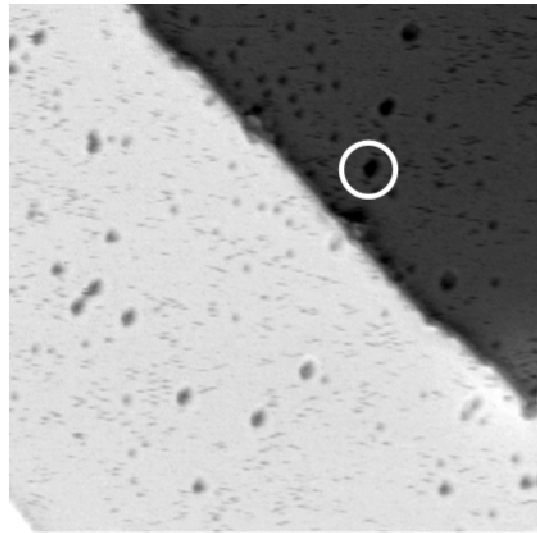


**Figure 3.3:** STM images taken at room temperature on the same area before (a) and after (b) dosing  $0.2\text{L NO}$ . The white circles mark the same feature on both images.  $25\text{ nm} \times 25\text{ nm}$ ,  $I_t = 1\text{ nA}$ ,  $U = +0.3\text{ V}$ .

## 3.2 Graphene

Ruthenium has been extensively studied for several years in the group. Occasionally the STM data showed that some part of the surface was covered by an ordered superstructure whose nature has never been systematically investigated. In the following a detailed analysis of this structure will be presented, and a possible application as a nanotemplate for engineering nanostructures will be discussed.

### 3.2.1 Formation of the ordered superstructure

During my measurements on the Ru(0001) surface I found that the formation of the superstructure is connected with the preparation procedure to clean the sample. In particular the final flash employed to remove residual chemical species adsorbed during the previous steps of the preparation procedure is important. When this final flash is so quick that the sample temperature is higher than 1000 K for less than 30 seconds, the surface is clean as shown in figure 3.2. When the final flash is prolonged and the sample temperature is kept above 1000 K for more than 1 minute, the superstructure appears. After annealing the cleaned sample for 90 seconds at 1400 K the large area STM images of figure 3.4 were recorded. The surface is covered with a superstructure forming a hexagonal lattice with a lattice constant of  $\sim 3$  nm. The periodic structure displays some angular distortions, mainly around edge dislocations in the overlayer, and there are also several translational domains. However, no areas of bare metal were observed after such a prolonged annealing, so that the entire surface is covered by the same quasi-periodic superstructure. This structure was reproducibly formed by extended annealing, and the same type of STM images were obtained from two other Ru(0001) sample investigated before.

In order to check the crystallographic state of the entire sample and to get more information about the periodicity of the superstructure, LEED experiments were performed (figure 3.5). The LEED pattern displays the bright spots caused by the Ru(0001) substrate and satellite spots that are caused by the superstructure. The satellites spots have the same hexagonal symmetry as the substrate spots indicating that the ordered hexagonal superstructure covers macroscopic areas of the crystal. Since the diffraction pattern corresponds to the surface reciprocal lattice, the reverse transformation gives the periodicity in real space; in particular, the distance between the satellites spots compared with the distance between the substrate spots gives the periodicity of the superstructure. Averaging over several measurements like the one shown in figure 3.5 gives a periodicity of  $11.6 \pm 0.2$  substrate lattice constants, corresponding to about 3.1 nm. This value is in reasonable agreement with the STM observations of figure 3.4.

Since the diameter of the electron beam in LEED is approximately 1 mm, the diffraction patterns confirm that the STM observations are valid over macroscopic areas of the crystal. Finally, moving the sample in front of the LEED shows that the entire crystal is covered by the superstructure.

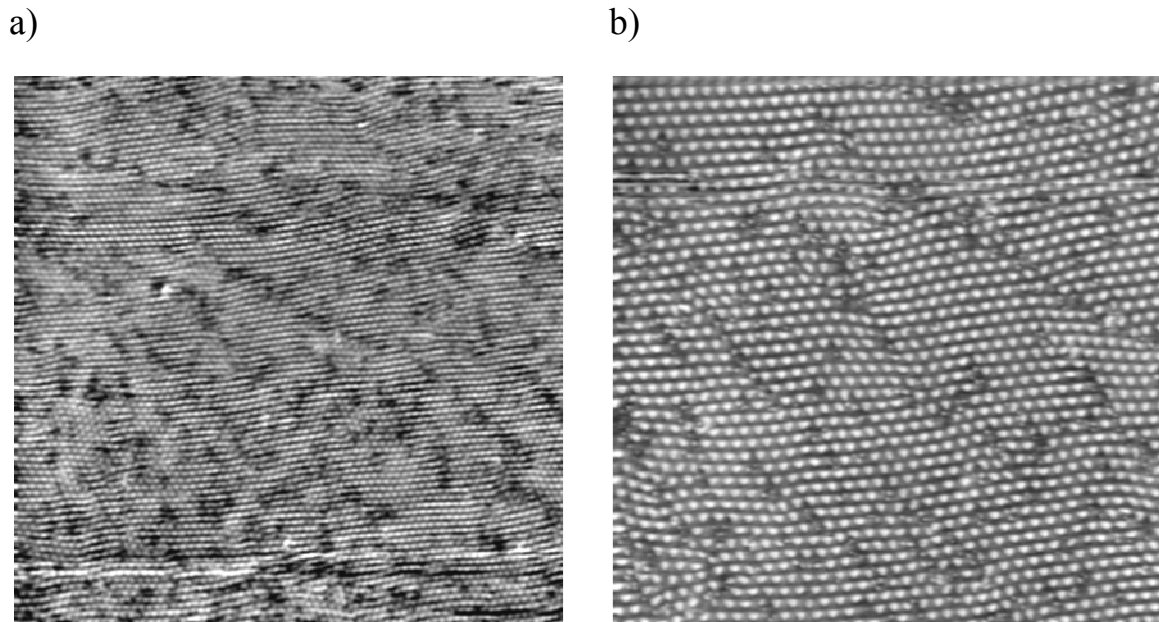


**Figure 3.4:** STM images taken after 90 sec annealing of the clean sample at 1400 K.  $I_t = 3$  nA,  $U = -0.85$  V. a) 200 nm x 200 nm b) 100 nm x 100 nm

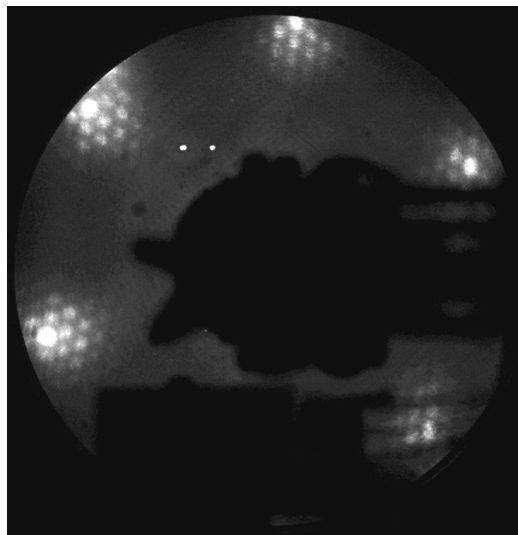


**Figure 3.5:** LEED pattern of the surface shown in figure 3.4. The bright substrate spots are surrounded by weaker satellites caused by the periodical superstructure. Beam voltage 86 eV.

### 3.2.2 Identification of the chemical species responsible for the formation of the superstructure

In order to identify the chemical species responsible for the formation of the superstructure X-ray Photoelectron Spectroscopy (XPS) measurements were performed. The survey spectrum (figure 3.6) shows exclusively ruthenium peaks, and it seems that the surface is not populated by any other chemical species. However, it is necessary to analyze in detail the main ruthenium peaks due to the Ru  $3d_{3/2}/3d_{5/2}$  doublet. The results are shown in figure 3.7 where only the binding energy region of the Ru  $3d_{3/2}/3d_{5/2}$  doublet is displayed. Figure 3.7a shows the spectrum measured on the clean surface. The fit of the measured data, after subtraction of the background due to inelastic scattering effects, reveals two peaks centered at binding energies of 280.1 eV and 284.1 eV. These peaks correspond to the Ru  $3d_{5/2}$  and Ru  $3d_{3/2}$  states respectively [41]. The ratio between the areas of the two peaks (branching ratio) is 1.51 as expected for the 3d doublet. Ruthenium has the 3d sub-shell completely filled by 10 electrons and the removal of a photoelectron from the 3d orbital leads to a  $3d^9$  configuration. Since the d orbitals have non-zero orbital angular momentum ( $l=2$ ), there is a coupling between the unpaired spin ( $s=1/2$ ) of the nine remaining electrons and the orbital angular momentum. The total angular momentum  $j$  is given by  $j = |l \pm s|$  and a state with angular momentum  $j$  has a degeneracy of  $2j+1$ . The  $3d^9$  configuration thus gives rise to two states differing in energy and degeneracy. One state has total angular momentum  $j = 3/2$  with a degeneracy of 4, the other has total angular momentum  $j = 5/2$  and a degeneracy of 6. The degeneracy of a state determines the probability of transition to such a state during photoionization which is reflected by the area of the peak in the XP spectrum. For the Ru  $3d_{5/2}/3d_{3/2}$  doublet a branching ratio of  $6/4 = 1.5$  is expected. Finally, according to Hund's third rule [42], as the  $3d^9$  shell of ruthenium is more than half full, the state with maximum  $j$  is the one with lower binding energy and this is why the Ru  $3d_{5/2}$  peak has a lower binding energy than the Ru  $3d_{3/2}$ .

Figure 3.7b shows the XP spectrum measured when the surface is covered by the superstructure. A fit of the data with two peaks (not shown in the figure) gives a branching ratio between the peaks areas of 1.25 which is not correct for the reasons discussed above. This fact indicates that the higher energy peak, the one with smaller area, hides a further component. Applying the same fit (i.e. the same branching ratio of 1.51 and the same energies) as for the clean surface (figure 3.7a), it is found that the higher binding energy peak contains an additional component (marked with a thick line in figure 3.7b) centered around 284.8 eV. This is the typical energy of the 1s state of carbon in the graphitic form [41].

XPS gives thus the first indication that the chemical species responsible for the formation of the superstructure is carbon.

In order to confirm this result and to characterize the evolution of surface carbon as a function of annealing temperature Auger Electron Spectroscopy was performed. Also for AES, as for XPS, a complication arises from the overlapping of the C and the main Ru peaks. The Ru main peak due to a MNN transition occurs at 273 eV [43] and the C KLL transition occurs at 272 eV [43].

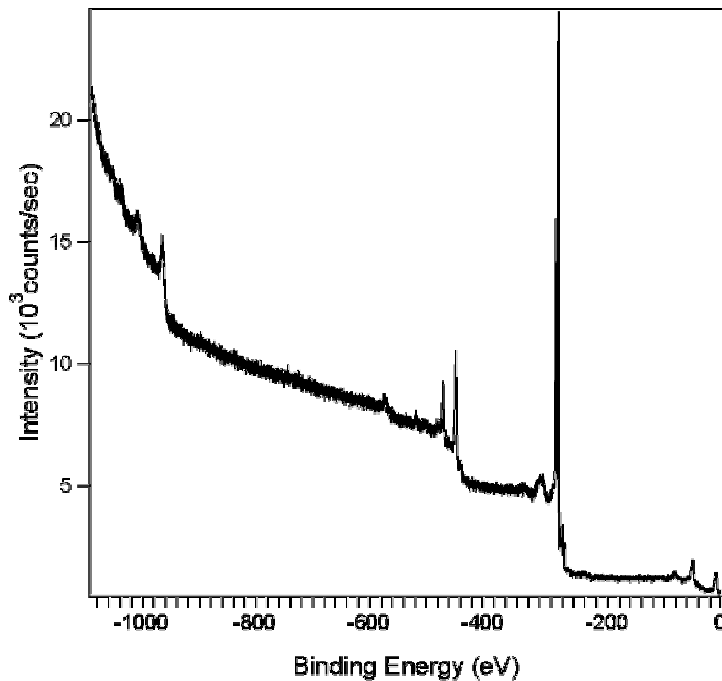


**Figure 3.6:** XPS survey spectrum of the surface shown in figure 3.4. The spectrum only exhibits ruthenium photoemission peaks and Ru Auger transition peaks.

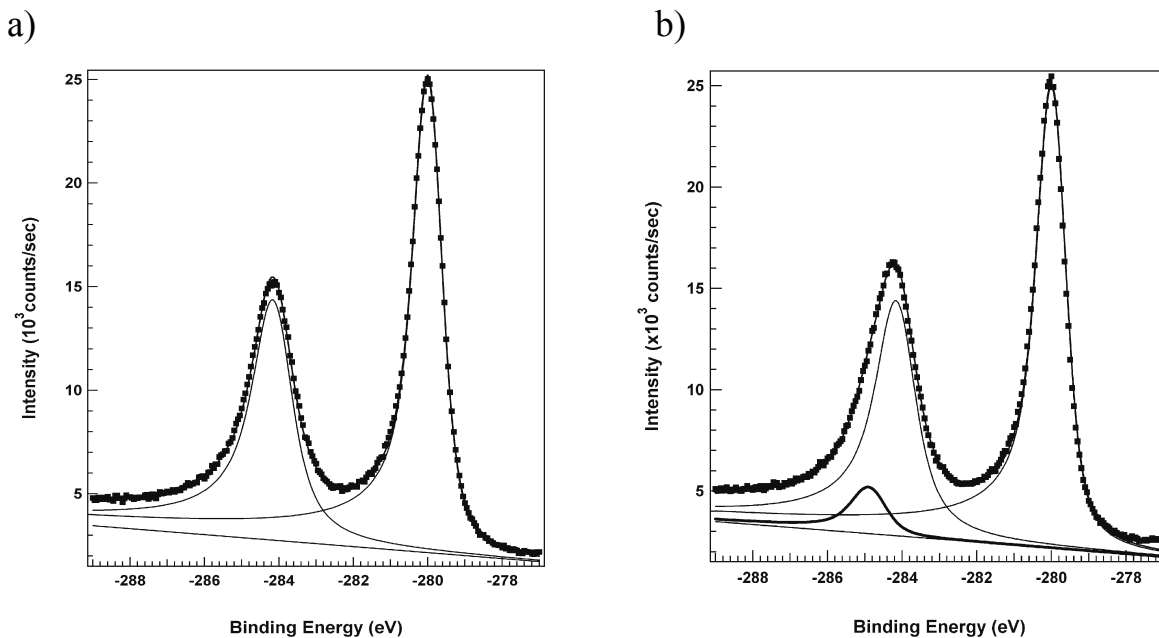


**Figure 3.7:** XPS of Ru(0001) showing the binding energy region of the Ru  $3d_{3/2}/3d_{5/2}$  doublet. a) Clean sample. b) Sample annealed for 90 s at 1400 K and displaying a LEED pattern as in figure 3.5.

However, the main feature of graphitic carbon in the differentiated spectrum is characterized by a relatively broad and pronounced negative going peak as can be seen in figure 3.8a [43]. On the contrary, the main peak of ruthenium at 273 eV is nearly symmetric. Hence, the amount of carbon on Ru surfaces can be determined by measuring the ratio  $R$  between the intensities of the lower and the upper half of the 273 eV peak [44-46]. Figures 3.8b and (c) display AES measurements of the clean Ru(0001) sample (b) and after 90 s annealing at 1400 K and thus covered by the superstructure (c). In (b) the main peak is nearly symmetric and has a ratio  $R = 1.30$  in agreement with the data for clean Ru [43]. In (c) the main peak is strongly asymmetric with  $R = 1.97$  indicating the presence of carbon in the graphitic form on the surface.

Hence, XPS and AES measurements agree well with each other and show that the superstructure must consist of graphitic carbon that segregates from the bulk to the surface during the annealing.

The behavior of the ratio  $R$  as a function of the annealing temperature has been studied and the results are shown in figure 3.9. The freshly prepared clean surface displays a ratio of 1.30, which is in agreement with the standard data for Ru [43]. Prolonged annealing up to a temperature of 800 K is of no effect.

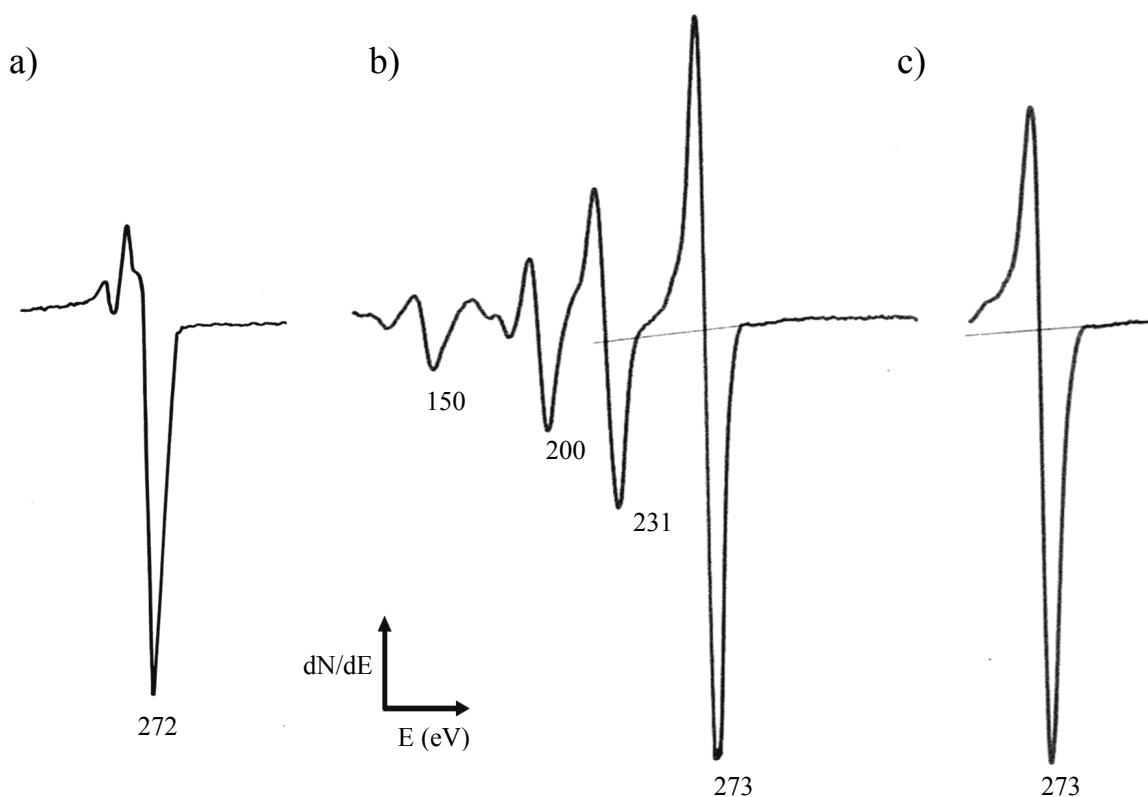


**Figure 3.8:** Differentiated AES spectra. a) Spectrum of bulk graphite from ref. [43]. The differentiated KLL transition at 272 eV is characterized by a pronounced negative going peak. b) Clean Ru(0001) surface: the main peak at 273 eV is nearly symmetric with a ratio  $R = 1.3$  in agreement with the reference data [43]. c) Main peak measured after 90 s annealing at 1400 K: the peak is strongly asymmetric with a ratio  $R = 1.97$  revealing the presence of carbon in the graphitic form on the surface (Primary electron energy: 2 KeV).

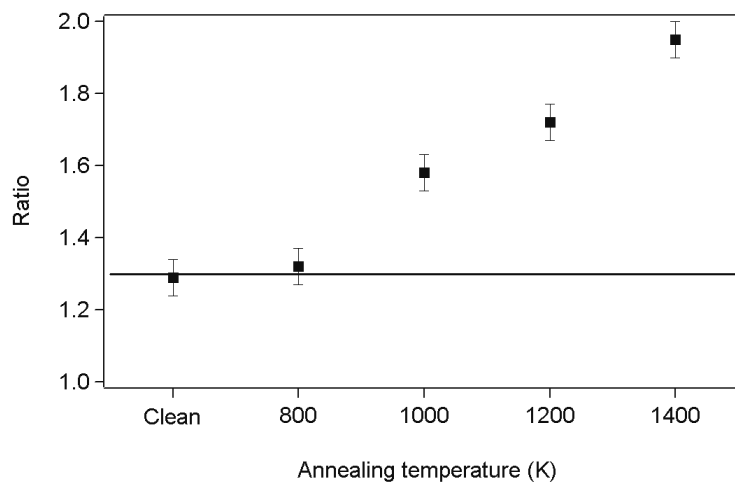
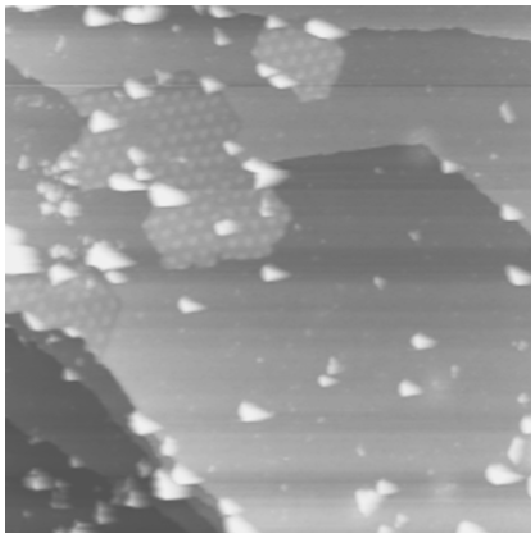


**Figure 3.9:** Ratio  $R$  of the negative and the positive going parts of the combined C KLL and Ru MNN Auger transitions at 273 eV as function of the annealing temperature. The line at a ratio of 1.3 is the literature value for the clean Ru surface [43]. The increase between 1000 K and 1400 K shows the segregation of carbon.

a)



b)

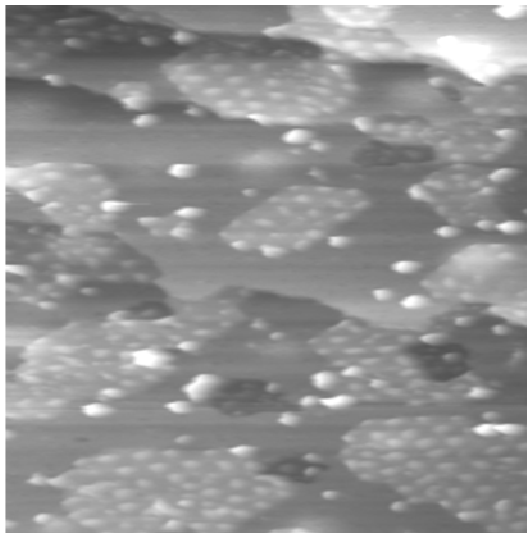


**Figure 3.10:** STM images of Ru(0001) after prolonged annealing to different temperatures. 100 nm x 100 nm,  $I_t = 3$  nA,  $U = -0.7$  V. a) Annealing to 1000 K,  $R = 1.57$  b) Annealing to 1200 K,  $R = 1.70$ .

Then, for temperatures between 1000 K and 1400 K the ratio increases up to a value of 2.0, indicating the segregation of carbon to the surface. The STM images of figure 3.10 display the surface after prolonged annealing to 1000 K (a) and 1200 K (b) corresponding to ratios  $R$  of 1.57 and 1.70, respectively. It is clear that the coverage of the superstructure increases with increasing annealing temperature. Annealing to 1400 K leads to a surface completely covered (figure 3.4).

The behavior of  $R$  has also been monitored during the sample preparation steps in order to optimize the preparation procedure itself when it is necessary to avoid the carbon segregation and to check the reactivity of the graphite layer (figure 3.11). Once the surface is completely covered by the superstructure ( $R \sim 2$ ), oxidation at 800 K partially removes the carbon but is not effective to completely clean the sample, and requires relatively long times ( $p(\text{O}_2) = 2 \cdot 10^{-7}$  mbar). Sputtering with argon at room temperature, on the contrary, is efficient in completely removing the graphite layer ( $p(\text{Ar}) = 5 \cdot 10^{-5}$  mbar,  $E = 1$  keV,  $t = 15$  minutes). The slow annealing after the sputtering causes some segregation of carbon which, however, can be removed by oxidation, provided that the annealing was short enough to cover the surface only partially. For this reason the annealing during the cleaning procedure is performed in such a way that the sample is kept at temperatures higher than 1000 K for no more than 1 minute and to reach a maximum temperature of about 1500 K. Oxidation and reduction are performed at 800 K and, as seen in figure 3.9, this temperature is of no effect for the carbon segregation. The final flash is uncritical as it is performed in a very short time ( $\sim 30$  seconds).

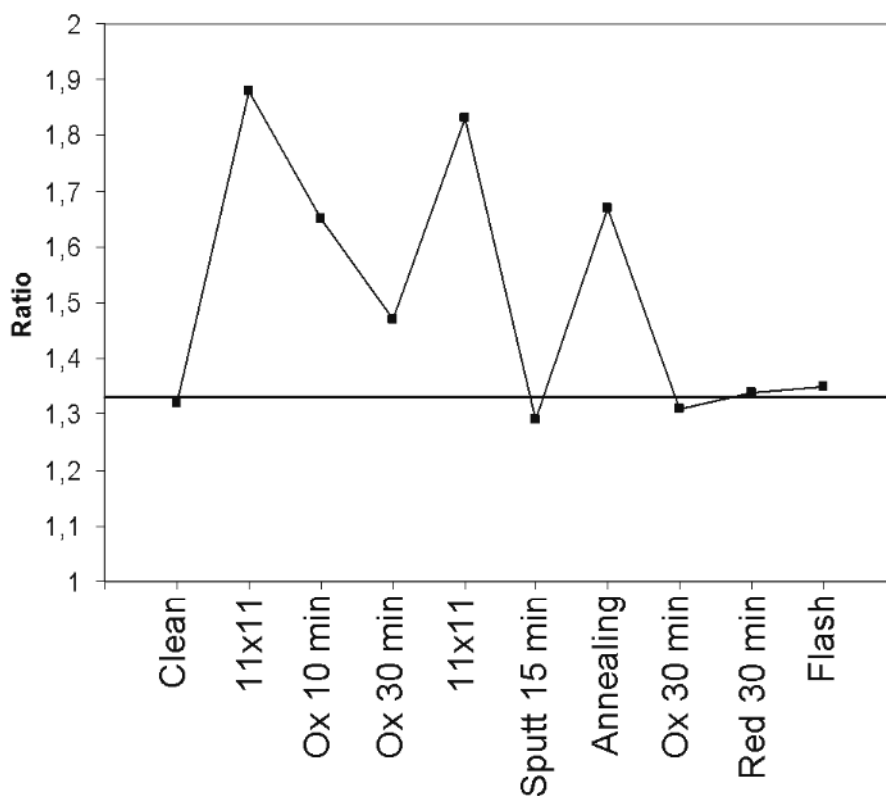


**Figure 3.11:** Ratio  $R$  after the different steps of the sample preparation procedure.

The stability of the graphite overlayer towards chemical reactions has also been proven indirectly. Since the XPS facilities are in a separate UHV system, the sample had to be transferred (for  $\sim 15$  minutes) through air to this chamber after the annealing treatment to take XPS data. The LEED pattern after the transfer showed the same overlayer spots as before (figure 3.5), evidencing that the overlayer is stable in air. Considering the chemical inertness of graphite and the difficulty of removing graphitic deposits from deactivated catalysts this property is not surprising.

In this paragraph it has been shown that it is possible to completely cover a Ru(0001) sample with a superstructure of carbon in the graphitic form simply by annealing for prolonged time ( $\sim 90 \div 120$  seconds) in UHV. An established procedure to prepare graphite layers on surfaces is by decomposition of CO or hydrocarbon molecules on metal surfaces at elevated temperatures [47-50]. This is the same process occurring as an undesired by-reaction in heterogeneous catalysis, where deposits of graphitic carbon are a major reason for catalyst deactivation. Graphite layers can also be formed by surface segregation of carbon by annealing carbon containing materials.

The effect has been investigated for example with carbon doped metals, but it often occurs also during the usual sputtering/annealing preparation of (nominally) clean metal crystals [51-53]. In an early work on the Ru(0001) surface Grant and Haas observed during cleaning of the ruthenium sample, in particular after annealing to 1800 K, that the LEED pattern displayed hexagonal satellite spots [54]. The authors interpreted this phase as a (9x9) overlayer of graphite, formed by carbon segregation. Later Goodman and coworkers found in a STM investigation of carbon species formed by decomposition of methane on Ru(0001) that, when the sample was subsequently annealed at 1300 K, a long-range surface structure appeared [55]. The lattice constant corresponded to an (11x11) superstructure, suggesting a moiré structure from the lattice mismatch between a single graphite layer and the Ru(0001) surface.

The following paragraphs present a systematic investigation of the geometry and the structural properties of the superstructure by STM. High resolution images displaying atomic features will be employed to develop a structure model.

### **3.2.3 Geometry of the superstructure**

#### **I. Partial coverage**

In order to understand the structural properties of the graphitic overlayer it is necessary to determine its morphology, its orientation with respect to the ruthenium lattice, the periodicity of the superstructure and the arrangement of the atomic features.

The first results are obtained studying the system when the surface is only partially covered by the superstructure. STM images recorded after annealing at intermediate temperatures show island formation. The images of figure 3.12 were taken after annealing at 1000 K for 120 s, corresponding to an AES peak asymmetry ratio of 1.6, approximately in the middle between the clean and the fully covered surface.

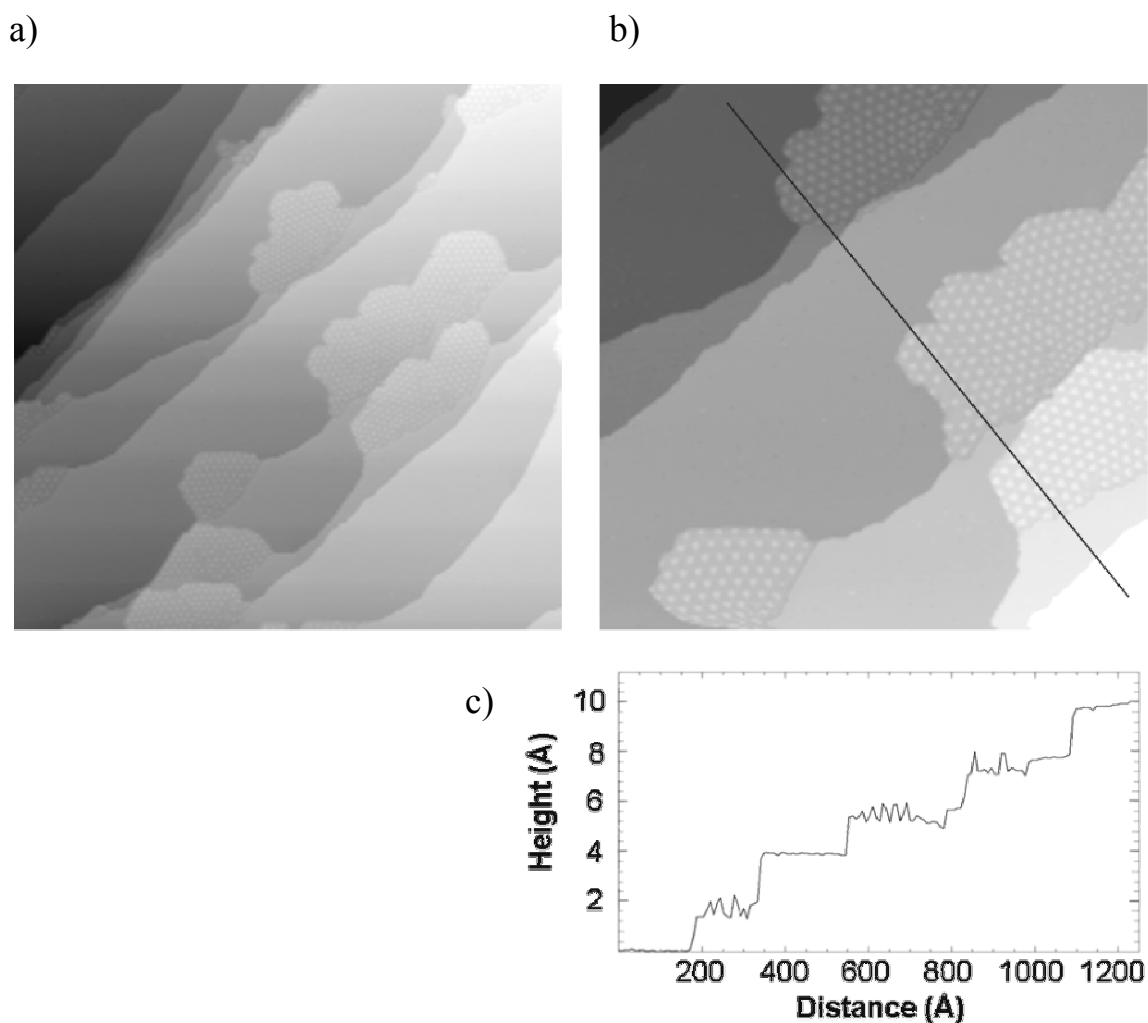


**Figure 3.12:** STM images recorded after annealing for 120 s at 1000 K corresponding to a ratio  $R \sim 1.6$ . The superstructure forms islands at the steps edges.  $I_t = 1$  nA,  $U = -0.5$  V. a) 200 nm x 200 nm. b) 100 nm x 100 nm. c) Line scan along the line displayed in b). The average island height is 1.8 Å above the ruthenium terraces. The superstructure displays a corrugation of about 0.7 Å.

The images show several metal terraces separated by monoatomic steps and islands revealing the superstructure. The islands display the same periodic overlayer as the structure in figure 3.4. Line profiles (figure 3.12c, corresponding to the line drawn in b) show the height modulation of the graphitic layer. The profile displays a monoatomic step of the metal at a distance of about 1100 Å from the origin showing a step height of 2.1 Å. This value is in agreement with the value expected for the Ru(0001) surface which confirms the calibration of the voltage-to-length conversion factor for the z signal. The corrugation amplitude of the overlayer amounts to 0.7 Å, corresponding to height oscillations of the islands above the metal terraces between 1.5 Å and 2.2 Å. The average height is 1.8 Å. Since, as pointed out in chapter one, STM images contain contributions

by both electronic and geometric effects it is not valid to interpret this value as geometric height of the graphite islands. The electronic structure of the uncovered surface is likely different from the graphitic layer. Because of this, the height difference between the graphite and the metal is most likely not identical to the real geometric difference. However, some qualitative considerations can be made. Compared to a metal, bulk graphite has a low density of states at  $E_F$ , and one may also expect the same for adsorbed graphene. Moreover, even if the work function for graphene on Ru(0001) (4.5 eV) is smaller than the work function for bare Ru(0001) (5.4 eV) [47], the effective tunneling barrier on graphite is probably larger than on the metal because only high  $\bar{k}_{||}$  states contribute to the tunneling current in the case of graphite [56]. The same effect is expected for a graphene layer overcompensating the lower work function. Both effects, lower density of states at  $E_F$  and higher effective tunneling barrier for graphene compared to Ru(0001), imply that, in order to measure the same tunneling current on bare metal areas and on graphene areas, the tip has to get closer to the surface over the graphene areas. For this reason the height of the graphene layer above the metal measured by STM is most likely lower than the geometric height. A rough estimate of the real geometric height of a graphene layer on Ru(0001) can be obtained considering a pure Van der Waals interaction between graphene and Ru. In this case one would expect to find 1/2 times the graphite interlayer distance (because the interlayer interaction in bulk graphite is mainly Van der Waals) ( $3.35 \text{ \AA} / 2 = 1.675 \text{ \AA}$ ) plus 1/2 times the ruthenium interlayer distance ( $2.14 \text{ \AA} / 2 = 1.07 \text{ \AA}$ ). The resulting value of  $2.75 \text{ \AA}$  is, as expected, higher than the value of  $1.8 \text{ \AA}$  measured by STM.

In any case, the STM value of  $1.8 \text{ \AA}$  clearly indicates that the islands are formed by single layers of graphite.

The islands in figure 3.12 are exclusively found at the lower step edges of the ruthenium, and are several hundred angstroms in diameter. This morphology is different from the graphene growth on Pt(111) induced by ethylene decomposition [50]. The decomposition of ethylene at 300 K on Pt(111) and the subsequent annealing to 900 K result in the initial formation of evenly spaced graphite islands, measuring 20-30  $\text{\AA}$  in diameter and distributed homogeneously all over the surface, even in the middle of flat terraces areas. After an annealing to 1070 K, the graphite starts accumulating at the lower step edges but many small islands remain on the terraces. Finally, annealing to 1230 K gives rise to the formation of large graphite islands both at the step edges and on the terraces. On ruthenium, on the contrary, it is observed that the nucleation starts at 1000 K at the step edges and proceeds on the lower terraces of the metal. Since in this case the source of carbon is evidently the bulk of the crystal it is possible that the step edges sites are the preferential sites for the carbon to segregate from the bulk to the surface. It is also possible that the steps act as nucleation centers as typically observed for defect sites and carbon, after segregation from the bulk, diffuses on the terraces to the step edges where the growth starts.

## II. Total coverage

After prolonged annealing at  $T \geq 1400 \text{ K}$ , the AES ratio R is about 2 and the surface is fully covered with the overlayer as previously shown (figure 3.4). Figure 3.13a displays the same situation on a stepped area of the surface.

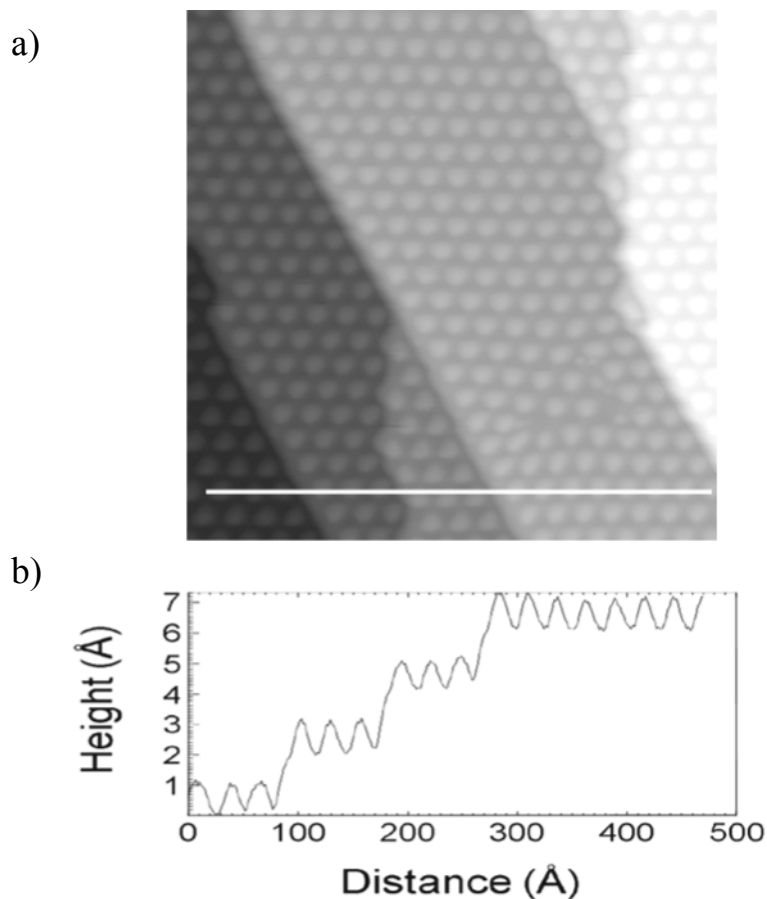


**Figure 3.13:** a) STM image recorded after annealing for 90 s at 1470 K. The surface is fully covered by graphene and six different terraces separated by steps are visible. The step edges are aligned along the main directions of the overlayer indicating a restructuring of the underlying Ru surface. 50 nm x 50 nm,  $I_t = 1$  nA,  $U = -0.2$  V. b) Height profile along the line displayed in a). The steps are 2.1 Å high and thus represent steps of the Ru(0001) substrate. The corrugation is about 1.2 Å.

Six different terraces separated by steps are visible. The line scan shown in (b) allow to measure the steps height which is the same for all steps and amounts to 2.1 Å, exactly the interlayer spacing of the (0001)-oriented Ru (2.14 Å), so that all steps must be steps of the Ru substrate. Graphite steps (3.35 Å) were never observed and even other type of surface structures like clusters that could indicate the presence of graphite multilayers were never present. It can be concluded that under the chosen preparation conditions the segregation of carbon is limited to a single graphene layer covering the entire surface. Effects that prohibit bulk growth could be of kinetic nature - the further segregation of carbon atoms below an existing coherent graphene layer is certainly energetically costly - or that the thermodynamic stability of bulk graphite is lower than that of dissolved carbon atoms in Ru.

The line profile in figure 3.13b also shows the pronounced corrugation of the superstructure which amounts to about 1 Å and will be analyzed below.

An interesting detail of figure 3.13a is the alignment of the steps along the main directions of the overlayer. Steps on bare Ru(0001) are typically bent with large radii [57], as also seen in the images of figure 3.12, but rarely show longer straight segments. Hence, the Ru surface restructures during the carbon segregation process to better adjust to the periodicity and orientation of the overlayer, indicating significant interactions between the graphene and the Ru surface.

### III. Atomic structure of the graphene layer

The STM images of figure 3.14 display the superstructure with atomic resolution. The long range structure due to the graphite layer is observed simultaneously with atomic features giving rise to what can be called “moiré pattern” [58]. Moiré patterns are interference patterns formed when two similar grids are superimposed. In the system formed by graphene on Ru(0001) the two grids are due to the metal substrate exhibiting a triangular lattice with lattice constant 2.706 Å (figure 3.15a) and the graphene layer with a honeycomb lattice with lattice constant 2.47 Å (figure 3.15b). When the graphene lattice is superimposed on the ruthenium lattice, the two different lattices come into coincidence every 11 unit cells of the metal or 12 of the graphene and the moiré pattern is observed (figure 3.15c). The resulting periodicity of the moiré structure is ~ 2.97 nm in agreement with the measurements without atomic resolution (previous paragraphs). Figure 3.14c displays a line scan along the line drawn in (a) and confirms these results. The superstructure has a period of ~3 nm and the atomic features have a distance of ~ 2.47 Å. The measurement of distances in STM usually has an error from thermal drift causing image distortions. For this reason, especially when measuring the distances of unknown structures, it is good to observe on the same STM image the presence of a known structure that can be used for calibration. Figure 3.16 shows the surface partially covered with the superstructure. The metal area is covered with CO molecules displaying the known  $(\sqrt{3} \times \sqrt{3})R30^\circ$  structure with a periodicity of 4.67 Å [59]. Using the CO structure as calibration for the distance measurement, the periodicity of the superstructure in the bottom left corner of the image can be precisely measured. The value obtained  $(2.98 \pm 0.03)$  nm is in agreement with the previous observations. The  $(\sqrt{3} \times \sqrt{3})R30^\circ$  CO structure is also useful to determine the crystallographic directions on the surface: the primary vectors of the Ru(0001) surface are rotated by 30° with respect to the unit cell of the CO structure. In this way the  $[10\bar{1}0]$  direction of ruthenium can be determined showing that the moiré runs parallel to this direction. This confirms that the  $[10\bar{1}0]$  direction of the graphite lattice is parallel to the  $[10\bar{1}0]$  of the ruthenium lattice as shown in the model of figure 3.15. This property is also confirmed by the fact that in the high resolution images of figure 3.14 the atomic features and the moiré pattern are parallel.

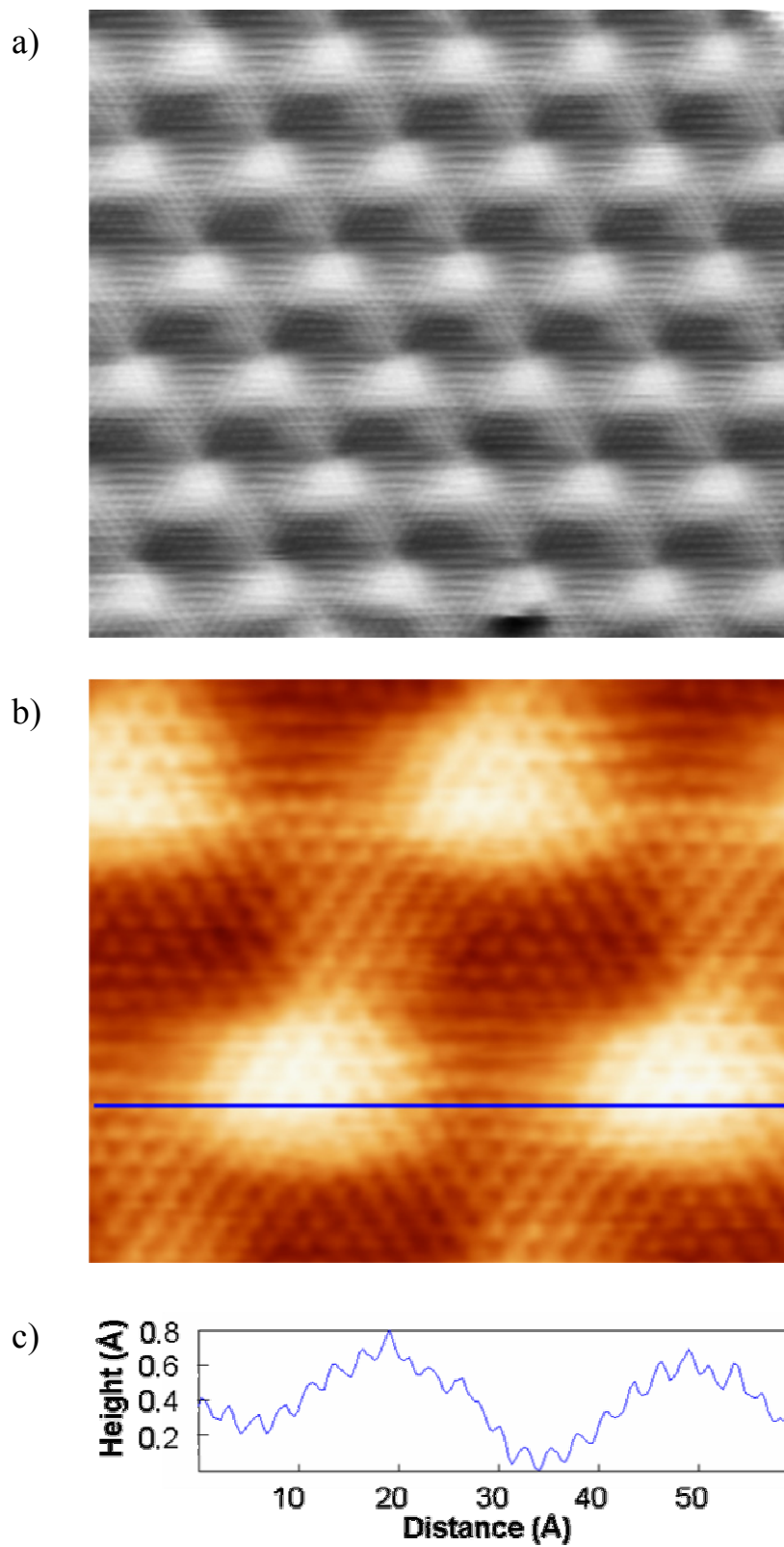


**Figure 3.14:** STM images displaying atomic resolution of the superstructure.  $I_t = 1$  nA,  $U = -0.05$  V. a) 15 nm x 13 nm b) 5 nm x 4 nm c) Line scan along the line shown in (b): the superstructure has a periodicity of 30 Å and the atomic features have a distance of  $\sim 2.46$  Å.

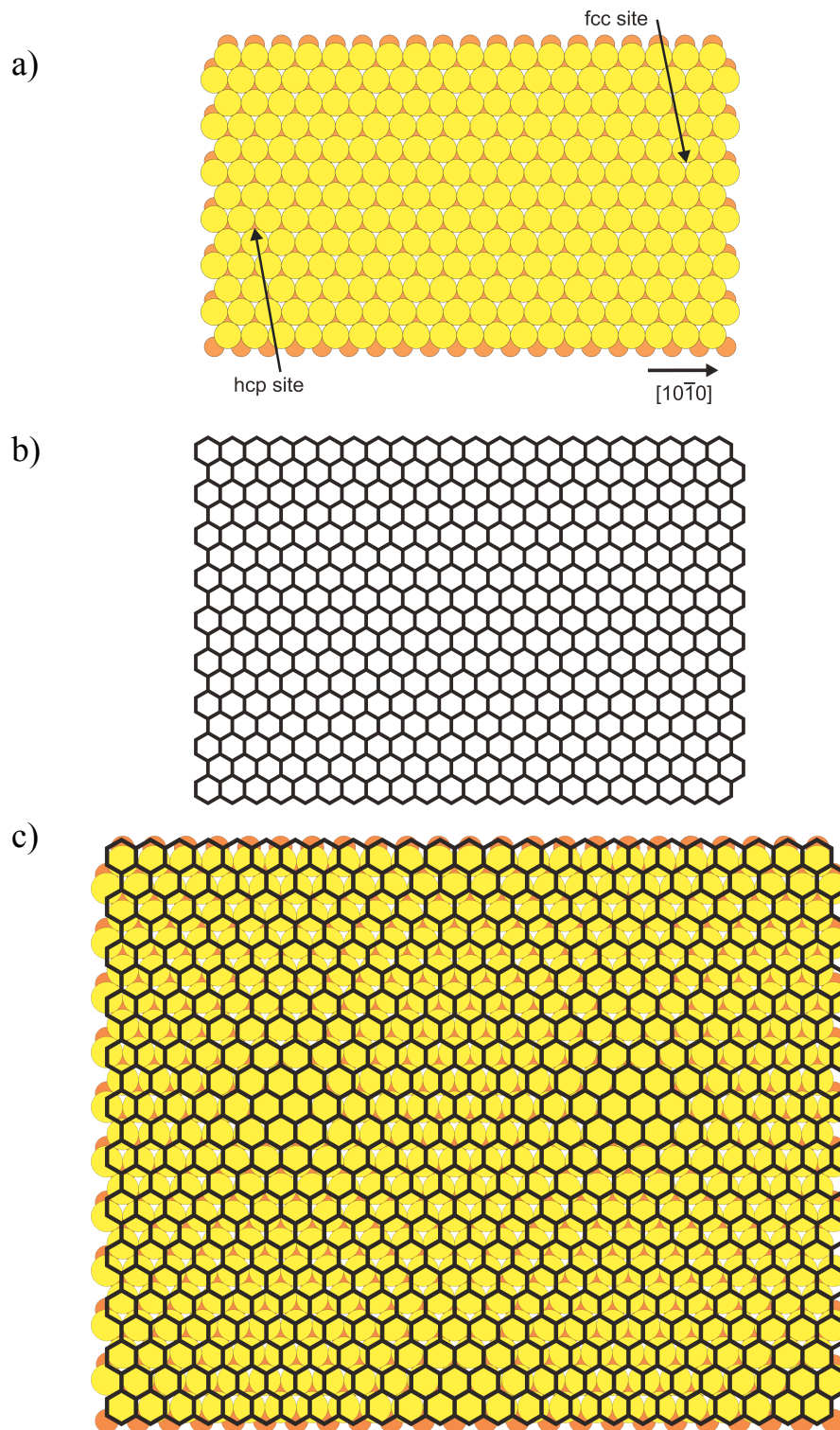


**Figure 3.15:** Models showing the formation of a moiré pattern. a) Triangular lattice representing the Ru(0001) surface. b) Honeycomb lattice describing a graphene layer. c) The superimposition of the graphene layer on the Ru(0001) lattice produces the moiré pattern. The two slightly different lattices come into coincidence every 11 substrate unit cells or every 12 graphene unit cells.

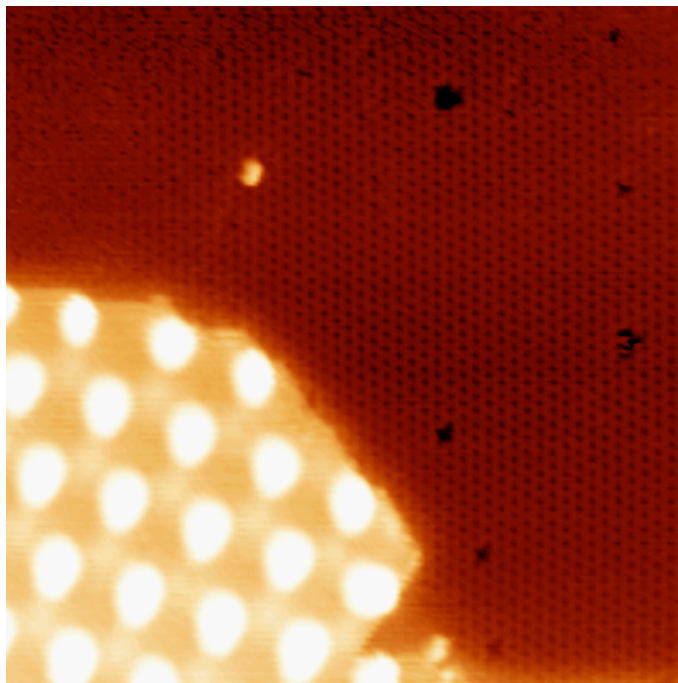


**Figure 3.16:** STM image displaying the surface partially covered with the superstructure. The metal area is covered by CO molecules forming the known  $(\sqrt{3} \times \sqrt{3})R30^\circ$  structure. The presence of the CO structure with its periodicity of  $4.67 \text{ \AA}$  is used as calibration to measure the periodicity of the superstructure. The precise result is  $(2.98 \pm 0.03) \text{ nm}$ .  $20 \text{ nm} \times 20 \text{ nm}$ ,  $I_t = 1 \text{ nA}$ ,  $U = -0.1 \text{ V}$ .

In some cases it was observed that the moiré structure and the graphene atomic features are rotated to each other by  $10^\circ$  like in the image of figure 3.17a. The rotational angle  $\beta$  between the two atomic grids is much smaller than this value. It is obtained by

$$\beta \cong \frac{a_{\text{Ru}} - a_{\text{C}}}{a_{\text{Ru}}} \alpha$$

respectively,  $\alpha$  the measured angle between the moiré pattern and the graphene lattice, and  $\beta$  the angle between the ruthenium and the graphene lattice [60]. The resulting angle  $\beta$  is  $1^\circ$ . This effect is shown in the model of figure 3.17b that also reveals that the periodicity of the moiré structure is not affected by this small rotation between the two lattices.

The uniformity and alignment of the structure is surprising. In contrast, graphene overlayers on Pt(111) behave differently, showing rotational angles between the two lattices ranging from  $0^\circ$  to  $90^\circ$  and periodicities of the superstructure varying between  $5 \text{ \AA}$  and  $22 \text{ \AA}$  [50].

It can be concluded that the long range periodic structure represents a moiré structure formed by superposition of 12 graphene unit cells and 11 unit cells of the Ru(0001) surface. This result is in good agreement with the LEED observation (figure 3.5) of a periodicity of  $11.6 \pm 0.2$  substrate lattice constants.

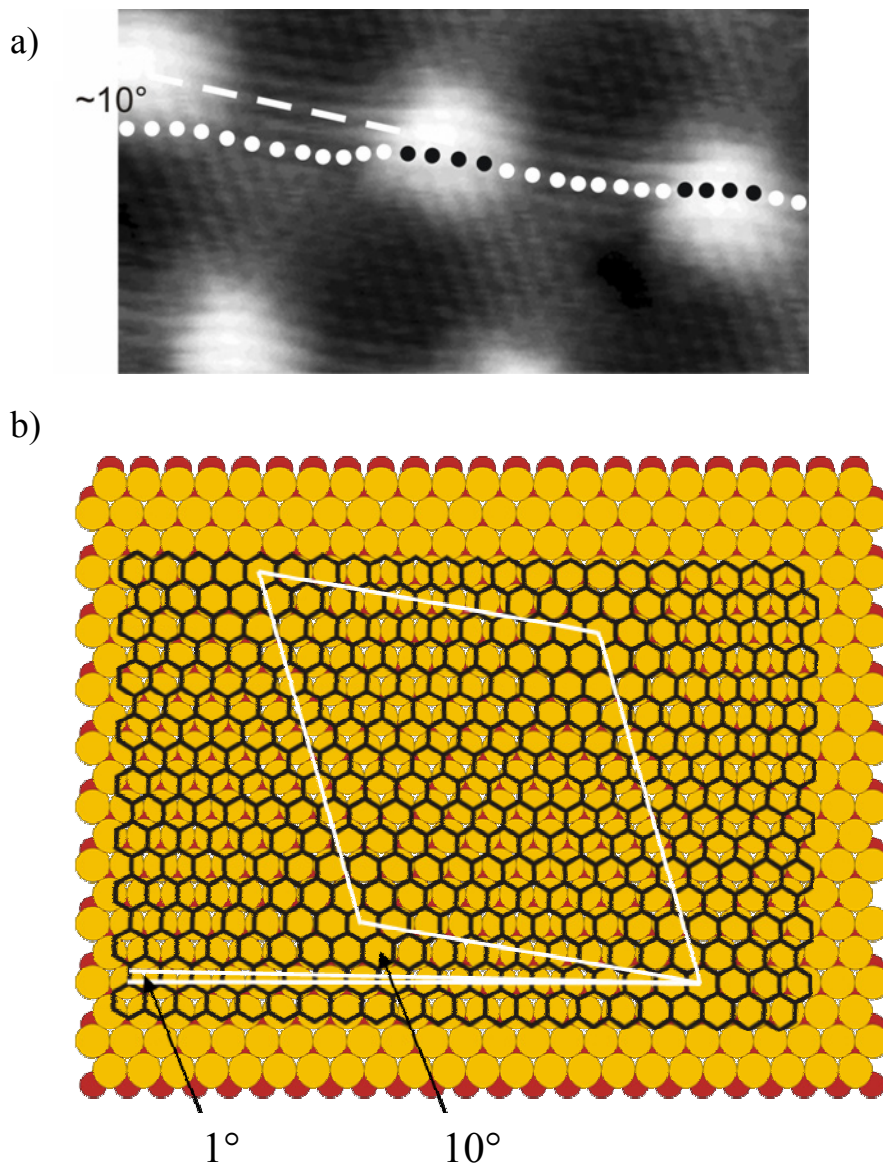


**Figure 3.17:** a) STM image with atomic resolution showing the moiré rotated by  $10^\circ$  degrees to the graphite lattice.  $8 \text{ nm} \times 4 \text{ nm}$ ,  $I_t = 3 \text{ nA}$ ,  $U = -0.05 \text{ V}$ . b) Model showing that a slight rotation ( $1^\circ$ ) of the graphene lattice to the ruthenium lattice results in the measured  $10^\circ$  rotations of the moiré structure. The periodicity of the moiré is unaffected.

The  $(11 \times 11)$  periodicity of the superstructure formed by graphene on Ru(0001) had been also concluded before from STM data without atomic resolution [55]. On the contrary, the previous observation of a  $(9 \times 9)$  structure by Grant and Hass can not be confirmed [54].

Figure 3.18 shows a schematic model of the unit cell in the simple and most common case of parallel ruthenium and graphene lattices. At the four corner of the unit cell the hexagons of the graphene honeycomb structure are centered around top sites of the underlying atoms of the ruthenium surface.

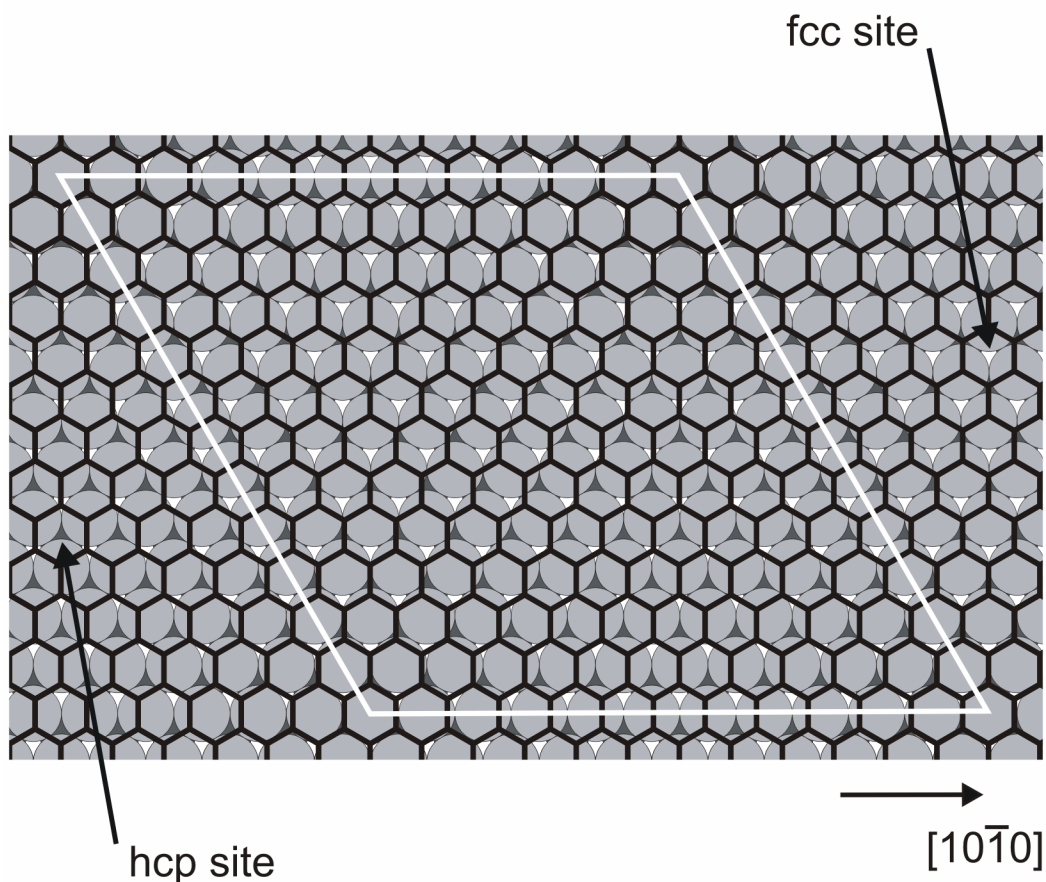


**Figure 3.18:** *Model of the unit cell of the superstructure.*

Across the cell the sites of the carbon atoms continuously shift with respect to the atoms of the Ru surface giving rise to the long range brightness modulation observed by STM. The unit cell is divided into two non-equivalent halves in the centers of which the graphene rings are differently arranged with respect to the two types of threefold hollow sites of the metal surface. In the upper left half of the unit cell the rings are centered around the fcc hollow sites, in the lower right half they are centered around the hcp sites. This difference is also observed in the STM images where, besides the moiré maxima, in every unit cell two non equivalent areas with different average gray levels can be distinguished.

STM images of stepped areas covered by the superstructure confirm this observation and provide a further proof for the model. The model of the Ru surface (figure 3.1) shows that, due to the hcp structure of ruthenium, adjacent terraces are different with respect to the orientations of the hcp and fcc sites. When the terraces are covered by the superstructure, the (11x11) unit cells must reflect this difference from one terrace to the other. This can be seen in figure 3.19. The STM image in (a) is the same image of figure 3.13a but displayed with enhanced contrast. The enlargement in figure 3.19b shows that

the unit cells of the moiré structure separated by a monoatomic step are indeed different. Each unit cell displays two halves, one in which the minimum between three bright maxima is almost black, and the second in which the minimum is less dark. In the unit cell on the left terrace, the black minimum is at the bottom right half of the cell, in the unit cell on the right terrace, the black minimum is at the upper left half of the cell. This switching of unit cells between neighboring terraces rules out a tip artifact. It can be concluded that the different appearance of the minima of the moiré structure in the STM data is real. It furthermore confirms the structure model of figure 3.18.

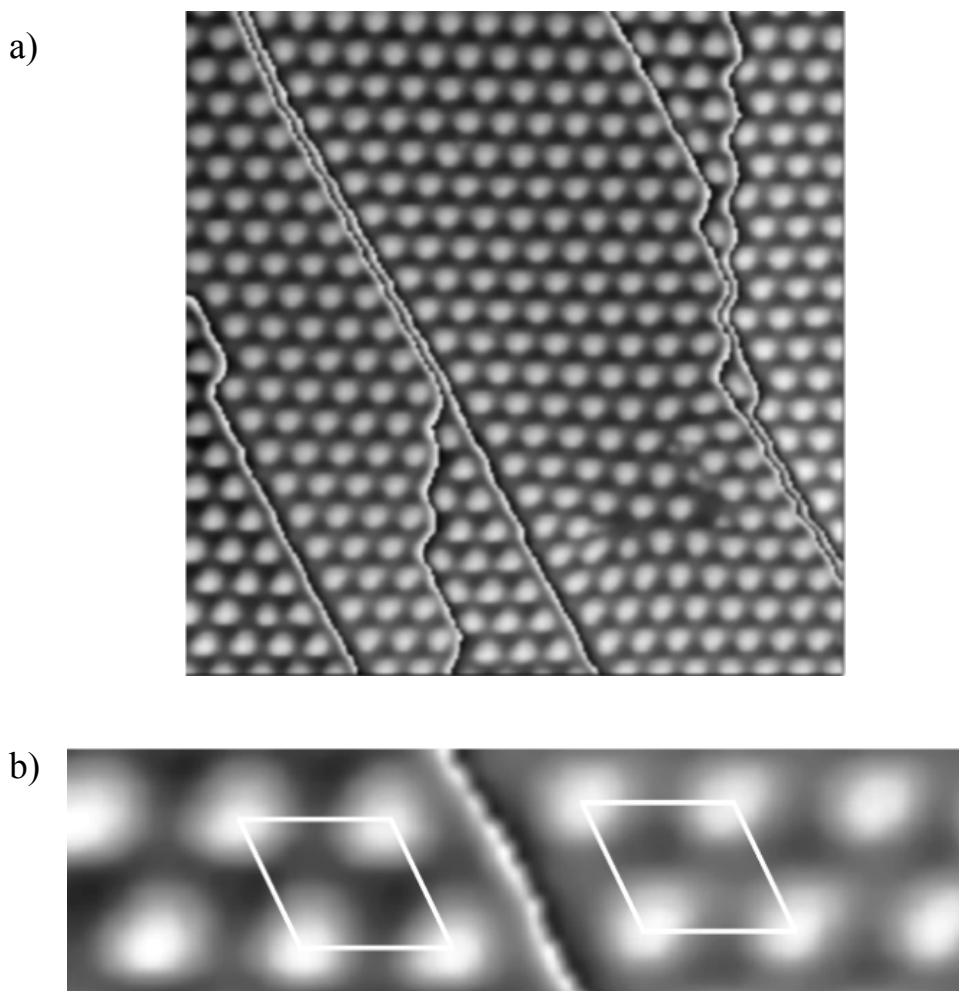


**Figure 3.19:** *a) The STM image of figure 3.13 displayed with greater contrast. b) Detail of (a) showing unit cells of the superstructure on adjacent terraces.*

#### IV. The two different C atoms in the graphene unit cell

Knowing that the unit cell of the moiré structure is formed by 12 x 12 graphene unit cells, the lattice of the graphene can be superimposed on the STM images in order to identify the atomic features visible in the STM measurements. In figure 3.20 the graphene lattice is superimposed on the image of figure 3.17b. The graphene lattice has a honeycomb structure described by a triangular lattice with two atoms per unit cell: in the figure the positions occupied by these atoms are depicted in red and in green. Close inspection of the image shows an important detail. The atoms that appear bright in the STM image are related to the positions that they occupy in the unit cell. At the maxima of the unit cell, the entire graphene rings appear bright with a depression in the middle. All six carbon atoms forming the graphene rings are measured as protrusions. In the darker minimum of the moiré unit cell the hexagons are not visible but only a triangular lattice. This lattice corresponds to the positions occupied by the carbon atoms marked green in the graphene lattice. In this area the red carbon atoms are not visible. On the contrary, in the less dark minimum of the moiré unit cell, the red atoms appear as protrusions forming a triangular lattice while the green atoms are not visible. Such a contrast shift from one type of carbon atom to the other with an intermediate imaging of both atoms has not been reported before. In particular, in bulk graphite only one of the two types of atoms is resolved in STM and the images showing atomic resolution exhibit a triangular lattice instead of the honeycomb structure [61-63]. In order to understand the reason for this phenomenon in bulk graphite, one has to consider its crystal and electronic structure. Graphite is formed by carbon atoms layers with a honeycomb structure stacked in an ABA configuration. Figure 3.21a displays a model of bulk graphite showing three layers. It is clearly visible that the surface exhibits two non-equivalent atoms. The A atoms, depicted in red, have a carbon atom directly below in the second layer while the B atoms, depicted in green, lie exactly above the centers of the hexagons in the second layer. This is also visible in the top view (figure 3.21b) which shows the graphite surface (hexagons with solid lines) and the second layer (hexagons with dashed lines). The B atoms occupy positions exactly above the centers of the underlying hexagons while the A atoms have a carbon atom directly below. Tománek and coworkers calculated that the presence of a carbon atom directly below an A type atom of the surface implies a weak interaction between the two atoms while the B type atoms do not interact with any underlying atom. This weak interaction results in a dispersive electronic band formed by wave functions localized on the A sites and thus in a low density of states on these sites (figure 3.22). In particular, at the K point of the surface Brillouin zone the electronic states of the A atoms are spread over approximately 1.2 eV around the Fermi level. On the contrary, since the B atoms do not interact, the wave functions localized on the B sites have a doubly degenerate band at the Fermi energy and a high density of states at the K point of the surface Brillouin zone [62]. Tománek also showed that, for tunneling voltages of about 0.5 V, the STM samples a very small fraction of the surface Brillouin zone of graphite around the K point [61]. This is due to the band structure of graphite that is characterized by the crossing of the  $\pi$  and  $\pi^*$  bands at the K point of the Brillouin zone giving rise to a single state at the Fermi energy that dominate the imaging by STM [56].

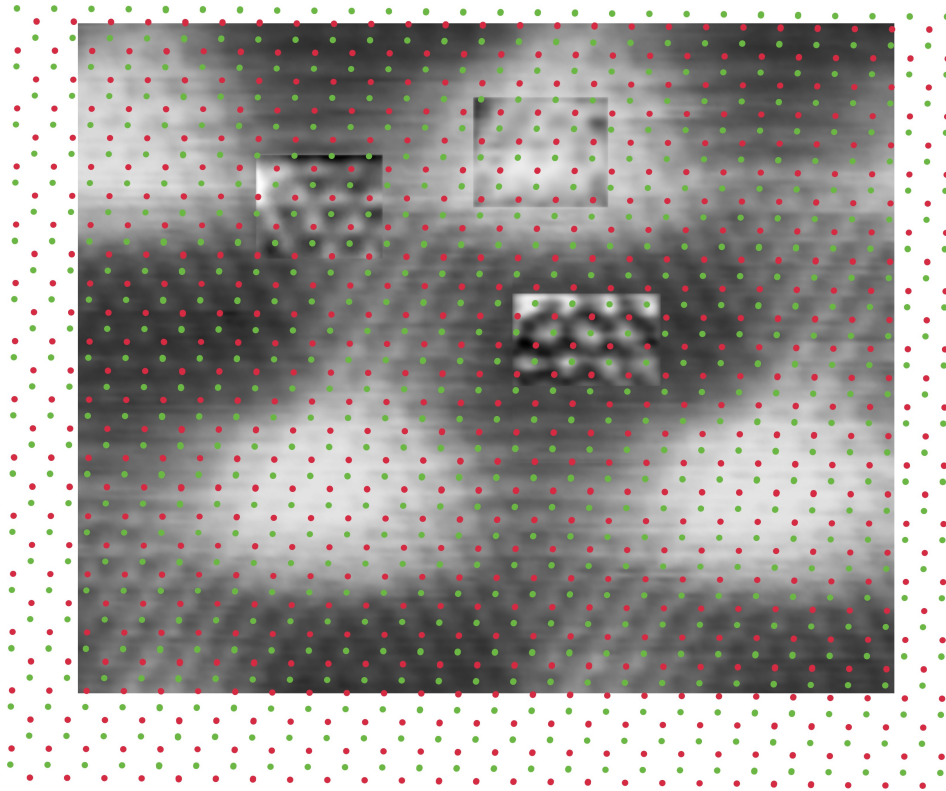


**Figure 3.20:** Honeycomb lattice of graphene superimposed on the STM image of figure 3.14. The graphene unit cell contains two atoms displayed in red and in green.

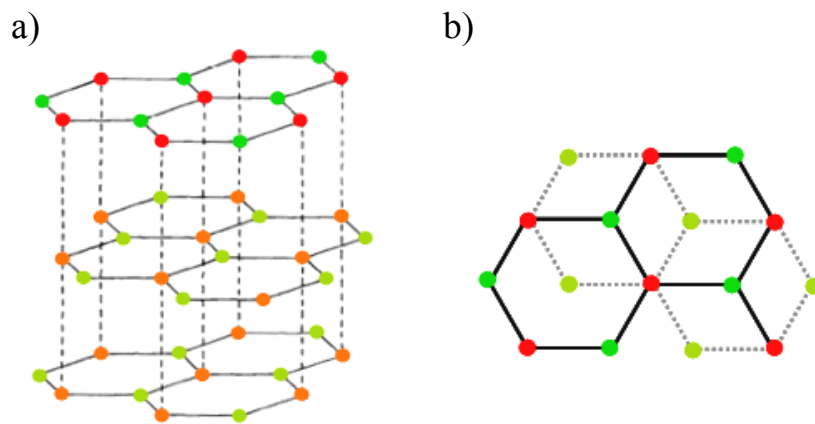


**Figure 3.21:** a) Model displaying 3 layers of graphite and showing the difference between atoms A, in red, and atoms B, in green. b) Top view of the graphite lattice.

Because the STM samples the surface Brillouin zone of graphite around the K point and because at this point the density of states of the A atoms is low and high for the B atoms, the protrusions observed by STM in the case of bulk graphite correspond to the B atoms. Such an atomic asymmetry has also been observed in STM measurements of graphene on Pt(111). Like in the case of bulk graphite only one type of carbon atoms forming a triangular lattice is visible [50]. For such a system the explanation by Tománek is not applicable because there are no defined positions of the two types of carbon atoms with respect to the underlying Pt lattice. For this reason other explanations for the atomic asymmetry of graphite in STM have been put forward. Some authors believe that the asymmetry is due to a charge density wave (CDW) state with a localization of the extra electronic charge on the B sites [64, 65]. Other authors advanced the hypothesis of a mechanical interaction between the STM tip and the carbon atoms with the B atoms showing a lower hardness than the A atoms and the tendency to be pulled up by the tip [66, 67]. A generally accepted solution for the asymmetry problem of graphite has not been reached yet.

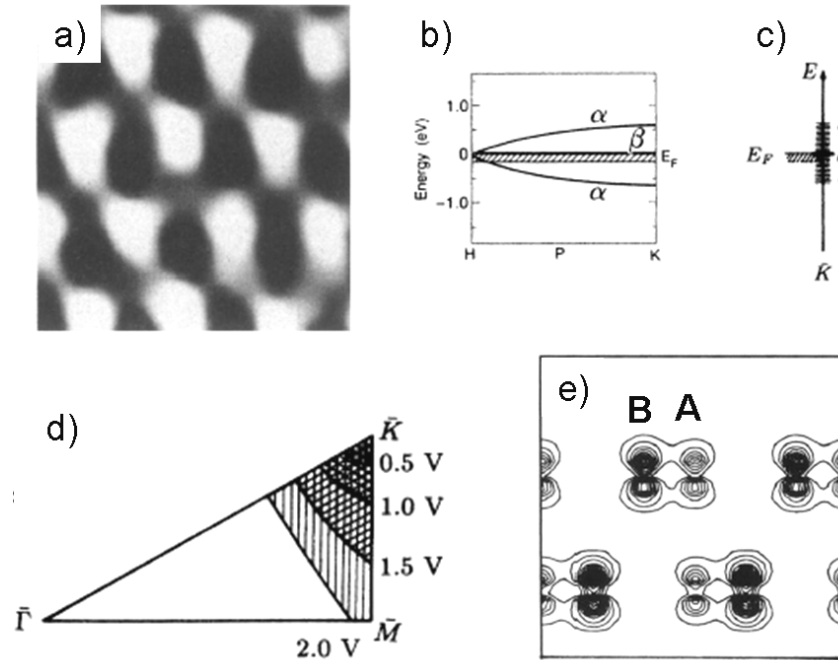


**Figure 3.22:** STM imaging of bulk graphite from ref. [61] a) Constant height STM image revealing atomic resolution. The bright protrusions form a triangular lattice while the entire hexagons of graphite are not visible.  $12 \text{ \AA} \times 12 \text{ \AA}$ ,  $U=0.1 \text{ V}$ . b) Schematic band structure of the  $\pi$  states of graphite along the P line in the Brillouin zone showing the dispersive band  $\alpha$  related to the A type atoms and the degenerate band  $\beta$  of the B atoms. c) Schematic band structure at the K point in the surface Brillouin zone of graphite:  $\alpha$  states are spread around the Fermi level exhibiting a low density of states while the  $\beta$  states are degenerate with a  $\delta$ -shaped density of states close to the Fermi energy. d) Fraction of the surface Brillouin zone sampled by STM at different bias voltages. For low voltages only the region around K is measured. e) Side view of the calculated STM charge density for two layers of carbon atoms in bulk graphite. The A atoms, which have a carbon atom directly below in the second layer, display a lower charge density than the B atoms explaining why only the B atoms are imaged as protrusions.

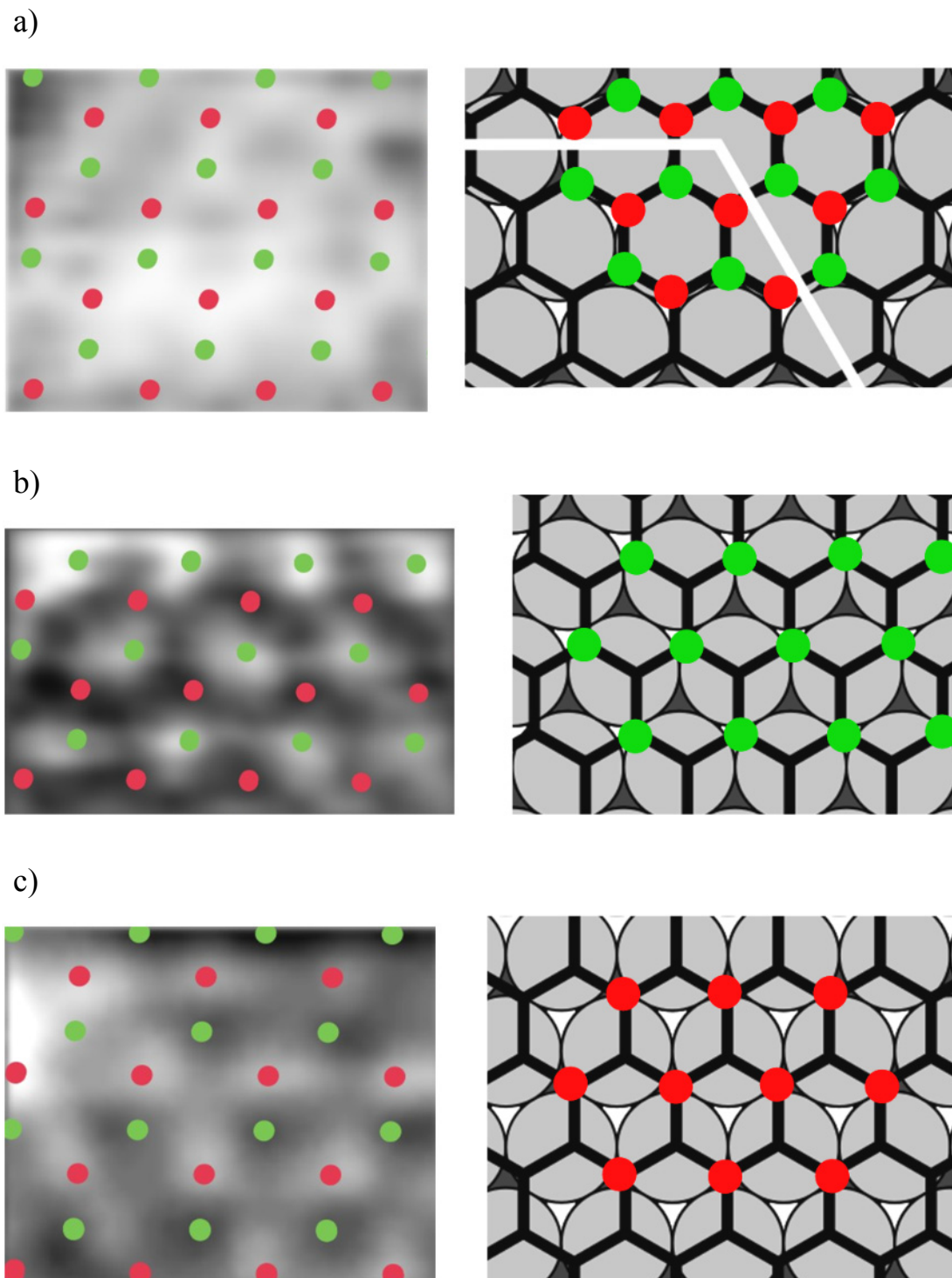


**Figure 3.23:** Areas with enhanced contrast of figure 3.20 and corresponding model enlarged from figure 3.15b. Each image corresponds to a high symmetry region in the unit cell: a) Maximum b) darker minimum c) less dark minimum.

The observations in the graphene/Ru(0001) system support an interpretation of the asymmetry in terms of interactions with the underlying layer. There is in fact a shift in contrast from one type of atom to the other depending on the position of the C atoms with respect to the ruthenium substrate. Based on the explanation by Tománek in terms of lower density of states for the carbon atoms interacting with underlying atoms, one would predict that in the case of graphene on Ru(0001) the carbon atoms with low density of states are those lying directly on top of the metal atoms while the atoms with a high density of states are those above threefold sites of the metal where the bonding to the substrate is less strong. This hypothesis is investigated in figure 3.23 where the three high symmetry regions of the moiré unit cells are shown together with the corresponding area in the model of figure 3.18. Figure (a) displays a maximum of the moiré unit cell where the entire rings of carbon atoms appear bright in the STM. In the related area of the model, it is clearly visible that the graphene rings are centered around the underlying Ru atoms and all six carbon atoms lie above the threefold hollow sites of the metal. Figure (b) shows the darker minimum region of the moiré unit cell with the protrusions forming a triangular lattice. In this case the bright atoms correspond to the positions of the green atoms while the red atoms are not visible. The corresponding model shows that the graphene rings are centered around the hcp sites of the metal, and the carbon atoms forming the rings lie alternatively above on top and fcc sites of the metal. The atoms on the fcc sites are the atoms depicted in green and seen as protrusions in STM. Finally, in (c) the less dark minimum of the moiré unit cell is shown with the protrusions forming a triangular lattice. Here the bright atoms are at the positions of the red atoms. In the corresponding model the graphene rings are centered around the fcc sites of the metal and the carbon atoms alternate between on top and hcp positions. The atoms above the hcp sites now are the red atoms. This explains the contrast shift from one type of C atoms to the other.

## V. The corrugation of the moiré

A further geometrical property is the corrugation of the moiré structure. Both in the images with and without atomic resolution this corrugation is pronounced and, as pointed out above, care must be taken interpreting the measured corrugation in the STM images as a real geometric corrugation. Figure 3.24 shows some of the STM images from the previous paragraphs with the line scans along the marked lines revealing the corrugation amplitude of the moiré structure. The corrugation ranges from  $\sim 0.6 \text{ \AA}$  to  $\sim 1.5 \text{ \AA}$ . From profile (c) it is visible that the height difference between the gray and the black area in the unit cell is  $0.5 \text{ \AA}$ .

The moiré corrugation is significantly larger than the geometric buckling of  $0.27 \text{ \AA}$  that was calculated for the graphene layer on Ir(111) [68] and this might suggest that electronic effects different from the Ir case might play a role in our system.

There are similar systems to the graphene/Ru(0001) system that exhibit pronounced corrugations comparable to the corrugation measured in our STM experiment. Corso and coworkers studied the deposition of hexagonal boron nitride (h-BN) on Rh(111) [69].

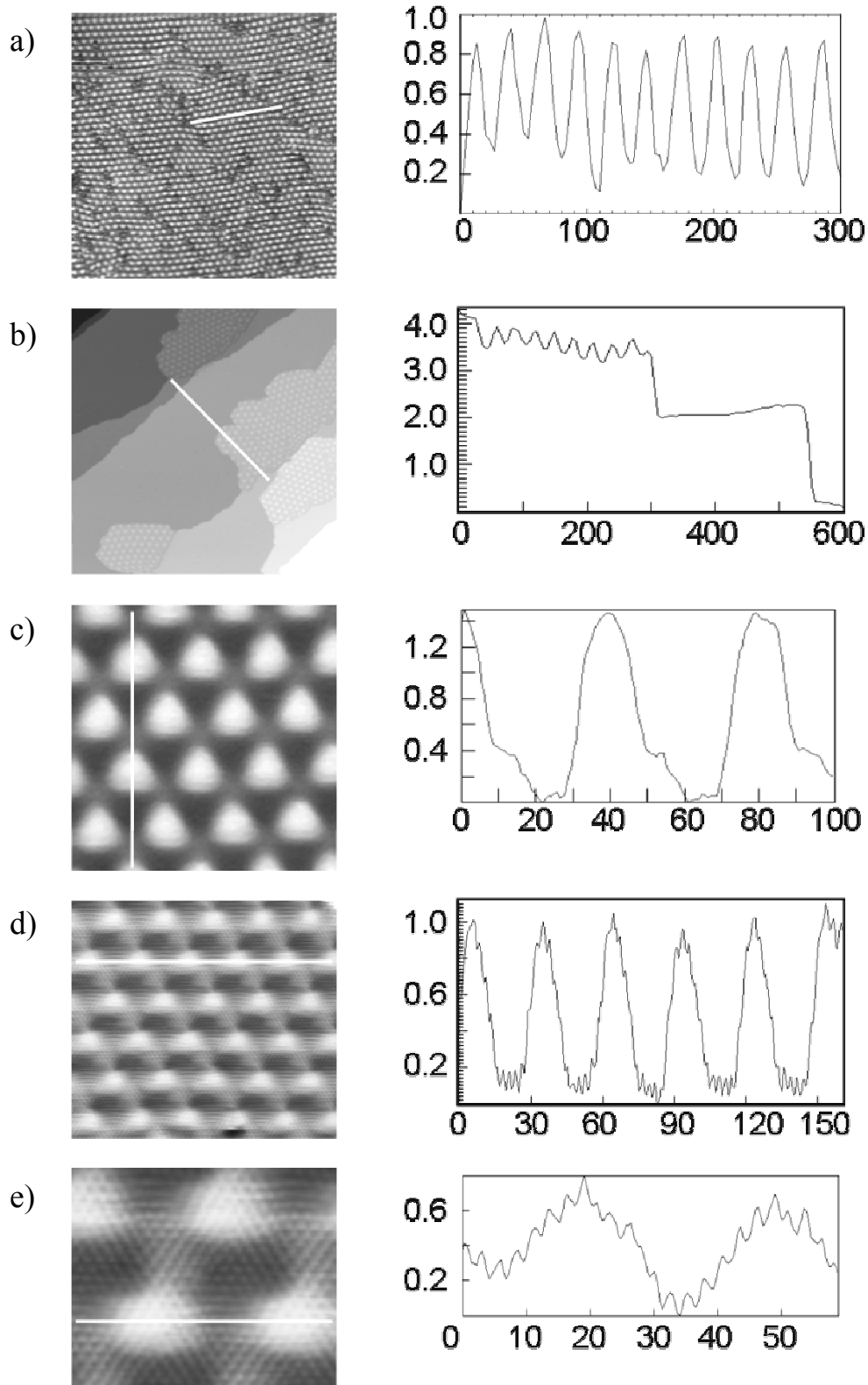


**Figure 3.24:** STM images and related line scans showing the corrugation of the moiré structure in the various cases. The x-axis display the distances in  $\text{\AA}$  and the y-axis the height in  $\text{\AA}$ .

A single layer of hexagonal boron nitride has the same structure as graphene, with one B and one N atom in each unit cell instead of the two C atoms. h-BN on Rh(111) forms a superstructure with  $\sim 30$  Å periodicity corresponding to a supercell of  $13 \times 13$  BN cells on  $12 \times 12$  Rh cells. In the STM height profiles a corrugation of  $\sim 1$  Å was reported. A recent theoretical study has shown that the h-BN layer on Rh(111) is highly corrugated with a predicted real geometrical corrugation of  $0.55$  Å due to the position of the BN rings with respect to the underlying metal layer [70]. A recent STM measurement shows that h-BN on Ru(0001) forms a very similar structure to the one on Rh(111) with a periodicity of  $32.5$  Å consisting of  $13 \times 13$  BN cells on  $12 \times 12$  Ru cells [71]. The apparent STM corrugation of this structure measures  $(0.7 \pm 0.2)$  Å. Because of the similarity between the two structures, it is reasonable to assume that the high STM corrugation reported for h-BN/Ru(0001) corresponds to a real geometrical corrugation as in the case of h-BN/Rh(111). It can therefore be concluded that the corrugations measured for graphene/Ru(0001) largely reflect real geometric corrugations as well. Finally, from the profiles on the images with atomic resolution, the atomic corrugation is about  $0.2$  Å, in good agreement with the  $0.21$  Å hard-wall corrugation amplitude measured by He atom scattering for bulk graphite [72].

## VI. Discussion

The surprisingly perfect orientation of the  $(11 \times 11)$  graphene structure on the Ru(0001) surface, the absence of other moiré phases, and the restructuring of the metal underneath the full monolayer suggest a substantial interaction between graphene and ruthenium. The interaction must be considerably stronger than the interlayer bond in bulk graphite, following from the fact that multilayer segregation does not occur during completion of the monolayer. A further hint at stronger chemical bonds than Van-der-Waals interactions between the metal and the graphene layer is the apparent height of the graphite islands above the metal measured in STM. Even considering that this value is affected not only by the geometry but also by electronic effects, the value of  $1.8$  Å is nonetheless much smaller than the van der Waals distance of  $2.75$  Å. Quantitative data about the interaction strength between graphene and metal surfaces are only available from the most recent work on Ir(111) [68]. An adsorption energy of  $200$  meV per carbon atom was obtained by calculations, a considerably higher value than the  $50 \div 60$  meV interlayer binding energy in bulk graphite [73]. In an early theoretical work on graphene/Ru(0001) no stable adsorption of the layer was found, but this may be due to the artificial  $(1 \times 1)$  structure that had been used [74]. LEED-IV studies of the graphite monolayer grown on Ni(111) determined an interfacial spacing of  $2.11$  Å– $2.16$  Å, for C atoms lying in on top and fcc sites of the metal, respectively [75]. However, for Ni(111) the graphene and metal lattice constants are almost identical, and the graphene overlayer accordingly forms a  $(1 \times 1)$  structure. On the contrary, for Pt(111) and Ir(111), which also form moiré structures with large unit cells, the spacing between the graphene and the metal are, on the average,  $3.70$  Å [76] and  $3.77$  Å [68], respectively. Hence, the short bonding distance for the graphene/Ru(0001) moiré structure is surprising. UPS measurements [47] and theoretical calculations [77] have shown that the binding energy between the C  $2p_z$  states and the Ru

surface is higher (by about 2 eV) than the binding energy of the C  $2p_z$  states in bulk graphite. Moreover, HREELS measurements of graphite on Ru(0001) [55], and also for graphene on Ni [78] and on transition metal carbide surfaces [79, 80], have shown a significant softening of the optical modes compared to the corresponding modes in bulk graphite. This observation indicates a weakening of the C-C bond in the honeycomb lattice due to the stronger interaction of the layer with the substrate than in bulk graphite. The nature of this interaction has been explained in terms of orbital hybridization between the  $\pi$ -states of graphite and the d-states of the metal [81, 82].

The data suggest a generally stronger interaction between graphene and various surfaces than the van-der-Waals interlayer interaction in graphite, but do not explain why Ru(0001) should be special. Here one can argue that, if the graphene-metal interaction actually has a covalent contribution, the same arguments about trends in bond strength as for chemisorbed atoms and molecules can be used [83]. The so-called “d-band model” developed by J. Nørskov predicts stronger metal adsorbates bonds from right to left of the rows of transition metals in the periodic table and from bottom to top. Ru should form stronger bonds than Ir and Pt because the Ru d-band lies higher in energy so that, after the bonding to an adsorbate orbital, more antibonding adsorbate-metal states are emptied than in the case of Ir or Pt. Ni, as a 3d metal, forms relatively strong bonds, too, but, in the case of graphene adsorption, the strength of the bond might be also influenced by the favorable (1x1) geometry.

### 3.2.4 Electronic structure

#### I. Voltage dependent images

STM data taken at varying tunneling voltages show that electronic effects are important. Figure 3.25 shows a series of images of the same area at bias voltages between -0.6 V and + 1.4 V (the sign refers to the sample). For -0.6 V (figure 3.25a) the typical moiré image is seen, a long-range hexagonal pattern of bright protrusions with triangular shape and with the two different minima, one appearing black, the other one less dark. Similar images were obtained between -2.0 V and -0.2 V and are typical for the filled states. At small positive voltages (+0.6 V, figure b), corresponding to empty states, the maxima become flat and develop bright rims. At more positive voltages (figure 3.25c to f) the previous maxima become darker, finally turning into minima, and pronounced bright rings develop. The truncated appearance of the rings at intermediate voltages is probably an effect of an asymmetric tip and was not present in other measurements. Figure 3.26 displays line scans over the maxima of 4 moiré unit cells at varying voltages. The line is shown for simplicity only in figure 3.25a. At -0.6 V the typical pronounced corrugation ( $\sim 1.1$  Å) of the superstructure is measured. At +0.6 V the corrugation is 0.6 Å. 0.2 Å due to the rims, 0.4 Å is the depth of the minima. With increasing voltage the rims become more and more pronounced (up to  $\sim 0.5$  Å) while the previous maxima turn into minima. At +1.4 V the apparent height of the rings is  $\sim 0.4$  Å.

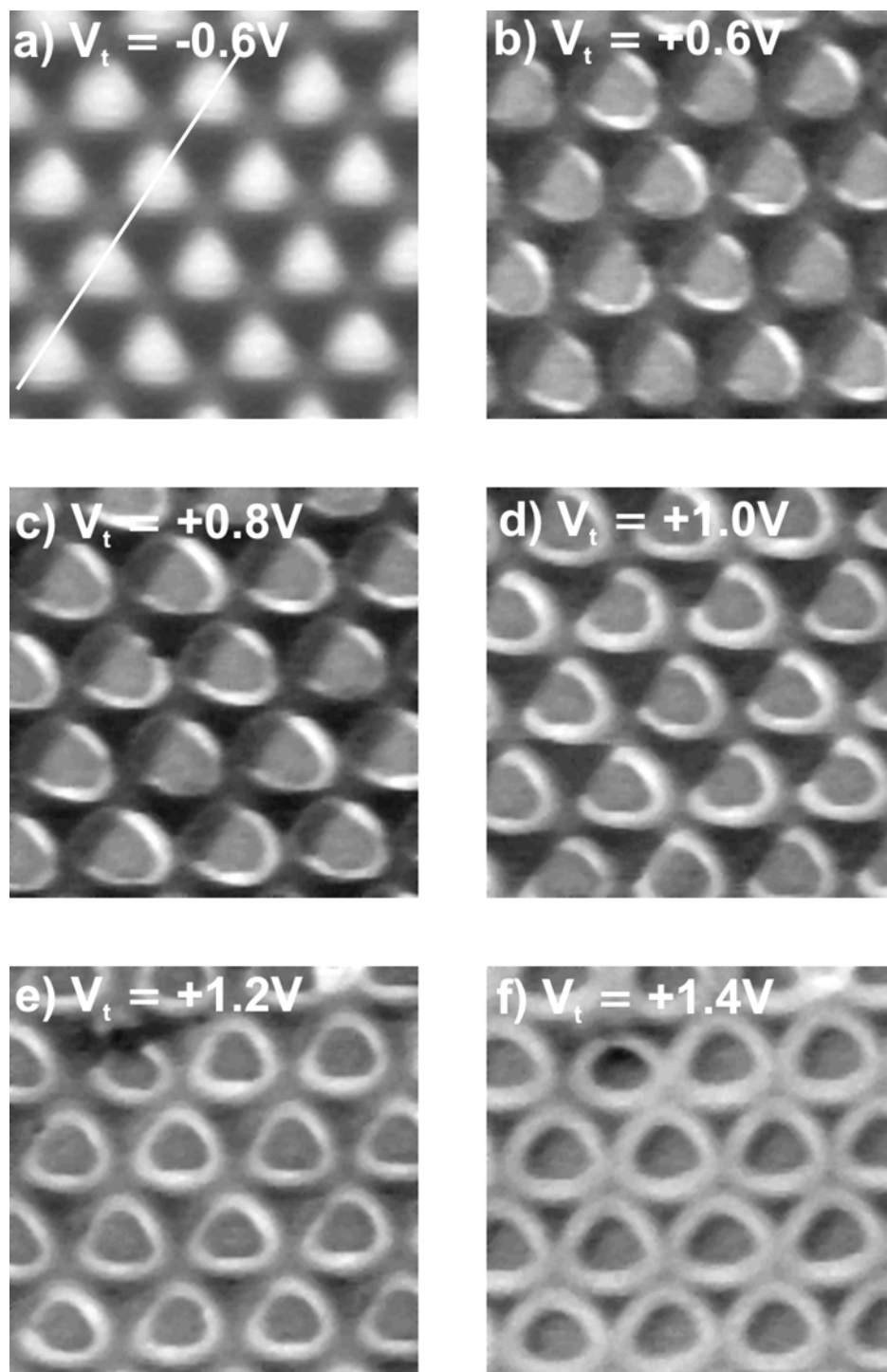


**Figure 3.25:** STM images taken on the same area at varying bias voltages at 55 K. The sign refers to the sample, the tunneling current is the same in all images ( $I_t = 1$  nA). The appearance of the moiré changes from a hexagonal pattern of maxima for the filled states to bright rings for the empty states. The truncated appearance of the rings at intermediate voltages is probably an effect of an asymmetric tip. 10 nm x 10 nm.

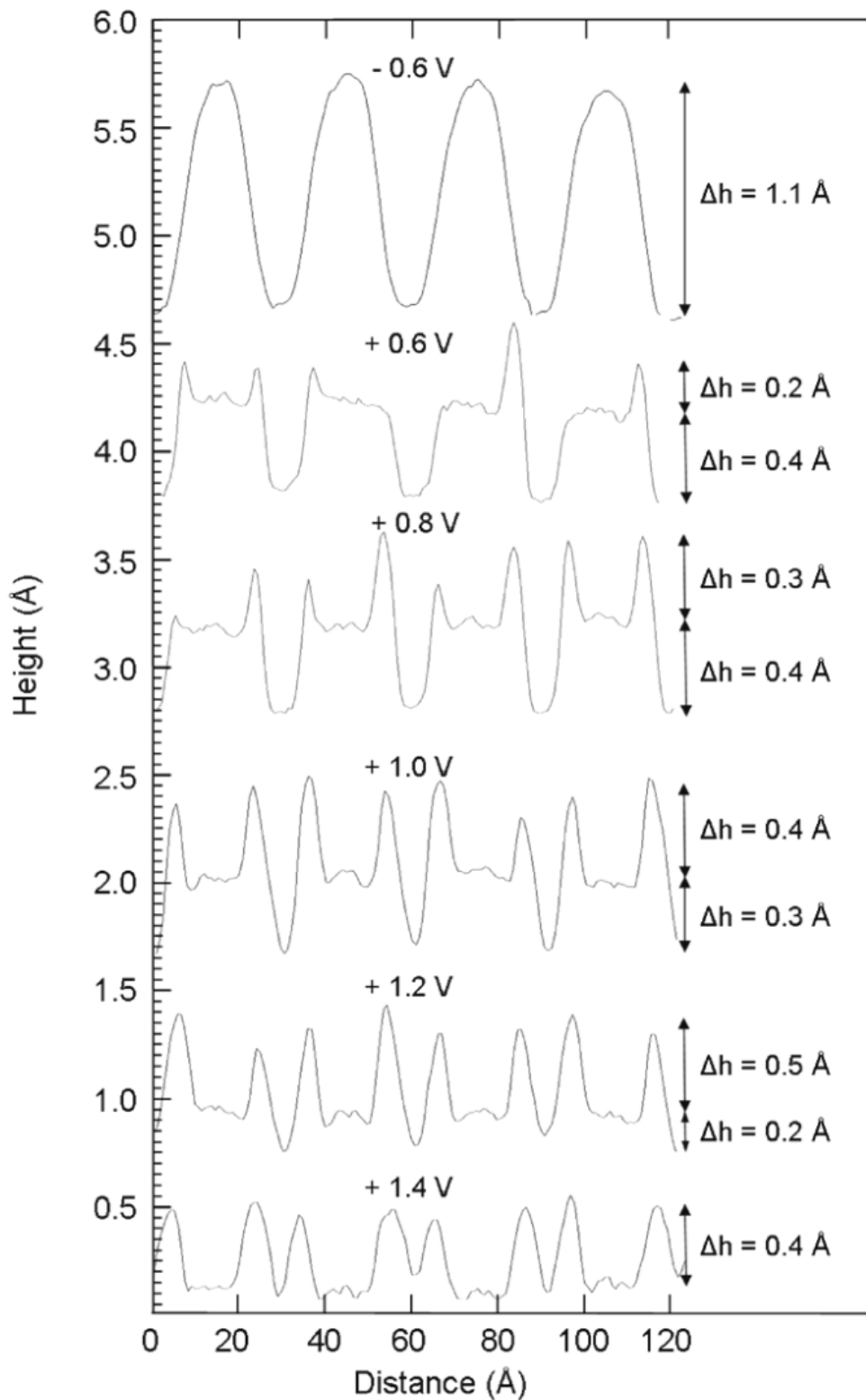


**Figure 3.26:** Height profiles showing the formation of the rings. The profiles are measured along the line shown in figure 3.25a and along the same line in figures 3-25b-f.

Figure 3.27 clearly shows that the rings appear around the maxima of the moiré structure. The STM image is taken with a constant tunneling current of 3 nA while the tunneling voltage is switched from -1.0 V to +1.0 V in the image centre. In the upper part of the image, measured at -1.0 V, the typical moiré pattern is visible. When the polarity is switched, the rings clearly appear around the maxima of the moiré.

This phenomenon shows that the imaging of the moiré structure is dominated by electronic effects, so that the measured height modulation of the long-range structure has no direct relation to the geometry. These measurements were performed at 55 K where the effect was easily visible. At room temperature it was difficult to obtain good data at positive voltages, but no systematic investigation of the temperature dependence was made. Such an effect has not been seen before for other graphene systems. Surprisingly similar images were observed for boron nitride films on Rh(111) that were originally interpreted as an indication of a double layer structure of the overlayer [69]. However, it was recently shown by theoretical calculations that h-BN on Rh(111) has a very similar monolayer structure as graphene on Ru(0001) [70] and for this reason the “rings effect” in the STM images of both systems might have the same nature.

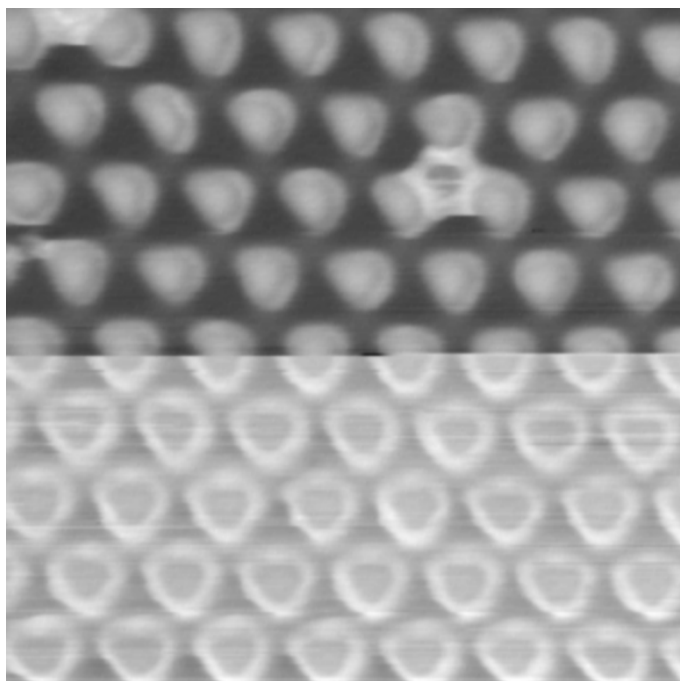


**Figure 3.27:** STM image showing that the rings appear around the maxima of the moiré structure. The image is taken at 55 K with a tunneling current of 3 nA. The bias voltage is switched from +1.0 V to -1.0 V in the centre of the image. 20 nm x 20 nm.

## II. Scanning tunneling spectroscopy measurements

To gain more information about the electronic structure of the adsorbed graphene layer scanning tunneling spectroscopy (STS) data were taken. Current Imaging Tunneling Spectroscopy (CITS) measurements were performed, measuring simultaneously the topography of a selected area in the constant current mode and a mesh of I-V curves directly related to the topographic features by interrupting the feed-back loop. First, spectra taken on the metal area were compared with those measured on the graphene covered areas. Secondly, it was tried to compare the spectra taken at different locations on the moiré structure to see a possible correlation to the rings in the topographic data. Finally, following a procedure introduced by Feenstra and coworkers [25], the decay length of the electronic states and the work function on the metal and on the graphene areas were measured.

### II a. Graphene versus Metal

Figure 3.28 shows the image of a graphene island and the surrounding metal and the superimposed grid where the STS data were taken. Every point corresponds to a single spectrum and, for the purpose of the analysis, the spectra were averaged across the graphene part and separately over the metal area. Defects and the immediate graphene/metal edge region were excluded. As figure 3.28b shows, the  $dI/dV$  spectrum on the metal area is structureless, as expected for a metallic surface where the density of states at a distance from the surface is dominated by s-states. In contrast, the graphene area shows two states in the spectrum, one at approximately -0.4 V and a second at +0.2 V. Since these states are absent on the metal it is obvious that they are caused by the graphene and not by some electronic state of the tip.

From the literature the electronic structure of adsorbed graphene layers near  $E_F$  is not very clear, and a definite interpretation of these measurements can presently not be offered.

For an isolated graphene layer the  $\pi$  and  $\pi^*$  bands intersect right at the K point of the Brillouin zone, giving rise to a single state at the Fermi energy [84]. A representation of the calculated band structure of a graphene layer is shown in figure 3.29a. The bands structure is taken from ref. [82], and the  $\pi$  and  $\pi^*$  bands are highlighted. These bands lie close to the Fermi level and are thus accessible by the STM/STS measurements. In the image it is clear that the bands cross at the Fermi level exactly at the K point of the Brillouin zone where a single state is present. This property is largely preserved for bulk graphite (except for the above discussed small dispersion perpendicular to the layers) where it determines to a large extent the imaging by STM [56]. For graphene adsorbed on several metal surfaces basically two changes were observed by ultra-violet photoelectron spectroscopy and obtained in calculations: a downshift of the  $\pi$  system by 1 to 2 eV with respect to  $E_F$ , and a reorganization of the electronic structure at the K point.

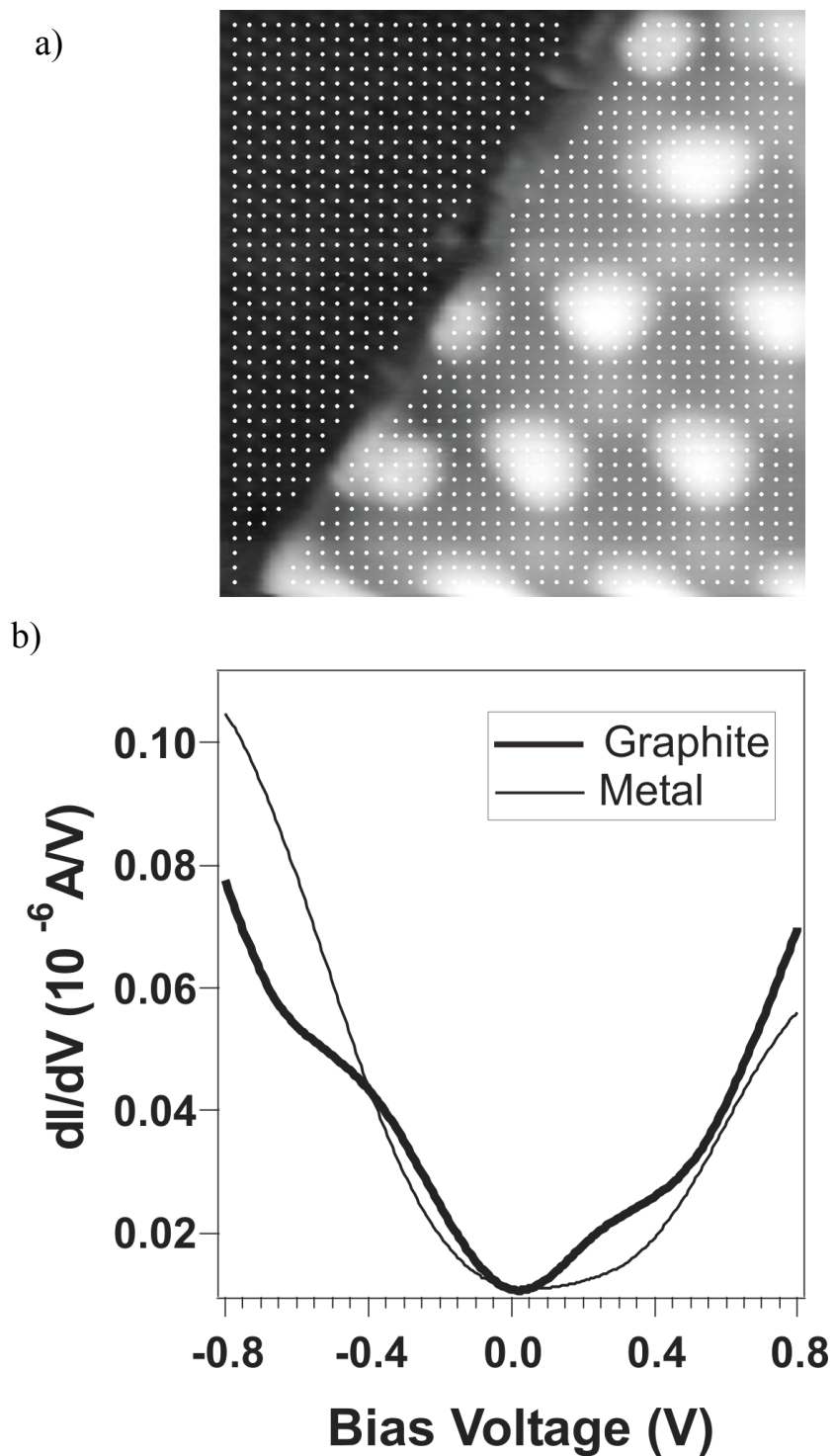


**Figure 3.28:** STS measurements at the edge of a graphene island and on the surrounding metal surface. a) Topographic image with superimposed grid where the spectra were taken.  $I_t = 1$  nA,  $V_{\text{offset}} = -0.4$  V, 10 nm x 10 nm. b) Averaged  $dI/dV$  spectra on the graphene area and on the metal. The graphene spectrum shows two peaks at  $-0.4$  V and  $+0.2$  V.

Systems studied were: Ru(0001) [47], Ni(100) [49], Ni(111) [85], TiC(111) [86], TaC(111) [87], Ni(111) [88]. Souza and Tsukada calculated the band structure for the (1x1) graphene overlayer on Ni(111) and the results are shown in figure 3.29b. The carbon bands with  $\pi$  character lying close to the Fermi level are highlighted again [82].

The hybridization of the graphite bands with the bulk nickel bands and the perturbation potential of the nickel substrate are responsible for the opening at K of an energy gap of about 1.0 eV centered at 0.8 eV below Fermi. A possible explanation for the two states observed in STS is that they represent the edges of such a gap resulting from the bond formation to the metal. These states are separated by 0.6 eV and the centre of the gap lies  $\sim 0.1$  eV below Fermi. It appears that the effect of the substrate-graphite interactions is weaker in the case of Ru(0001) than for Ni(111). This could be due to the fact that graphene forms a moiré structure on Ru, for which the average interaction with the metal is less strong, while in the case of Ni(111) graphene forms a (1x1) structure with all carbons atoms sitting on threefold hollow sites.

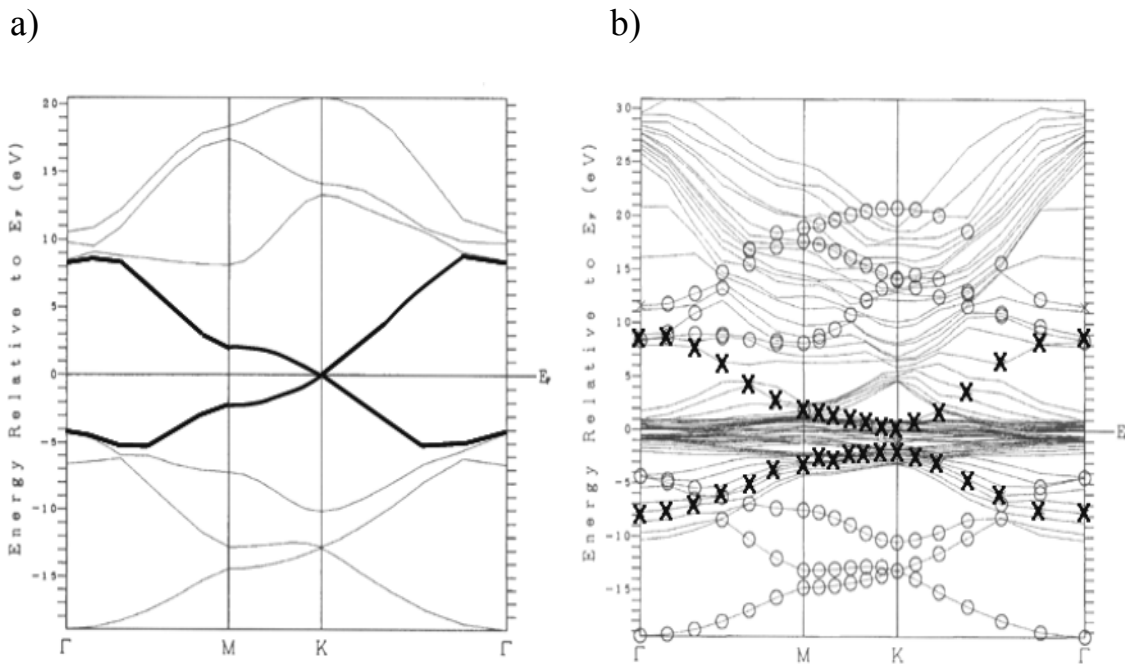


**Figure 3.29:** Calculated band structure for an isolated graphene layer (a) and for a graphene layer epitaxially grown on a Ni(111) surface (b) from ref. [82]. (a) The  $\pi$  and  $\pi^*$  bands lying close to the Fermi Level are highlighted. (b) The bands with carbon character are marked by circles and crosses. The crosses refer to the  $\pi$  and  $\pi^*$  bands that do no longer cross at the K point. On the contrary, the opening of a band gap is observed. The gap is about 1.0 eV, and it is centered at 0.8 eV below Fermi.

## II b. STS at different locations of the graphene layer

In order to obtain more insight into the peculiar electronic structure of the Ru(0001)/graphene system, tunneling spectra were recorded on different locations of the moiré unit cell (i.e. avoiding the spatial averaging over the entire layer).

Figure 3.30 displays the results of spectroscopy measurements at three different locations on the moiré structure under conditions where the rings appear, namely at the minimum of the unit cell (curve A in green), on the ring (curve B in blue) and at the centre of the rings (curve C in red) corresponding to the maxima of the moiré. The main difference is the shape of the I-V curve: in figure 3.30b it is clearly visible that curve A is symmetric whereas B and C display a more pronounced negative going behavior towards negative tunneling voltages. In the positive tunneling voltages region, the three curves are almost identical. In the  $dI/dV$  curves these differences reflect in a symmetric shape for the spectrum at the location A and an asymmetric shape at B and C.

Although these data can not yet be interpreted in a consistent picture, they demonstrate spatial variations of the electronic structure across the moiré unit cell. A collaboration with M. L. Bocquet (École Normale Supérieure de Lyon) who is performing DFT calculations has been started to resolve this issue, but the large unit cell is already a challenge for a DFT study. Results have to be awaited. The spatial variations from figure 3.30 suggests that the bonding of the graphene layer to the metal varies across the unit cell, which, considering the structure model and the contrast shift between the two atoms in the graphene cells, is not surprising.

What might also play a role for the imaging of graphene is a 2D free electron-like state that, according to calculations for isolated graphene, has density-of-states maxima above and below the layer [89]. For bulk graphite this state turns into a surface state that was identified by inverse photoelectron spectroscopy at +3.6 eV (at  $\Gamma$ ) [90]. STS data of bulk graphite displayed peaks in the same energy range, although the interpretation was somewhat controversial [91, 92]. Because of the spatial distribution of the electron density this state should play a role for the interaction of graphene with a surface, and one may therefore expect an energy shift and a contribution to the tunneling current even at lower energies. The strange electronic effects observed by tunneling into empty states could thus possibly also be connected with this surface state.

However, there are further effects in the STM data that are not directly related to topographical features but to electronic properties. Possible effects in the present case are charge density waves (CDW) and image potential states.

Charge density waves are characteristic for low dimensional metals (quasi-1D or 2D) and are caused by electron-phonon coupling. Basically, the atomic equilibrium positions forming the periodic lattice of the metal change and, together with the electron gas, lead to a modulation with a larger periodicity than the atomic lattice. The cost of elastic energy is compensated by a gain in electron energy and which increases as the temperature of the metal decreases. For this reason CDW are observed below a critical transition temperature  $T_P$  (Peierls temperature). The transition results in a new electronic band structure characterized by a gap at the Fermi level.

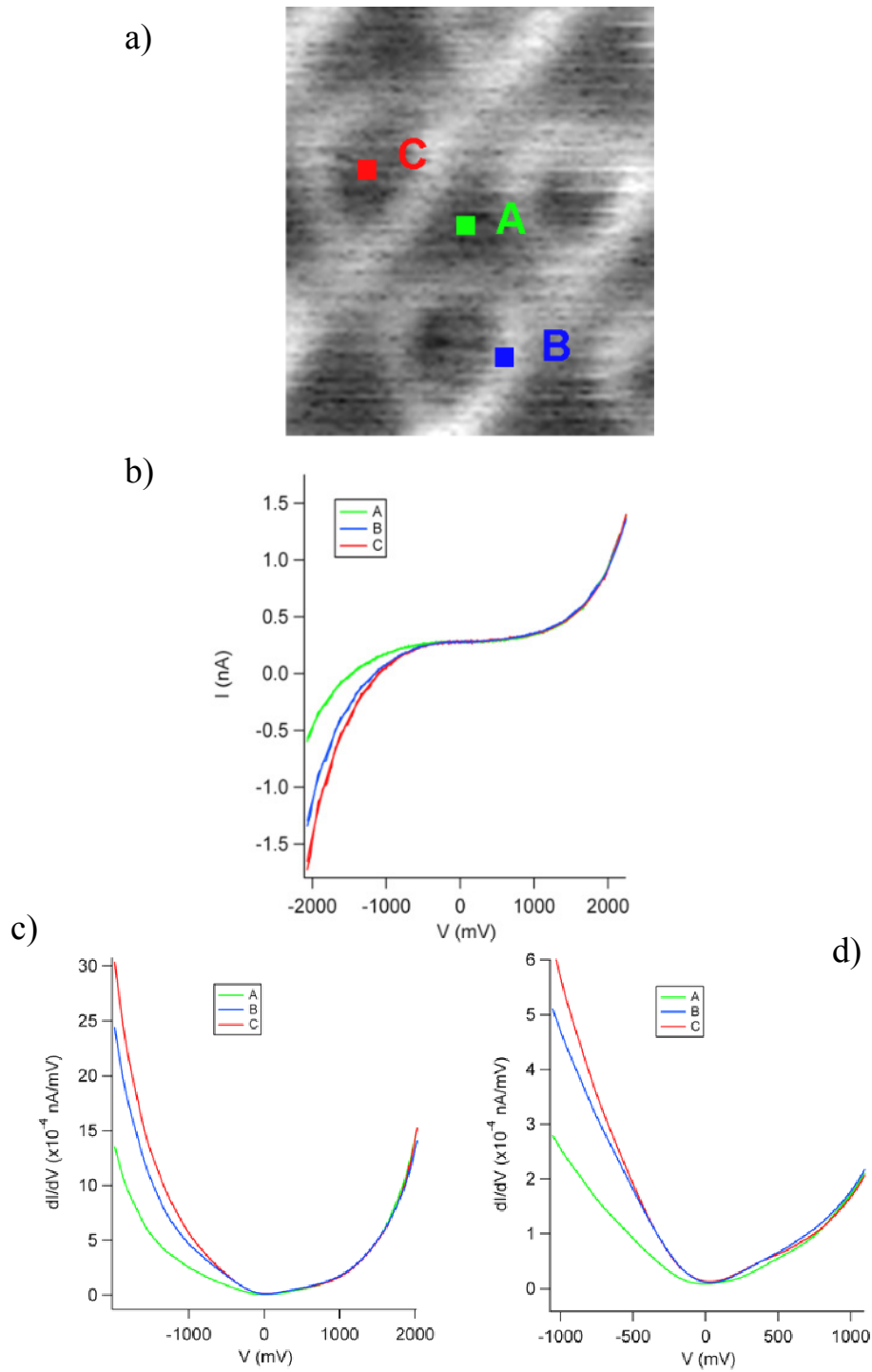


**Figure 3.30:** STS measurements on different locations on the moiré structure under conditions where the rings appear. a) Topographic image.  $I_t = 0.1$  nA,  $V_{\text{offset}} = +1.0$  V,  $3.5$  nm  $\times$   $4.5$  nm. b) Averaged  $I/V$  spectra on the three locations marked in (a). Spectrum A has a symmetric shape while spectra B and C have a pronounced negative going behavior towards negative tunneling voltages. c)  $dI/dV$  curves. d) Enlargement of the  $dI/dV$  curves.

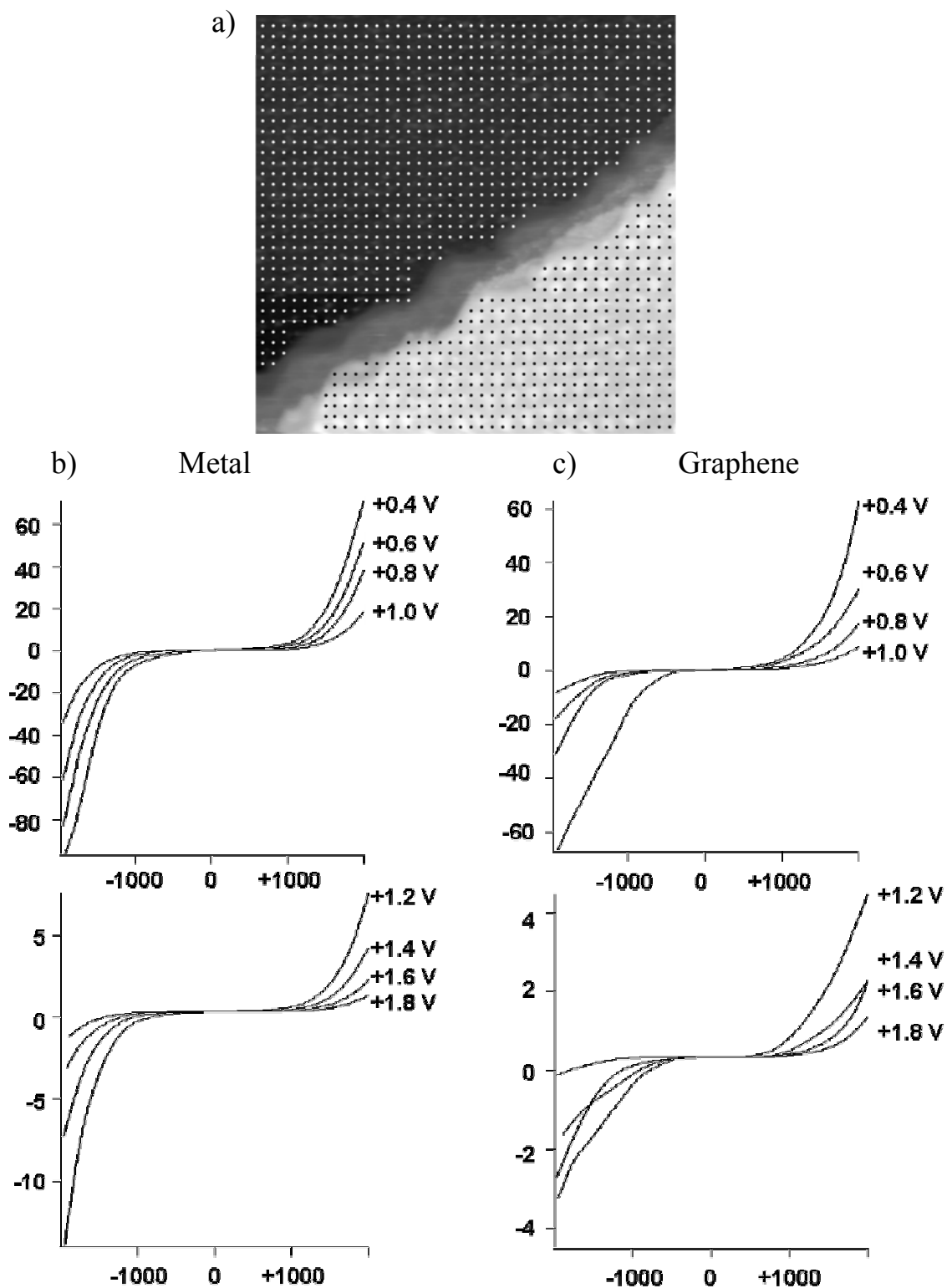
The effect has been observed in a large class of transition metal-chalcogenides such as NbSe<sub>2</sub> [93], NbSe<sub>3</sub> [94], TaS<sub>2</sub> [95], TaS<sub>3</sub> [96], and the resulting STM images taken below  $T_P$  and with tunneling voltages at the edges of the band gap reveal superimpositions of the atomic and the charge density wave periodicities [97]. However, typical values for the energy gap due to the CDW transitions are of the order of 50 meV or lower. For this reason it is improbable that the moiré structure and in particular the “rings” effect in the STM images of graphene/Ru(0001) is due to a charge density wave. The effect appears in fact for tunneling voltages above 500 mV implying an energy gap one order of magnitude larger than typical CDW gaps.

Image potential states are quantized electron states existing in front of many metal surfaces [98]. An electron in front of a conducting metal surface experiences an attractive force identical to that produced by a positive (mirror image) charge inside the metal. If the metal has a partial band gap near the vacuum level, an electron below the vacuum level experiences the Coulomb-like attractive image potential and a repulsive surface barrier. This results in the formation of quantized electronic states forming Rydberg-like series similar to the hydrogen atom series that converge at the vacuum energy. In STS experiments these states result in strong oscillations in the  $dI/dV$  curves due to transmission resonances of the tunneling electrons at the voltages where the image potential states occur [99, 100]. Recently it was shown that image potential states play an important role in STM imaging of ionic overlayers forming moiré phases such as FeO on Pt(111) [101] or NaCl on Ag(100) [102]. However, the image potential states typically have energies of several eV, so that they become visible (in the images and in STS) at tunneling voltages of the order of the work function of the sample and the tip. For this reason, an explanation of the STS structures and of the rings in the STM images of graphene on ruthenium in terms of surface potential states is not convincing. The bias voltages of the STS features and of the images changes are much lower than the work function of graphene/Ru(0001) (= 4.5 eV [47]) and of the tungsten tip (= 5.2 eV [103]).

### III. Decay length

In a paper by Feenstra and coworkers it was shown that scanning tunneling spectroscopy can be employed not only to measure the density of states of the sample but also to determine the inverse decay length  $K$  of the tunneling process [25]. Since the electronic states in the surface Brillouin zone that carry the tunneling current have different decay length according to their  $\vec{k}_{||}$  vector, the decay length provides information about the wave vector of the contributing states. The basic idea behind this method, which will be briefly described, is to combine the I-V measurement with a V-z measurement of the tip displacement  $z$  as a function of the bias voltage  $V$ . In this way I-z curves are obtained that can then be used to determine the decay length.

With CITS (Current Imaging Tunneling Spectroscopy), the topography of the surface is measured together with a set of I-V curves by interrupting the scanning and the feedback loop at precise and known positions on the scanned area. As a consequence, all I-V curves in one measurement are measured at a fixed tip-sample distance  $z$  that is determined by the tunneling parameters.



**Figure 3.31:** a) STM topography of the area where the measurement is performed.  $I_t = 1$  nA,  $V_{\text{offset}} = -0.7$  V,  $30$  nm  $\times$   $30$  nm. b) and c)  $I$ - $V$  curves for several tip-sample distances on the metal (b) and the graphene (c) area. The tip-sample distance is varied by changing the offset tunneling voltage as indicated beside the spectra.

By performing a series of CITS measurements at varying offset bias voltages one obtains a series of I-V curves measured at different tip-sample separations. An example of such a series of I-V curves is shown in figure 3.31. Figure 3.31a displays the topography of an area partially covered by graphene where the experiment was performed. Figures (b) and (c) show the I-V series for the metal and the graphene parts, respectively, measured at different tip-sample distances. Eight CITS measurements were performed on the same area with the same set point for the tunneling current ( $I_t=1$  nA) and at different offset bias voltages (+0.4 V, +0.6 V, +0.8 V, +1.0 V, +1.2 V, +1.4 V, +1.6 V, +1.8 V). In each measurement the tip-sample distance was adjusted by the feedback loop such that the tunneling current was 1 nA. Hence, when the bias voltage is increased from +0.4 V to +1.8 V, the tip-sample distance increases because at high voltages more states contribute to the tunneling current so that the tip has to retract to keep the tunneling current constant at 1 nA. The data on the metal area and those on the graphene area were averaged separately to obtain separate curves for the metal and for graphene. The averaged curves are fitted with the smoothing spline tool as described in chapter 2. Figure 3.31b and (c) show for simplicity only the smoothed curves. From this series of I-V curves the tunneling currents were extracted at a sequence of voltages between -2.0 V and +2.0 V for each of the eight tip-sample separations. This procedure was performed for every curve in steps of 0.1 V.

In order to measure the tip-surface separation  $z$  as a function of the bias voltage  $V$  it is additionally necessary to record the  $z$  signal of the feedback loop (i.e. the change of tip-surface distance) when the offset bias voltage is changed [104]. The measurement was performed several times on the area shown in figure 3.31a, both on the graphene and the metal region, and the results were then separately averaged. Examples of the V- $z$  curves obtained in this way are shown in figure 3.32.

The tunneling current was kept fixed at 1 nA, and the vertical displacement  $z$  of the tip was recorded during a voltage ramp from +0.2 V to +2.7 V. From these curves, the tip displacements at each voltage between +0.2 V and +2.7 V are obtained and in particular at the eight voltages at which the I-V curves were taken. On the metal area the tip performs a vertical displacement of 1.9 Å when the bias voltage is increased from +0.4 V to +1.8 V. On the graphene area, the tip displacement is 1.6 Å for the same voltage range. Finally the tunneling current values from the I-V data from figure 3.31 are plotted as a function of the tip displacement  $z$  (from figure 3.32) on a logarithmic scale (figure 3.33). Figure 3.33a displays the results for the metal area that clearly show a linear behavior. Furthermore, the lines corresponding to voltages between -1.8 V and +1.8 V are all parallel. Figure 3.33b shows the data from the graphene area. The data at a tip-sample distance of 1.15 Å (I-V curve in figure 3.31c measured at an offset bias voltage of +1.4 V) appear to be affected by a systematic error (visible also in the I-V spectra in figure 3.31c) and are not considered in the analysis. All other data lie on straight lines like on the metal, but in the case of graphene the slopes of the lines vary, reflecting different decay lengths.

From the expression for the tunneling current  $I \propto e^{-2Kz}$ , the inverse decay length  $K$  is obtained from the slope  $m$  of the linear regression:  $2K = -m$ .

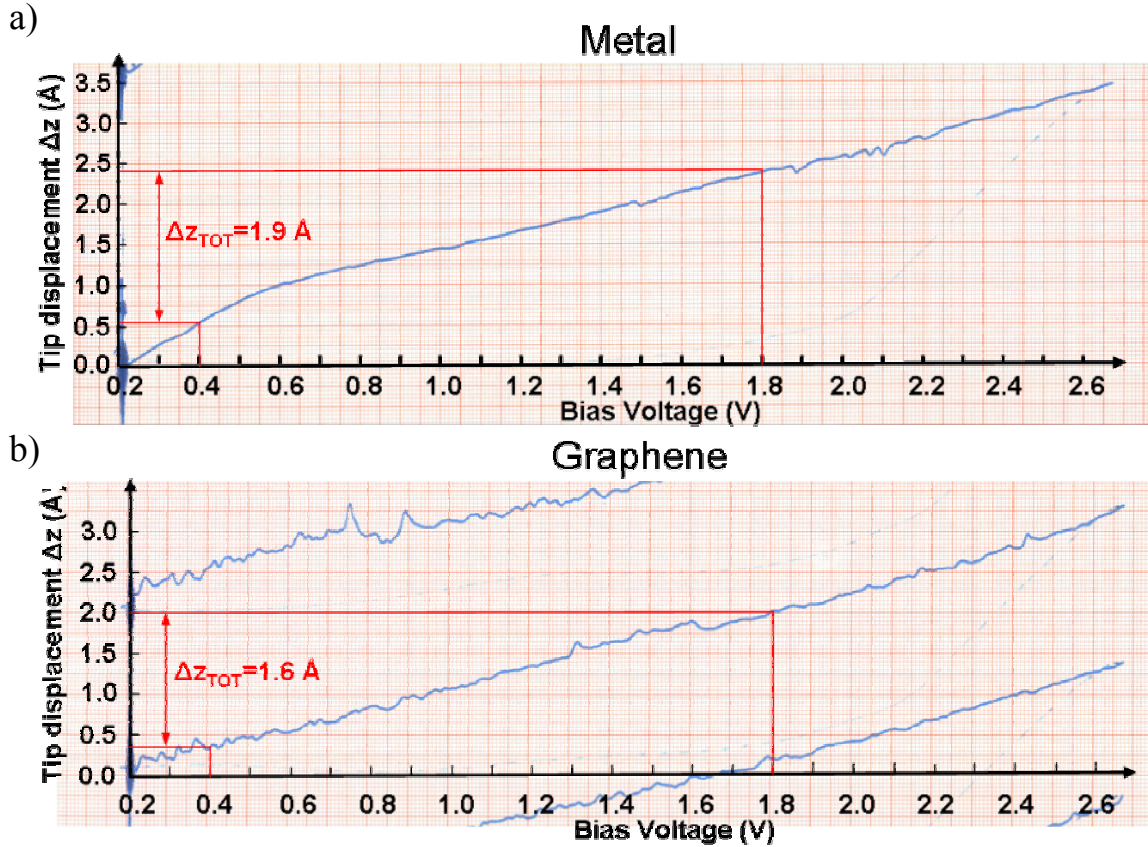


**Figure 3.32:** Vertical displacement  $\Delta z$  of the tip as function of the offset bias voltage at constant tunneling current (1 nA) on the metal (a) and the graphene (b) area.

The results are shown in figure 3.34. The decay length for the metal is constant over the entire region from -2.0 V to +2.0 V as already visible in figure 3.33 from the same slopes of the curves. The decay length for graphene, on the contrary, shows a strong voltage dependence. It displays two maxima at  $\sim -0.8$  V and  $\sim +0.6$  V, a minimum at 0 V where it is close to the value for the metal, and for large positive and negative voltages it seems to converge to the metal curve.

In chapter 1 it was mentioned that, in the 3D treatment of the tunneling effect also the wave vector component  $\vec{k}_{//}$  parallel to the tunneling junction (i.e. parallel to the sample surface) has to be considered. In this case the general expression for the tunneling current is characterized by an inverse decay length  $K$  given by:

$$K = \sqrt{\frac{2m\Phi}{\hbar^2} + k_{//}^2}$$

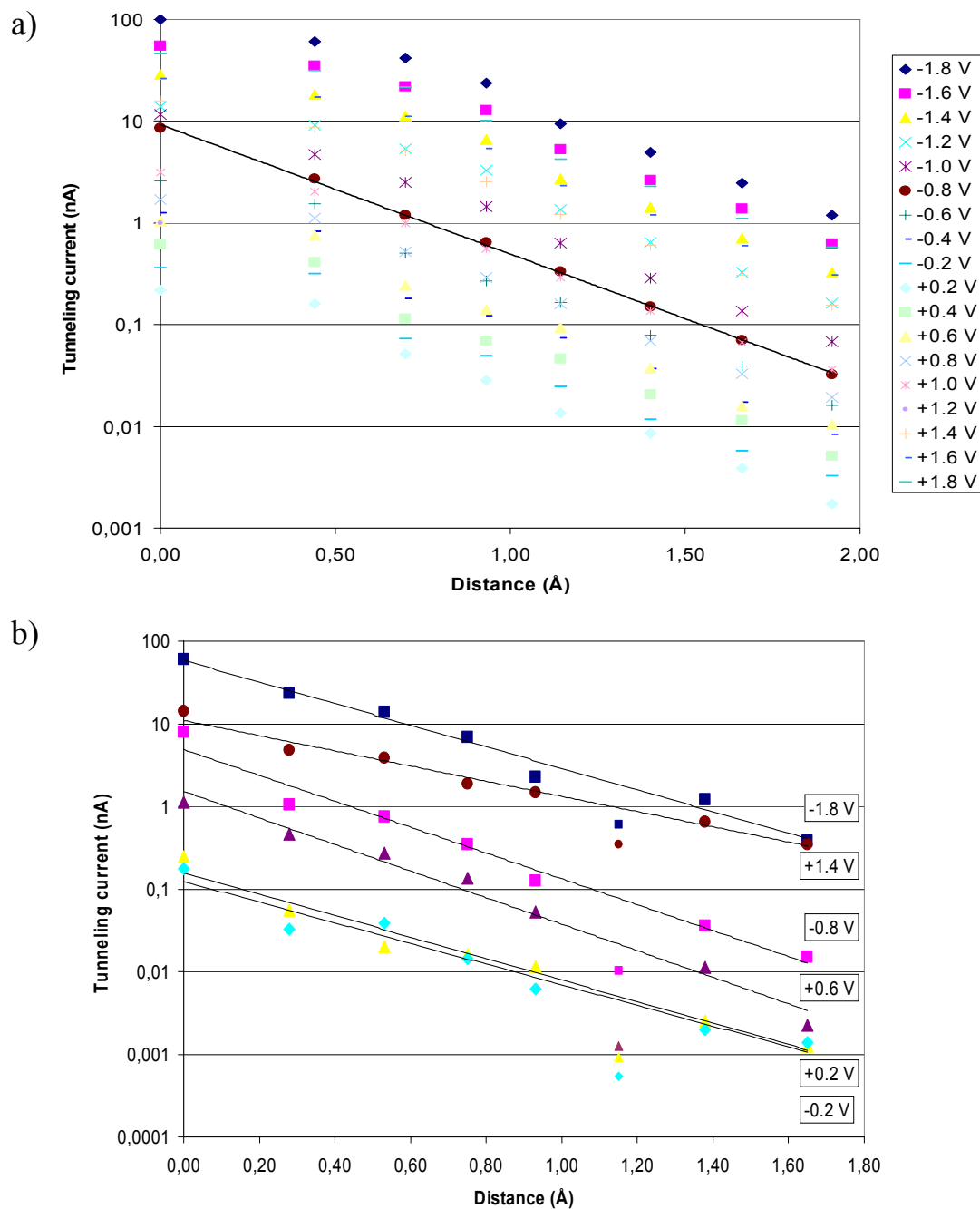


**Figure 3.33:** Logarithmic plot of the tunneling current  $I$  as function of the tip displacement  $\Delta z$ .  $\Delta z$  is obtained from a series of measurements like those shown in figure 3.32. A distance of  $\Delta z = 0 \text{ \AA}$  corresponds to the offset bias voltage of  $+0.4 \text{ V}$  and the other values represent the relative tip displacement as the offset voltage is increased in steps of  $+0.2 \text{ V}$  up to  $+1.8 \text{ V}$ . The tunneling current is obtained from the spectra shown in figure 3.31b and (c) for several voltage values between  $-1.8 \text{ V}$  and  $+1.8 \text{ V}$ . a) Results on the metal area. The linear decay of the tunneling current (logarithmic scale) with  $\Delta z$  is clearly visible and the lines corresponding to different voltages are parallel. b) Data from the graphene area. The data of a tip sample distance of  $1.15 \text{ \AA}$  appear to be affected by a systematic error and are not considered in the analysis. All other data display a linear decay.

This means that states with non-zero  $\vec{k}_{||}$  decay faster, i.e. they have a shorter decay length, in the tunneling barrier, so that states with  $\vec{k}_{||} = \vec{0}$  dominate the tunneling current. Only if there are no states with  $\vec{k}_{||} = \vec{0}$  tunneling from states with large  $\vec{k}_{||}$  can be observed.

In the case of ruthenium, the tunneling is dominated by states with  $\vec{k}_{||} = \vec{0}$  since  $\vec{k}_{||} = \vec{0}$  states are available over a wide range of voltages around  $E_F$ . A narrow partial band gap at  $\vec{k}_{||} = \vec{0}$  only develops at an energy of 1.6 eV above  $E_F$  [105]. It is therefore in agreement with expectations that the decay length over the bare Ru is constant over the voltage range investigated.

For graphene, on the contrary, the maxima represent states with large  $\vec{k}_{||}$  contributing to the tunneling. The band structure of an isolated graphene layer has no electronic states at  $\vec{k}_{||} = \vec{0}$  ( $\Gamma$  point) at energies between approximately  $-4$  V to  $+8$  V (figure 3.29). Directly at  $E_F$  graphene has a single state at the K point, i.e. at  $\vec{k}_{||} = 1.7 \text{ \AA}^{-1}$ . With increasing (positive or negative) energies away from  $E_F$   $\vec{k}_{||}$  decreases continuously. For isolated graphene figure 3.34 should accordingly show a curve with a maximum inverse decay length that continuously decreases to lower values towards higher and lower voltages.

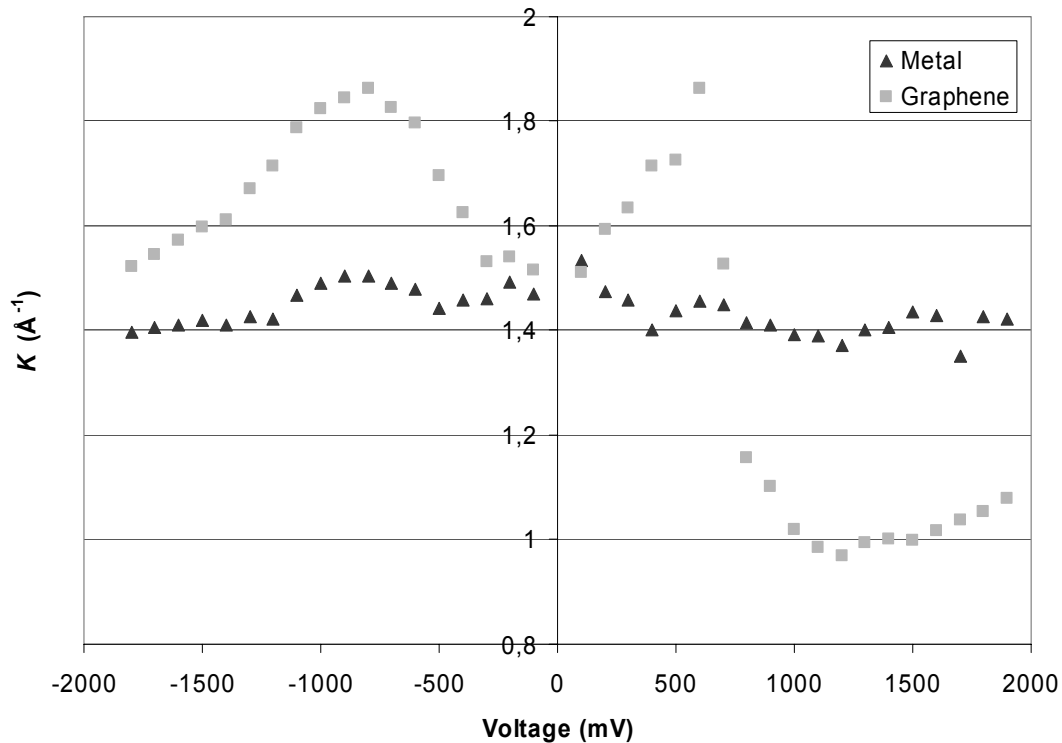


**Figure 3.34:** Decay lengths obtained from the slopes of the lines in figure 3.33 as function of the tunneling voltage. The decay length obtained on the metal area is constant while the data from graphene display two maxima.

Graphene/Ru(0001) is obviously different. The fact that a minimum is observed at  $V = 0$  V can be explained by the gap that was observed in STS. For tunneling voltages within the gap, there would therefore be no graphene states available (except possibly for some broadened states at the edges of the gap), so that the tunneling current would be mainly carried by electronic states of the underlying Ru substrate. This may explain that the decay length at 0 V becomes identical to that of the bare Ru. As the voltage is increased to the gap edges states with higher  $\bar{k}_{||}$  start to contribute to the current. The maxima in the inverse decay length curve accordingly occur close to the states observed in the tunneling spectra (figure 3.28). At more positive or negative voltages the inverse decay length again decreases because of the ordinary dispersion of the  $\pi/\pi^*$  bands of the isolated graphene (figure 3.29).

The minimum at approximately +1.2 V in the positive branch of the curve requires a different explanation. The strong decrease of  $K$  between +0.5 V and 1.2 V interestingly goes parallel with the evolution of the ring structure in the topographic data (figure 3.25). This correlation suggests a common reason. The changes of  $K$  in this energy range indicates that the electronic state displaying the ring structure is connected with a very low - and most likely even zero -  $\bar{k}_{||}$  value.

Figure 3.29 does not show such a state, but more elaborate calculations of bulk graphite found a surface state with a minimum at  $\Gamma$ , i.e. at  $\bar{k}_{||} = 0$ , and an energy of  $\sim +3$  eV [106].

Assuming that this state shifts down in energy by  $\sim 2$  eV upon bond formation between graphene and Ru (such a downshift of all graphene energies has in fact been observed by UPS [47]), tunneling into such a state may contribute here. It would explain the  $K$  minimum and would be correlated with the unique effects in the topographic data.

Despite the qualitative behavior of the measured decay length which is nicely explained in this way, it should be mentioned that the quantitative agreement is less good.

From the constant inverse decay length of ruthenium of  $1.4 \text{ \AA}^{-1}$ , a work function  $\Phi$  of 7.4 eV results, considerably higher than the value of 5.5 eV measured for bare ruthenium [47].

For graphene, using a work function of 4.5 eV obtained by Himpsel and coworkers [47] and the maximum value of  $1.8 \text{ \AA}^{-1}$  for the measured decay length, the obtained value for  $|\bar{k}_{||}|$  is  $1.43 \text{ \AA}^{-1}$ .  $|\bar{k}_{||}|$  at the K point of the surface Brillouin zone of graphene would be  $1.70 \text{ \AA}^{-1}$  [42]. On the other hand, it is not clear so far, if the edges of the band gap actually occur at the K point. Bond formation between graphene and Ru might lead to a more complicated electronic band structure at energies close to  $E_F$ .

Deviations might also be due to systematic errors occurring in the rather elaborate experimental process that was necessary for this analysis. Nevertheless the qualitative results, in particular the excellent agreement with the expected linear behavior in the I-z curves of figure 3.33 and the constant value obtained for the ruthenium decay length, give some credit to this analysis.

### 3.3 Gold deposition

The properties of graphene/Ru(0001) described in the previous paragraphs show that this system fulfils a series of important requirements for an ideal nanotemplate. Its preparation procedure, consisting in prolonged annealing of the sample in UHV, is relatively easy, the system displays a perfect order over large areas of the sample with a periodicity of 3 nm, it is stable in air and at high temperatures and it is chemically inert. For these reasons it may be suitable as nanotemplate to grow arrays of metal clusters. In particular, considering the peculiar size dependent catalytical properties of gold nanoparticles [15] it may give access to study the properties of gold deposited on this system. In the following paragraphs preliminary results will be shown.

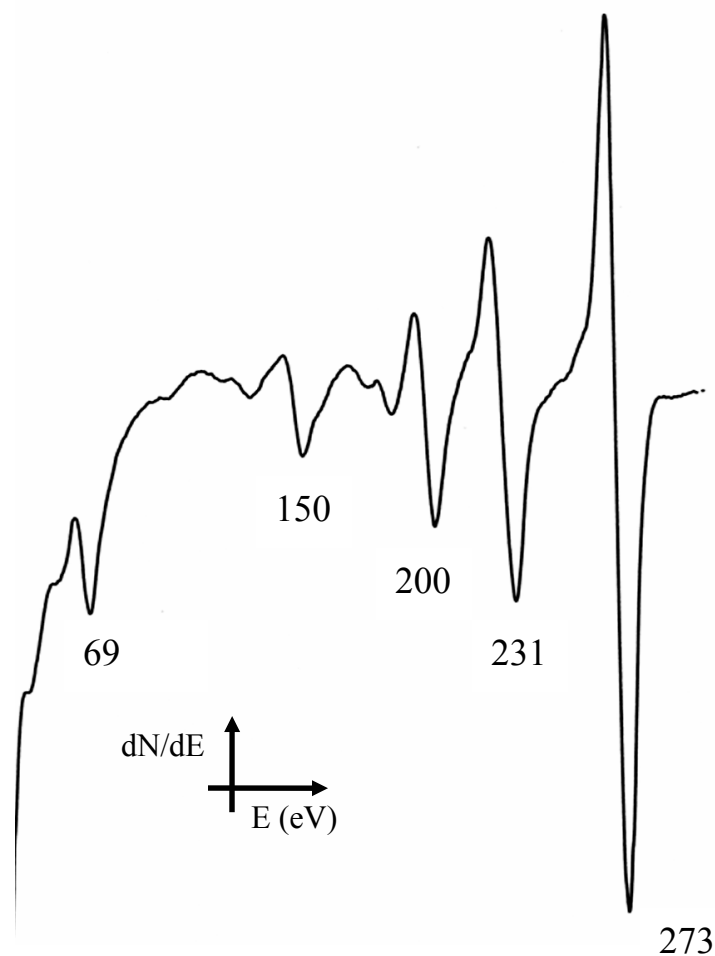


**Figure 3.35:** AES spectrum of Ru after 30 min of Au deposition at room temperature. The presence of gold on the surface is indicated by the peak at 69 eV due to the Au MNN transition (Primary electron energy: 2 keV).

### 3.3.1 Evaporator

In order to deposit gold on the Ru(0001) sample, a home-built resistively heated metal evaporator was employed. The gold source is placed in a tungsten spiral through which an electric current flows heating the source and causing sublimation of gold. At the same time, sublimation of tungsten is prevented because of the high sublimation temperature of this metal (a vapour pressure of  $10^{-7}$  Torr is achieved for gold at 1150 K while for tungsten it is necessary to reach 2520 K [107]). This system is placed into a stainless steel cylinder with an aperture of 15 mm, and the sample is positioned with the manipulator directly in front of the aperture at a distance of 140 mm from the gold source. The gold sublimated from the source can thus condense on the sample surface.

One of the main problems occurring during metal deposition is the presence of contaminants due to the hot filament or to the undesired heating of other components of the evaporator. For this reason the filament is operated with a current of 1.3 A and degassed for several minutes ( $10 \div 15$ ) without the sample in front of the aperture. During the initial phase of this procedure the background pressure increases by about  $5 \cdot 10^{-10}$  mbar and then decreases to its initial value. Typically, after the degassing procedure, the background pressure does not increase by more than  $1 \cdot 10^{-10}$  mbar during the gold deposition on the sample. Evaporation is thus performed in a background pressure of  $\sim 2 \cdot 10^{-10}$  mbar with a current through the filament of 1.0 A.

Figure 3.35 displays the AUGER spectrum of the surface after 30 min of gold deposition. The peak due to the presence of gold is clearly visible at 69 eV. It corresponds to a MNN transition involving the valence band of gold.

In order to calibrate the performance of the evaporator the gold coverage on the surface was determined by STM using large area images and averaging over several metal terraces. The results are shown in figure 3.36 where the sample coverage is plotted as function of the evaporation time together with the STM images. The images were taken at 300 K after deposition of gold at the same temperature. The image of figure 3.36d is taken after annealing the surface at 700 K after gold deposition at room temperature in order to remove the gold clusters formed on top of large gold islands and to obtain a homogeneous single layer of gold. The linear dependence of the gold coverage with the evaporation time is clearly visible, and one can estimate a flux of  $3 \cdot 10^{-3}$  ML/min. Such a low deposition rate was chosen in order to obtain better accuracy in experiments with low coverages of gold, in particular in the presence of graphene on the surface.

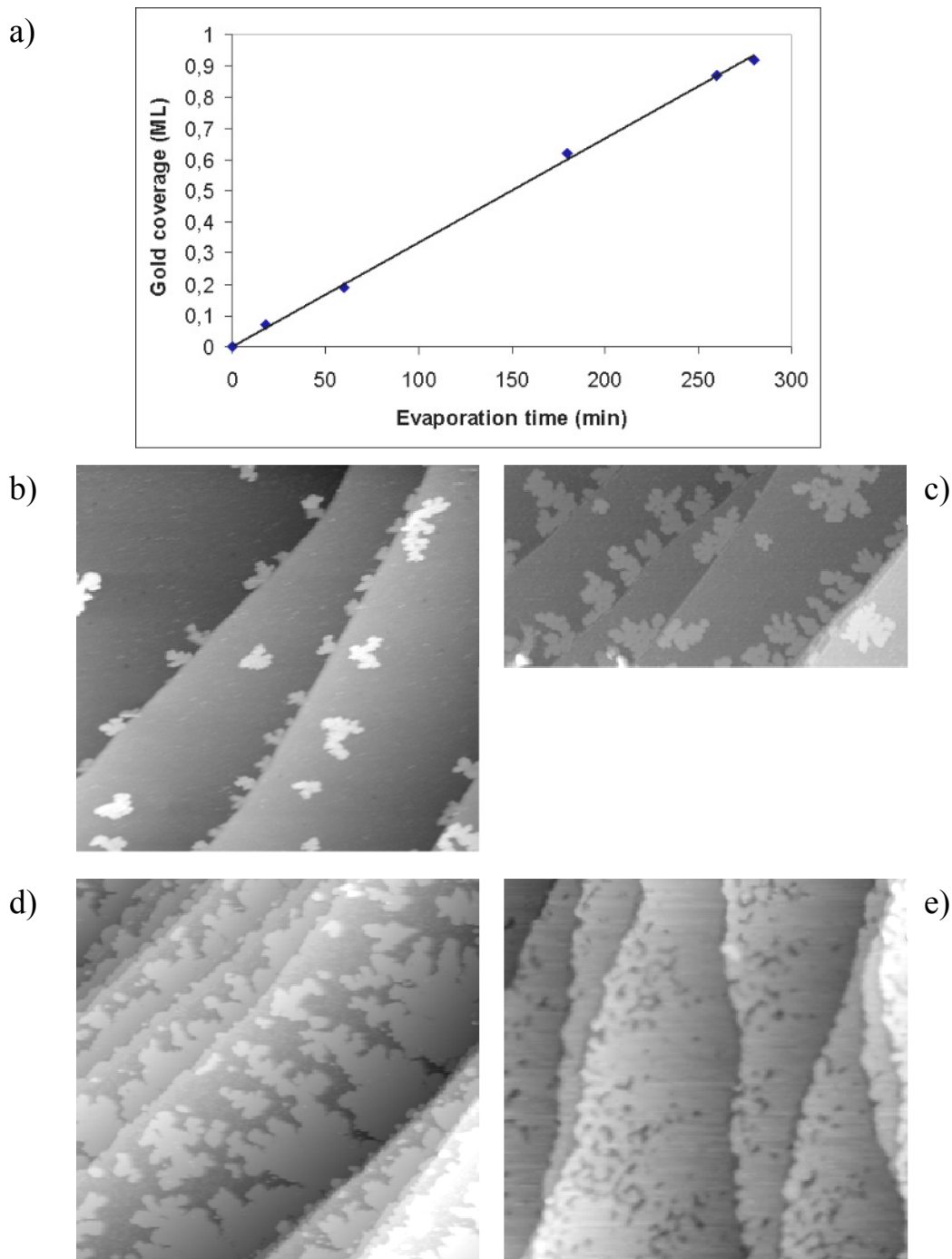


**Figure 3.36:** Calibration of the performance of the Au evaporator by STM. a) Au coverage as function of the evaporation time at room temperature. From the slope of the curve a flux of  $3 \cdot 10^{-3}$  ML/min is determined b ÷ e) Examples of STM images employed for the determination of the Au coverage. b) Image recorded after 12 min of Au evaporation:  $\Theta_{Au} = 0.07$  ML.  $I_t = 1$  nA,  $U = +0.5$  V,  $200$  nm  $\times$   $200$  nm. c) Image recorded after 60 min of Au evaporation:  $\Theta_{Au} = 0.19$  ML.  $I_t = 1$  nA,  $U = +0.5$  V,  $200$  nm  $\times$   $100$  nm. d) Image recorded after 180 min evaporation:  $\Theta_{Au} = 0.62$  ML.  $I_t = 1$  nA,  $U = +0.4$  V,  $200$  nm  $\times$   $200$  nm. e) Image taken after 280 min evaporation and an annealing to  $700$  K:  $\Theta_{Au} = 0.92$  ML.  $I_t = 1$  nA,  $U = +0.4$  V,  $200$  nm  $\times$   $200$  nm.

### 3.3.2 Gold on clean ruthenium

Figure 3.37 displays gold islands formed after gold deposition on the bare ruthenium surface at room temperature. The islands are characterized by the typical dendritic fractal shape [108] explained by the diffusion-limited aggregation (DLA) model [109]. The individual gold atoms are highly mobile on the bare ruthenium surface at room temperature and, once adsorbed on the metal surface, they perform random walks. When they reach the edges of a gold cluster, they are trapped and their diffusion is kinetically hindered. The limited diffusion of gold atoms once bound to the edges of islands at room temperature gives rise to the dendritic shape. This was confirmed by Hwang and co-workers who showed that annealing the sample to 500 K after gold deposition at room temperature results in the formation of islands with compact form [110]. At 500 K the mobility of the gold atoms at the clusters edges is enhanced and the clusters relax to energetically favourable shapes.

The STM image of figure 3.37 displays a gold island grown around a screw dislocation of the ruthenium surface and further islands growing at step edges of the surface. This property was observed before [111], and it is quite common that defect sites on metal surfaces act as nucleation sites for clusters growth.

A line scan analysis of the STM image shows that the gold islands have an apparent height of  $\sim 2.5$  Å above the ruthenium surface, and are thus higher than the Ru monoatomic steps ( $=2.14$  Å).

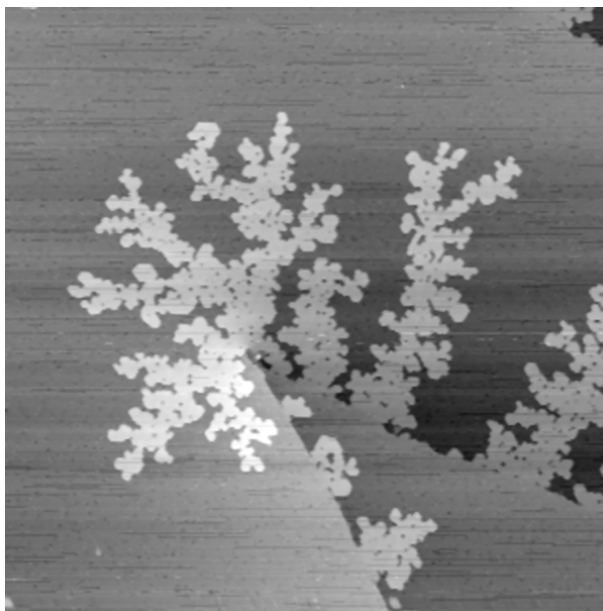


**Figure 3.37:** STM image recorded after 30 min of Au deposition on the clean Ru surface. The Au islands display the typical dendritic shape due to the fractal growth mechanism. The island in the centre of the image grows around a screw dislocation of the ruthenium while the other islands grow at the lower step edges of the surface.  $I_t = 3$  nA,  $U = +0.5$  V, 50 nm x 50 nm.

### 3.3.3 Gold on the surface partially covered with graphene

Figure 3.38a displays an STM image taken after 45 min deposition of gold at room temperature on the surface partially covered with graphene. The image displays six metal terraces partially covered by graphene areas recognizable by the characteristic moiré periodicity. The light-grey features with irregular shapes are gold islands. The coverage of gold on the bare ruthenium areas is about 0.5 ML, while on the graphene areas it is 0.08 ML. Gold obviously nucleates preferably on the ruthenium areas where the bonding to the substrate is stronger than on graphene and the total energy is minimized. Furthermore, there is a high concentration of gold islands on the bare ruthenium at the edges of the graphene layers. The graphene edges can act as nucleation centres for the gold islands in a similar way as the dislocation sites or the lower step edges of bare ruthenium [111]: gold particles deposited on the surface diffuse and get trapped at the edges of the graphene layer where the islands formation then starts. It can, however, not be ruled out that this phenomenon is an effect of the scanning tip of the STM. By scanning, the weakly bounded islands on graphene could be moved by the tip to the bare ruthenium areas where they bind more strongly and are not affected by the microscope tip any more. It would be desirable to systematically investigate this effect performing STM measurements at various tip-sample distances.

Another interesting result is the shape of the gold islands: on graphene they exhibit a more compact shape than on the metal areas, and the fractal growth is not observed (figure 3.38b). This indicates that the diffusion of gold atoms at the edges of the islands grown on graphene is not limited as on the ruthenium areas so that the islands can assume compact shapes even at room temperature.

Figure 3.38b shows a gold island grown on graphene in detail. Interestingly it displays the same moiré modulation as the graphene layer with a modulation amplitude of about 0.5 Å. The apparent height of the island above the graphene layer thus oscillates between 3.2 and 3.7 Å

Using the height difference between gold islands grown on the bare Ru and islands grown on graphene one can estimate the height of the graphene layer above the metal. This estimate is based on the assumption that the local density of states of the Au islands is the same independently on the substrate on which they have grown. A height oscillating between 1.8 and 2.3 Å is obtained which is in agreement with the results of paragraph 3.2.3 I.

Unfortunately, gold deposited at room temperature on graphene does not show the formation of ordered arrays of clusters with one cluster per moiré unit cell, but shows, on the contrary, the tendency to form large compact islands.

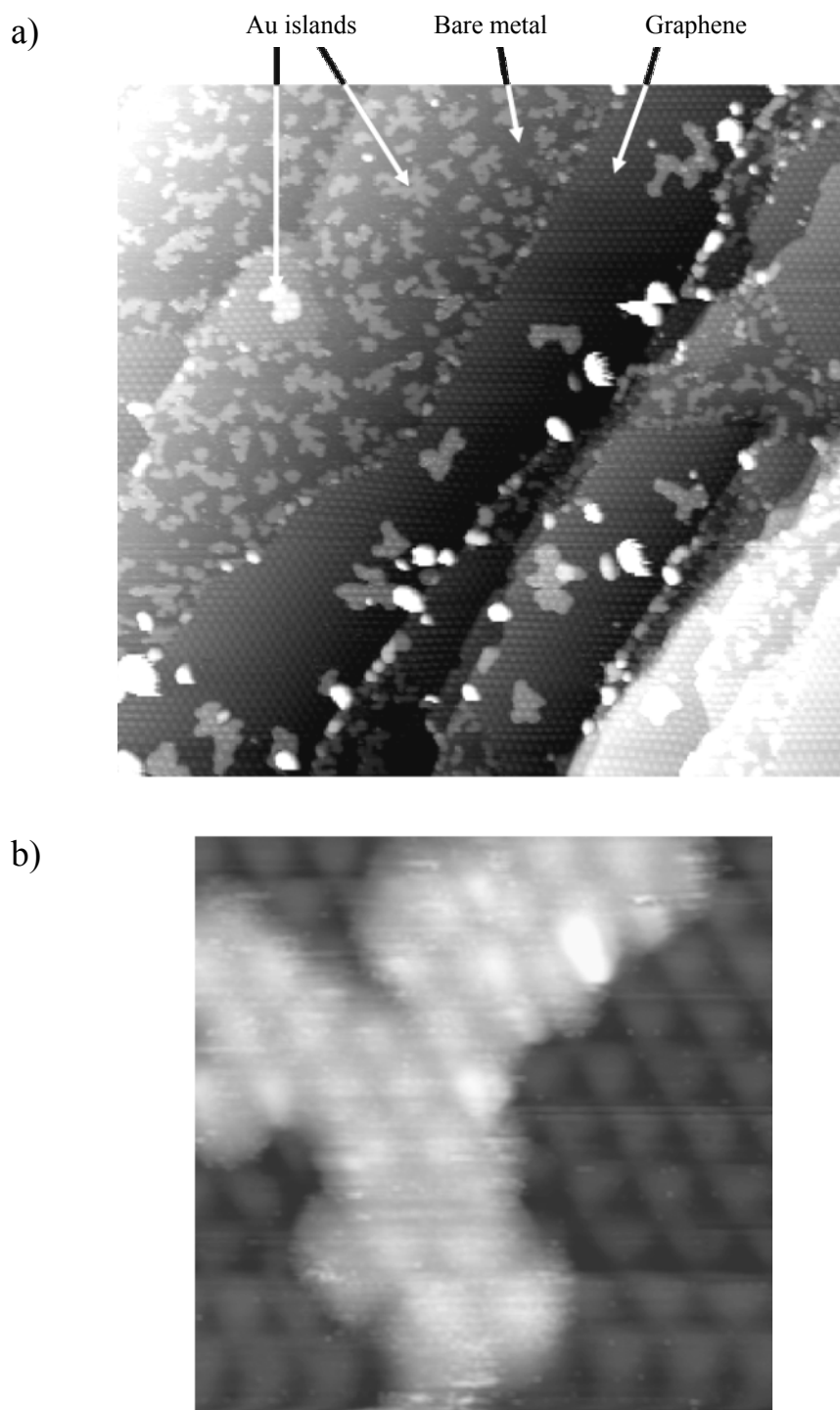


**Figure 3.38:** STM images recorded after 45 min of Au deposition on the surface partially covered with graphene. a) The image shows six metal terraces partially covered with graphene. The gold coverage on the metal areas is much higher than on graphene and several islands appear at the edges of the graphene layer.  $I_t = 1$  nA,  $U = -0.7$  V, 200 nm x 200 nm. b) Au island grown on graphene. The island displays the same height modulation as the graphene moiré structure. The compact shape is different from the dendritic shape of the islands grown on the bare metal.  $I_t = 1$  nA,  $U = -0.7$  V, 20 nm x 20 nm.

Goriachko and co-workers deposited gold on the (12x12) structure formed by hexagonal boron nitride deposited on the Ru(0001) surface [71]. After annealing the sample to 900 K they observed the formation of well defined round nanoparticles of gold randomly distributed over the surface. This behaviour is completely different from the behaviour of iridium deposited on the (11x11) structure formed by graphene on the Ir(111) surface [68]. In this work the formation of regular arrays of Ir clusters was observed with tunable sizes that were stable up to 500 K. However, in the case of Ir, the surface could not be completely covered with the graphene layer and the regular arrays of Ir clusters were then only observed on the graphene islands.

These preliminary results show that Au can be deposited with the newly built source in a clean and controlled way. However, the islands formed on the graphene are too large which is most likely caused by a too high mobility of the Au atoms on the graphene at room temperature. In the future the temperature will therefore be lowered and the deposition of other metals will be tried. From its homogeneity the Ru(0001)/graphene system has great potential for engineering 2D arrays of nanoparticles.





## Chapter 4

### CO poisoning of O/Rh(111)

One of the key issues in the study of oxygen adsorption on transition metal surfaces is the saturation coverage. The saturation coverage is the main calibration point for surface analytical techniques, and it enters kinetic models of catalytic reactions. It is further a measure of the reactivity of a given metal.

Recently, there has been a debate about the oxygen saturation coverage on Rh(111), with several groups suggesting 0.5 ML and a STM group measuring only a (2x2) structure compatible with a maximum coverage of 0.25 ML. It will be shown here that the source of these discrepancies is the presence of CO molecules poisoning the rhodium surface and modifying its reactivity.

#### 4.1 Oxygen saturation coverage of Rh(111): 0.25 or 0.5 ML?

There has been a fierce discussion in the recent literature about the interpretation of the (2x2) low energy electron diffraction (LEED) pattern observed during oxygen exposure on Rh(111) [112-114]. Most authors assume that the (2x2) pattern indicates two different phases of adsorbed O atoms, a (2x2)O phase at  $\Theta(\text{O}) = 0.25$  ML and a (2x1)O phase at

$\Theta(\text{O}) = 0.5$  ML. Because the (2x1)O structure forms three rotational domains that lead to the same diffraction spots as the (2x2)O structure, the two structures can not be distinguished by inspection of the LEED pattern, and more elaborate arguments were used. In contrast to this interpretation, scanning tunneling microscopy (STM) data obtained by Xu and Ng showed only one phase, a (2x2) structure [112, 114].

The debate has some significance for the question about systematic trends in the reactivities of transition metals with oxygen. The hexagonally closed-packed surfaces of Rh and of Ru and Pd, the left and right neighbors of Rh in the periodic table, display remarkable similarities. On all three metals oxygen atoms adsorb on three-fold hollow sites. For Ru(0001) and Pd(111) it is well established that the (2x2)O structures, with  $\Theta(\text{O}) = 0.25$ , are most stable, but that there are further, thermodynamically stable structures at higher coverages, among them (2x1)O structures at  $\Theta(\text{O}) = 0.5$  (oxide-like phases [115] are not considered here). Moderate O<sub>2</sub> doses at 300 K only lead to the (2x2)O phase on Pd(111) [116] and to the (2x1)O phase on Ru(0001) [39] [117], but these limits are caused by kinetic restrictions. The phases with higher coverages can, in fact, be obtained by dosing at higher temperatures, with stronger oxidants than O<sub>2</sub>, or by coadsorption of other gases [30, 118-122]. Rh(111) fits into this scheme in so far as a (2x2)O structure exists - this fact has not been doubted in the mentioned dispute - and a (1x1)O phase could be prepared with atomic oxygen and NO<sub>2</sub> [123, 124]. The question is therefore if a (2x1)O structure can form by O<sub>2</sub> adsorption alone, like on the more reactive Ru, or if its formation is kinetically restricted as on Pd.

The following arguments speak for two oxygen structures with a (2x2) diffraction pattern on Rh(111), i.e., a (2x2) structure with  $\Theta(\text{O}) = 0.25$  plus a (2x1) structure with  $\Theta(\text{O}) = 0.50$ . During O<sub>2</sub> dosing the half order spots show two intensity maxima as a function of exposure, one at about 1 L (indicating the (2x2)O structure), the second at saturation at about 10 L (indicating the (2x1)O structure) [125]. The LEED I(V) curves, measured at the two maxima, display differences [125, 126] that are small but distinct enough that one group of authors concluded that two different structures must exist [125]. After a certain dosing procedure elongated half order spots were observed close to saturation, which can be explained by narrow domains of the (2x1)O structure, supporting the interpretation that at saturation a (2x1) structure is present [127]. Also most of the recent x-ray photoelectron spectroscopy work agrees on an oxygen saturation coverage of 0.5 at 300 K [128-130]. At saturation and at half saturation different Rh core level shifts were observed, again indicating two different structures [131]. Finally, DFT calculations predict that both phases would be stable [132]. On the other hand, the quoted STM data [112, 114], which may appear the most direct experimental evidence in this matter, clearly showed only a (2x2) structure; no transformation into the (2x1)O phase at larger oxygen exposures was observed. STM and TPD data presented here can resolve this discrepancy and show that the presence of contaminants modifies the reactivity of the surface.

## 4.2 The Rh(111) surface and the sample preparation procedure

Rhodium is a transition metal of the platinum group with atomic number 45 and electronic configuration  $[\text{Kr}]4d^85s^1$ . Its crystal structure is face centered cubic (fcc) with lattice constant 3.803 Å. The (111) surface, employed in this study, is described by a triangular lattice with lattice constant  $a = 2.689$  Å. A model of the surface with the four high symmetry adsorption sites is shown in figure 4.1.

The sample was cleaned following the standard UHV procedures consisting of repeated cycles of Ar ion sputtering ( $3 \cdot 10^{-5}$  mbar Ar, 1.5 keV, 5  $\mu\text{A}$ , 15 min), annealing to 1300 K, oxidation at elevated temperature ( $2 \times 10^{-7}$  mbar  $\text{O}_2$ , 700 K), and flash annealing to 1100 K. The oxidation, performed for 1-2 hours, served to remove the residual carbon from the surface, the final flash was quick and to a lower temperature than the previous annealing temperature to prevent carbon segregation from the bulk of the crystal. Sample cleanliness and structural order were checked with LEED, AES, and STM.

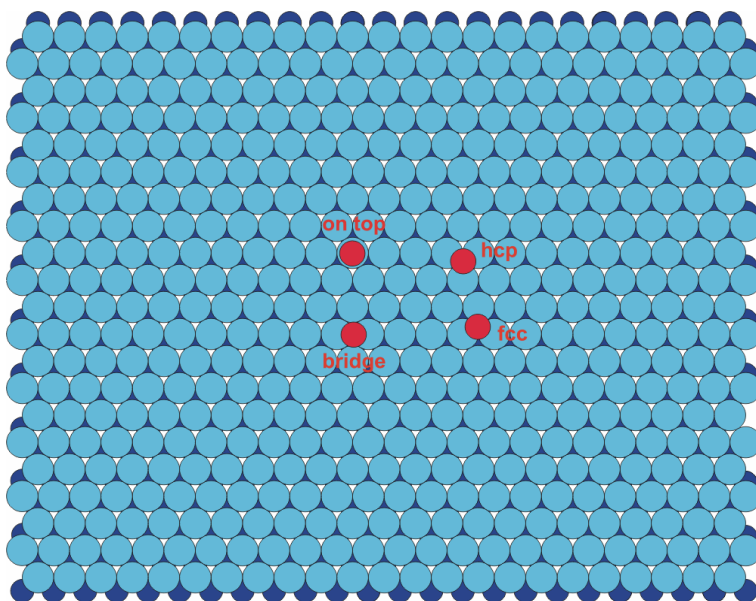


**Figure 4.1:** Model of the Rh(111) surface with the 4 high symmetry adsorption sites: “on top” directly above a metal atom, “bridge” between two atoms, threefold “fcc”, the hollow site without a metal atom in the second layer, threefold “hcp” with a metal atom directly below in the second layer.

### 4.3 (2x1) and (2x2) oxygen structures

Figure 4.2 shows STM data of the Rh(111) surface, recorded at 300 K after dosing 30 L of O<sub>2</sub> at a sample temperature slightly above 300 K. According to the literature this exposure corresponds to oxygen saturation at 300 K. LEED of this surface showed a (2x2) diffraction pattern with very sharp spots, without spot elongations. The two STM frames are recorded on the same area around an atomic step (the irregular, diagonal line) and the horizontal shift of the step between the two frames is caused by thermal drift. The terraces are completely covered by a streaky structure that forms large domains, which are rotated by approximately 120° with respect to each other. Deviations from precise 120° angles can be explained by drift. The periodicity of the row structure is  $(4.5 \pm 0.5) \text{ \AA}$  perpendicular to the rows (the error is caused by drift). The distance between two close-packed atomic rows of the Rh(111) surface, measured perpendicularly to the rows, is  $(\sqrt{3}/2)a = 2.3 \text{ \AA}$ , i.e., the experimental value approximately corresponds to two times this distance. The large domain on the left terrace of figure 4.2a and the identically oriented domain in the center of figure b also display a fine structure along the rows. The periodicity is  $(3.1 \pm 0.3) \text{ \AA}$ , approximately equal to the lattice constant of Rh(111) of 2.7 Å. It is concluded that figure 4.2 shows a (2x1)O structure with an oxygen coverage of 0.5 ML. The model in figure 4.2c displays a (2x1) structure of O atoms on the Rh(111) surface and explains the formation of the three rotational domains visible in a and b.

Figure 4.3 shows translational boundaries, where two domains are displaced perpendicularly to the rows as indicated in the model of figure c.

The data thus show all possible types of domains for a (2x1) structure on a (111) surface, i.e., all three rotational domains and the two translational domains.

The sharp LEED pattern and the absence of spot distortions is in agreement with the large and evenly shaped domains. Because the (2x1)O structure is symmetric with respect to occupied and empty O adsorption sites the bright or dark rows in the STM images can not be attributed to oxygen atoms, which, of course, does not affect the identification of the structure.

Both figures show massive fluctuations of the (2x1) domains. For example, in figure 4.2 the domain to the right of the step in (a), which has the rows oriented perpendicularly to the step, has increased in (b), in figure 4.3 the antiphase boundary appears irregular and changes its position between the two frames. The domain boundaries fluctuate on a time scale comparable to the time period of the individual scan lines (in this case 0.12 s) as follows from the parallel orientation of many of the dislocation features to the direction of the scanning lines in figure 4.3. Obviously, the oxygen layer is very mobile at 300 K, even at the saturation coverage of 0.5 ML.

As mentioned, it is assumed that O<sub>2</sub> exposures of approximately 1 L lead to the (2x2)O structure with a coverage  $\Theta(\text{O}) = 0.25 \text{ ML}$ . In the STM measurements at 300 K no overlayer structure is resolved after such a dose. However, by lowering the temperature, an ordered structure becomes visible. Figure 4.4 shows the surface after dosing 1.5 L of O<sub>2</sub> at 320 K and cooling to 60 K where the STM measurement is then performed.

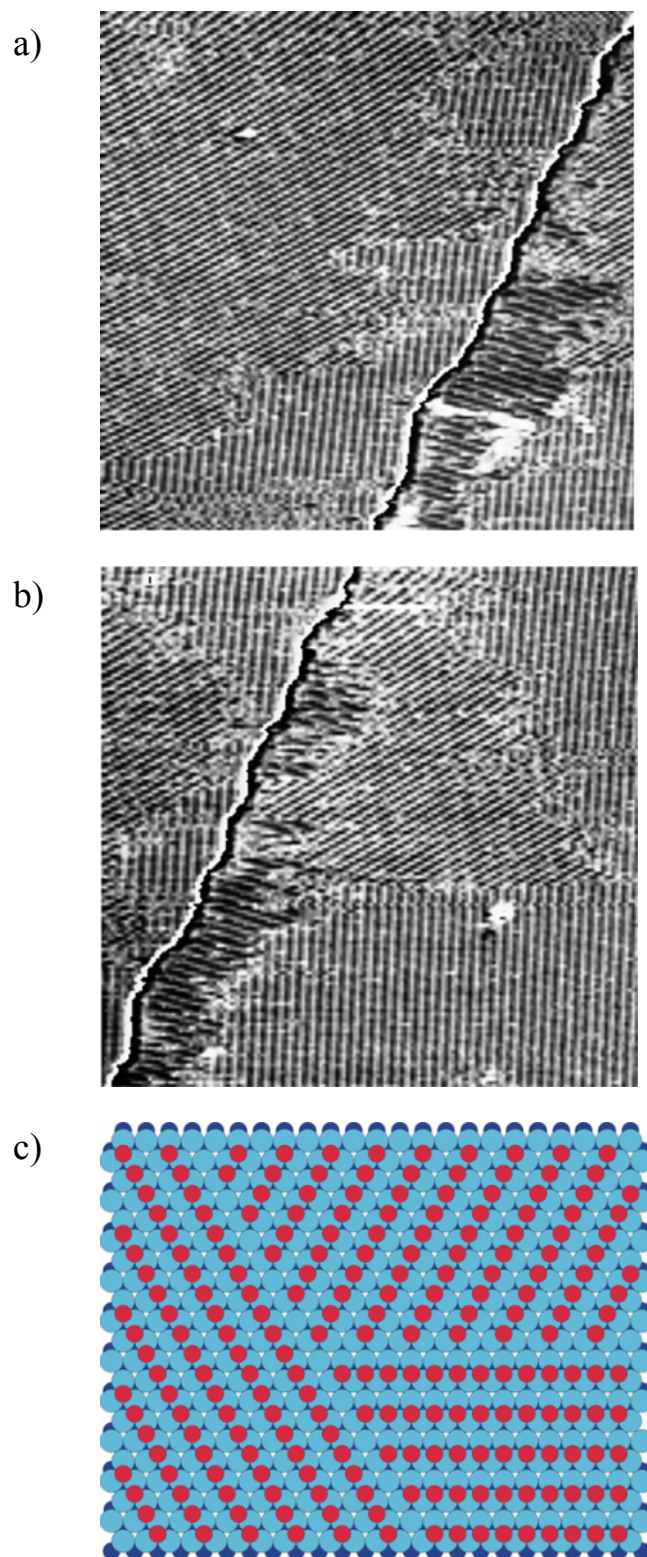


**Figure 4.2:** a) and b) STM images of the surface after dosing 30 L of  $O_2$  at 300 K and recorded on roughly the same area. The images display a streaky structure forming three different rotational domains. 26 nm x 23 nm,  $U = +0.21$  V,  $I_t = 1$  nA. c) Model showing the formation of the three different rotational domains formed by a (2x1) structure on the Rh(111) surface.

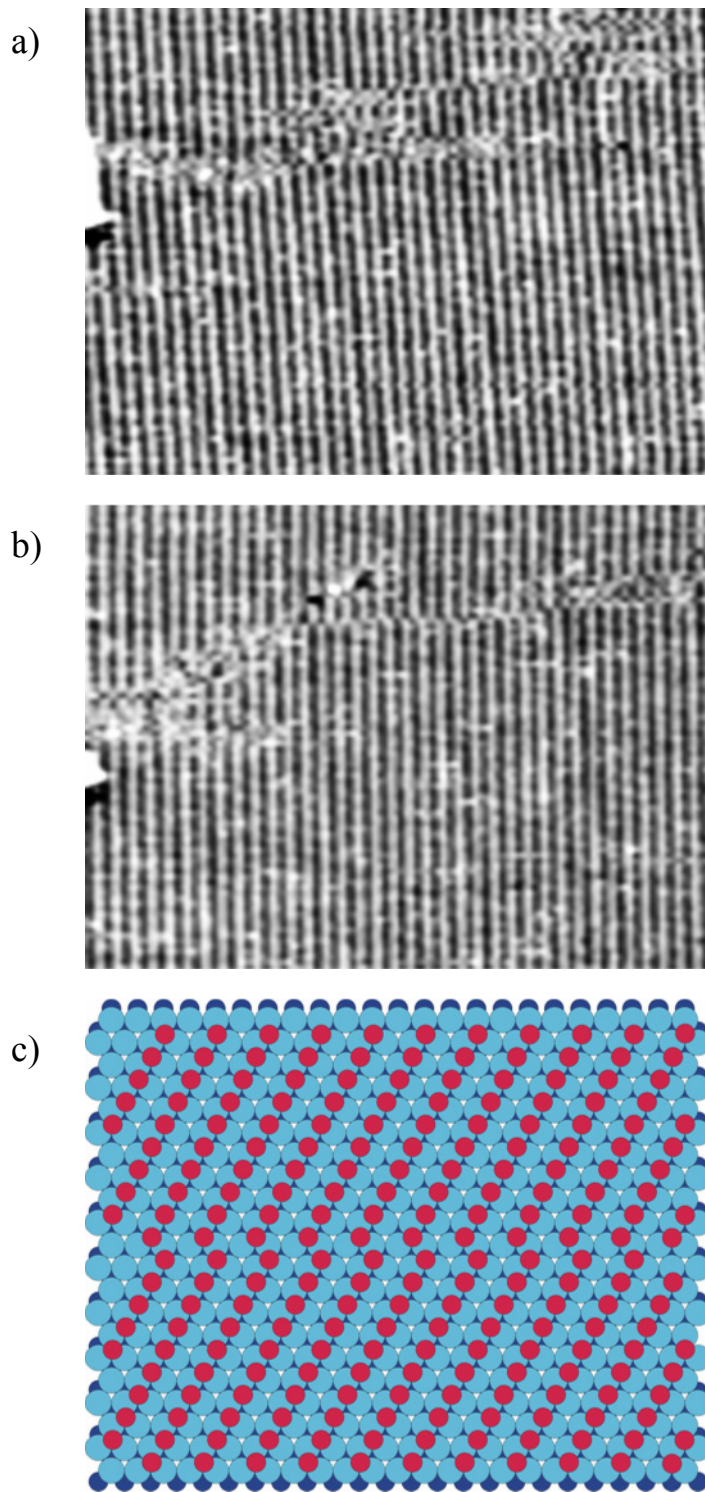


**Figure 4.3:** a) and b) STM images of the surface after dosing 30 L of  $O_2$  at 300 K and recorded on the same area. The streaky structure forms two translational domains. The domain boundary fluctuates revealing the high mobility of the oxygen atoms on the surface. 19 nm x 13 nm,  $U = +0.21$  V,  $I_t = 1$  nA. c) Model showing the formation of two different translational domains of a (2x1) structure on the Rh(111) surface.

The bright atomic features form islands with a hexagonal structure. The lattice constant of  $(5.0 \pm 0.5) \text{ \AA} \times (5.0 \pm 0.5) \text{ \AA}$  agrees with twice the lattice constant ( $2.7 \text{ \AA}$ ) of the Rh(111) surface. The STM data thus also confirm the existence of the  $(2 \times 2)\text{O}$  structure. The O atoms appear bright in figure 4.4, in contrast to the usual dark imaging of adsorbed oxygen [133], but this can be explained by a chemically modified tip, most likely by oxygen from the dosing.

That it is necessary to lower the temperature to resolve the  $(2 \times 2)\text{O}$  structure has actually been expected. LEED and He scattering experiments revealed a reversible order-disorder phase transition of the  $(2 \times 2)\text{O}$  phase on Rh(111) at 280 K [134]. Obviously, the disordered state at 300 K is connected with such a high mobility of the O atoms that resolution of the disordered O structure is prevented. This explanation is in agreement with the strong domain boundary fluctuations at  $\Theta(\text{O}) = 0.5 \text{ ML}$ , where the O atoms are only immobilized in the inner regions of the  $(2 \times 1)$  domains.

I have also performed experiments on the reaction of the adsorbed oxygen with  $\text{H}_2$ . At 300 K the  $(2 \times 1)\text{O}$  phase disappears very quickly in an  $\text{H}_2$  atmosphere ( $p(\text{H}_2) = 2 \cdot 10^{-7} \text{ mbar}$ ), in agreement with previous findings of a reaction onset at 275 K [135].

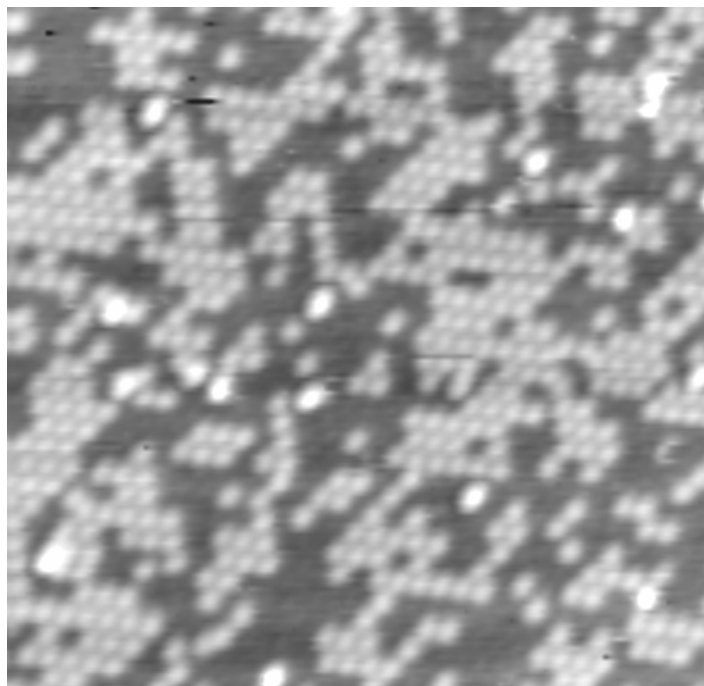


**Figure 4.4:** STM image recorded at 60 K after dosing 1.5 L  $\text{O}_2$  at 320 K. Islands with the  $(2 \times 2)$  structure are resolved. 19 nm x 19 nm,  $U = +0.86 \text{ V}$ ,  $I_t = 1 \text{ nA}$ .

#### 4.4 Oxygen adsorption in the presence of contaminants

Under slightly worse vacuum conditions (i.e. a background pressure decreasing slightly more slowly after the preparation and dosing steps) the LEED pattern after saturation of the surface with oxygen shows broadened half order spots. Figure 4.5 shows an STM image from such a surface, recorded at 300 K after adsorption of 30 L of O<sub>2</sub> at 320 K. Although the surface is thus prepared in the same way as in the experiment of figure 4.2 and figure 4.3, the STM shows a hexagonal structure instead of the stripe structure of the (2x1)O phase. The lattice constant is  $(5.8 \pm 0.6) \text{ \AA} \times (5.8 \pm 0.6) \text{ \AA}$ , close to twice the lattice constant of the Rh(111) surface. Four translational domains occur as indicated by the four different lattices superimposed on the atomic features. The model in figure 4.6 displays the four translational domains that are possible for a (2x2) structure on the Rh(111) surface.

The data thus clearly show a (2x2) structure, in agreement with the LEED pattern. The surface is completely covered with this ordered phase, except for the bright defects at the domain boundaries which have a coverage of 0.5% (figure 4.5). The average diameters of the domains of only 40 to 50 Å can explain the broadened half order LEED spots.

Higher oxygen doses of up to 200 L, and also recording STM images for long times (1-2 h) in an oxygen background pressure of  $5 \times 10^{-9}$  mbar, do not modify this structure. Under these conditions the (2x1)O phase can not be prepared. These findings are quite similar to those reported by Xu and Ng [112]. The (2x2) structure observed at 300 K in this previous STM study did also not transform into a (2x1) structure by increasing the O<sub>2</sub> exposure to 27 L or by scanning in an O<sub>2</sub> atmosphere. This result led to the mentioned debate about the (2x2) LEED pattern on Rh(111). The data from the quoted paper also show similar bright defect features at the domain boundaries. These similarities suggest that the surface state of the Xu and Ng investigation was the same as that of figure 4.5.

This (2x2) overlayer behaves quite differently than the two oxygen structures investigated above. The data show an almost static structure at 300 K, in contrast to the extremely mobile oxygen layer at  $\Theta(\text{O}) = 0.25 \text{ ML}$  and to the still considerably mobile domain boundaries of the (2x1)O structure. Furthermore, in an H<sub>2</sub> pressure of  $5 \times 10^{-7}$  mbar this (2x2) structure remains unchanged in LEED and STM at 300 K, in disagreement with the observed high reactivity of oxygen with H<sub>2</sub>. It must be concluded that this overlayer is different from the (2x2)O structure.

For further analysis thermal desorption spectroscopy (TDS) experiments of this surface phase were performed, monitoring the masses of hydrogen (2), oxygen (16, 32), water (18), carbon monoxide (28), carbon dioxide (44) and argon (40). It turns out that for O<sub>2</sub> exposures between 10 and 200 L no desorption of hydrogen, water, argon and, surprisingly, not even oxygen was observed. On the contrary, there are strong desorption peaks of masses 28 and 44 at about 520 K and shoulders at 500 K (figure 4.7), indicating CO and CO<sub>2</sub> desorption. The CO spectrum also shows a slow increase towards higher temperatures. Quite clearly, the surface is contaminated with some carbon species.

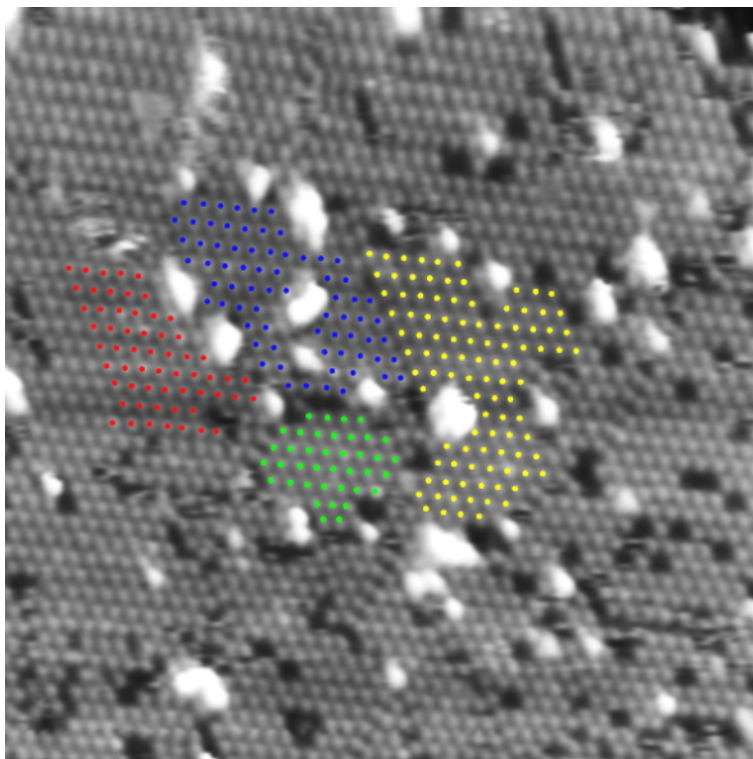


**Figure 4.5:** STM image recorded at 300 K after dosing 30 L of  $O_2$  at 320 K. The image displays a  $(2 \times 2)$  structure as revealed by the four translational domains indicated by the colored lattices. 25 nm x 25 nm,  $U = +0.3$  V,  $I_t = 3$  nA.

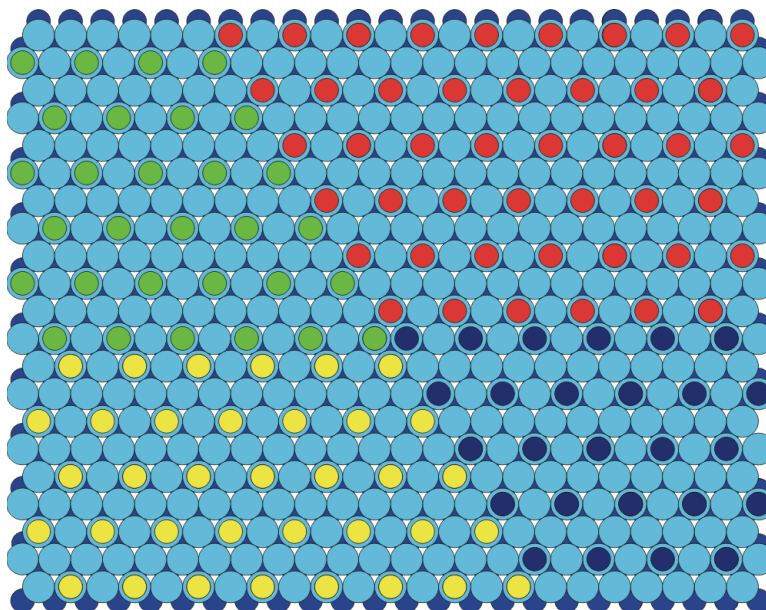


**Figure 4.6:** Model showing the formation of the four different translational domains of a  $(2 \times 2)$  structure on the Rh(111) surface.

What is the nature of this species? Elemental carbon, segregated from the bulk, can be ruled out because the segregation temperature of 950 K determined by XPS studies [136] is much higher than the observed CO/CO<sub>2</sub> desorption peaks at 520 K. Carbon segregation and reaction with residual surface oxygen could explain the slow CO increase in the TDS at higher temperatures and the absence of any O<sub>2</sub> desorption (expected at ~970 K [137]). However, these conditions are not related to the formation of the (2x2) structure at 300 K. Adsorbed CO at 300 K and in UHV would form a ( $\sqrt{3}\times\sqrt{3}$ )R30° structure or a "split spot" structure [137] characterized by a LEED pattern with double diffraction spots that was never observed in the experiments. In addition, there are two CO structures on Rh(111) with (2x2) symmetry, one with  $\Theta(\text{CO}) = 0.25$  ML and one with 0.75 ML, but they occur under completely different conditions than here. The (2x2)-CO structure corresponding to a coverage of 0.25 ML is observed only at low temperatures ( $T < 120$  K) and is destroyed within few seconds by the electron beam of the LEED [138]. The (2x2)-3CO structure, corresponding to 0.75 ML coverage, was observed only in a permanent CO pressure of  $10^{-5}$  Torr [137]. A pure CO structure is therefore ruled out.

Experimental observations about the adsorption of CO<sub>2</sub> at room temperature on Rh(111) indicate that the molecule dissociates after chemisorption, and no ordered structures of pure CO<sub>2</sub> have been observed. HREEL spectra taken after exposure of the surface to CO<sub>2</sub> are identical to the spectra taken after CO adsorption [139]. At the same time, LEED experiments showed the formation of the same ordered structures exposing the surface either to CO or to CO<sub>2</sub> with the only difference that, using CO<sub>2</sub>, higher exposures were needed [137]. For these reasons it can be also ruled out that the observed (2x2) structure is a pure CO<sub>2</sub> structure.

The only reasonable explanation left is CO in a mixed structure with oxygen. The coadsorbed phases of oxygen and CO were studied by LEED [113], TPD [113] and core level photoemission spectroscopy [140]. These studies revealed the presence of three different phases with (2x2) periodicity which were referred to as (2x2)-(O+CO), (2x2)-(O+2CO) and (2x2)-(2O+CO) according to the type and number of species in the unit cell.

The (2x2)-(O+2CO) has two CO molecules per unit cell, one sitting on-top, the other in the hcp sites, and an oxygen atom in the fcc sites. This structure was obtained by exposing the pure (2x2)-O structure to a large amount of CO (20-3000 L) at 250 K, but it was found to be stable only at low temperatures. At 300 K the CO molecules would desorb or react with O.

The (2x2)-(2O+CO) structure is formed by 2 oxygen atoms per unit cell, one sitting in fcc sites, the other in hcp sites, and a CO molecule on an on-top site. This structure was prepared by exposing the (2x1)-O structure to 10 L of CO at 160 K and flashing the surface to 200 K to enhance the surface ordering. Also this structure was only found to be stable at low temperatures.

On the contrary, the (2x2)-(O+CO) structure, with one O atom and one CO molecule per unit cell (the O atom occupying an fcc site, the CO molecule an on top site), is stable, and it survives annealing to 370 K [140]. A model of this structure is shown in figure 4.8.

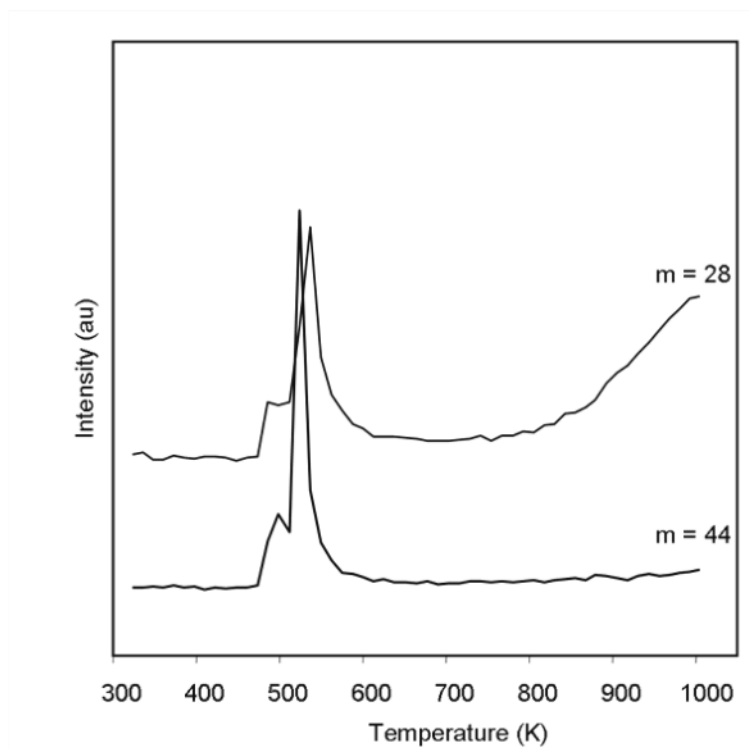


**Figure 4.7:** Thermal desorption spectra of masses 28 and 44 from the sample in the state shown in figure 4.5. Heating rate 5 K/s.

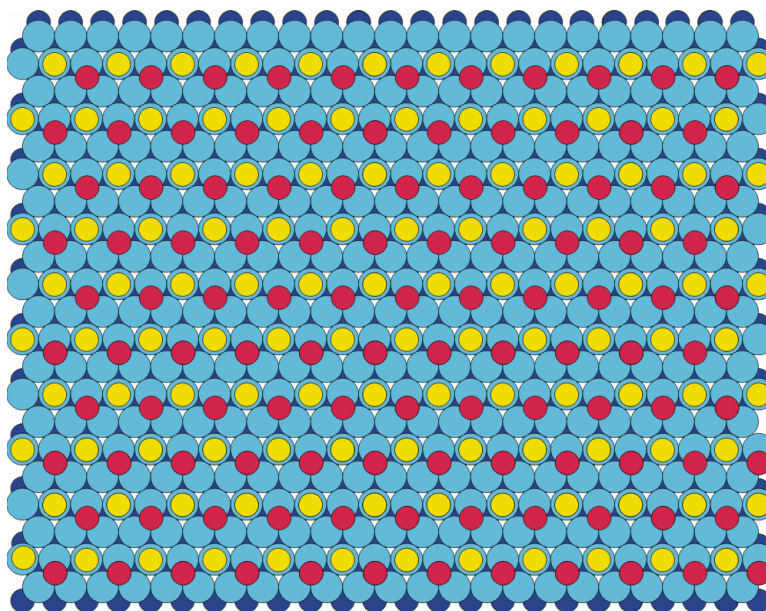


**Figure 4.8:** Model showing the (2x2) structure formed by oxygen atoms and CO molecules coadsorbed on the Rh(111) surface. The oxygen atoms (in red) occupy the fcc sites while the CO molecules (in yellow) are adsorbed in on top positions.

The TDS of figure 4.7 can be explained by a decomposition of the (2x2)-(O+CO) structure. One part of the CO desorbs during annealing, another reacts with oxygen to give CO<sub>2</sub> (the peak temperatures are roughly in agreement with the reported values of 450 K [125]), the remaining oxygen reacts with slowly segregating carbon at higher temperature.

This deactivation of the Rh(111) surface, e.g., for the oxidation of hydrogen, does not involve carbon segregation from the bulk to the surface. However, at higher temperatures this process also happens, similarly as for the Ru(0001) case, as indicated by the following experiment.

After exposing the surface to 50 L of oxygen at 550 K, above the desorption temperature of CO and CO<sub>2</sub>, but below the desorption temperature of O<sub>2</sub> (~970 K [137]), neither oxygen desorption nor the peaks of CO or CO<sub>2</sub> at ~500 K are observed, but only the high temperature peak of CO (figure 4.9).

The absence of these peaks is simply caused by the fact that the adsorption temperature was higher than the CO/CO<sub>2</sub> desorption peaks. However the slowly increasing production of CO between 700 and 900 K indicates the presence of C and O atoms on the surface. Oxygen is still present from the adsorption, carbon most likely segregates from the bulk to the surface where it reacts with O atoms to give CO. In this way the absence of O<sub>2</sub> desorption can be understood. The slow bulk diffusion of C atoms may account for the slow kinetics of the process. Additionally, CO may be desorbing from the increasingly hot parts of the sample manipulator.

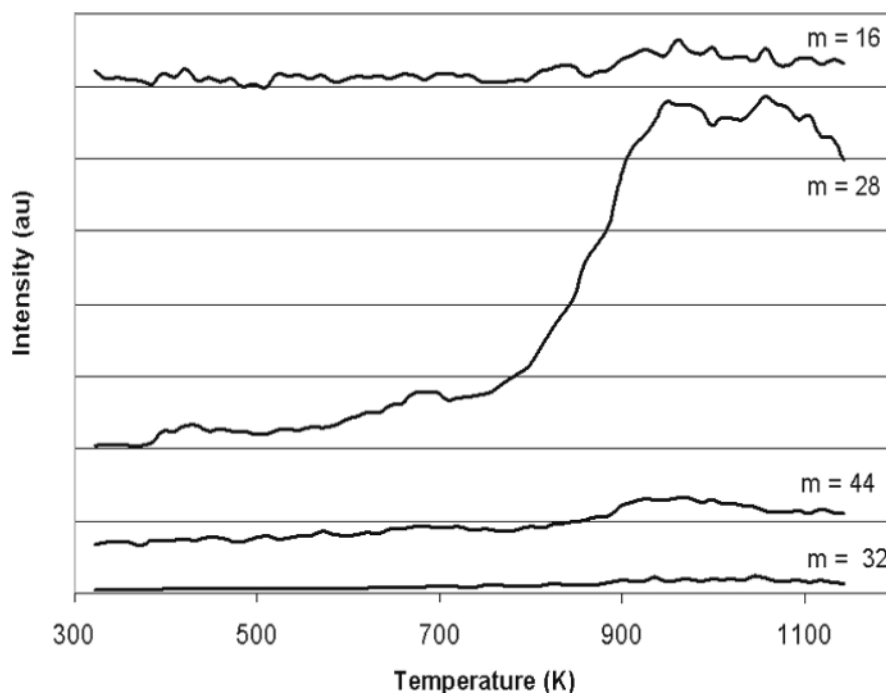


**Figure 4.9:** Thermal desorption spectra of masses 16, 28, 32 and 44 recorded after dosing 50 L O<sub>2</sub> at 550 K. Heating rate 5 K/s.

## 4.5 Discussion

The presence of CO during the adsorption of oxygen on the Rh(111) surface results in the formation of an ordered (2x2)-(O+CO) structure. This structure is almost static, even at its domain boundaries, and does not react with hydrogen. CO is known for its poisoning effects on transition metal surfaces. STM experiments of hydrocarbon hydrogenation reactions on the surfaces of Rh(111) and Pt(111) have shown that the presence of CO inhibits the reactions by forming ordered immobile structures [141, 142]. This has a double effect: first, CO molecules block the active sites for the reaction and, secondly, the immobile structures formed by CO hinders the diffusion of the reactants and stops the reaction. In both cases the poisoning action of CO is explained in terms of geometrical effects. For the H<sub>2</sub> oxidation on Rh(111) the presence of CO on the surface blocks empty sites necessary for the dissociative adsorption of the hydrogen molecules. Since this is a fundamental step of the reduction reaction, the surface is no longer reactive to H<sub>2</sub>.

The source of the CO could be the carbon monoxide content of the residual gas in the UHV chamber. During the time of the unintentional formation of the (2x2)-(O+CO) structure the background pressure decreased more slowly after the preparation and dosing steps, and the composition of the background pressure showed small changes. None of these changes appeared serious, and the ultimate base pressure was not significantly worse than during the experiments in which the pure oxygen overlayers could be prepared. However, the typical time scale of STM experiments of more than 1 h can have led contamination by CO. Alternatively, CO could have been formed by reaction of O<sub>2</sub> with some carbon species present in the chamber during the dosing.

## 4.6 Conclusions

The STM data prove that under clean adsorption conditions both the (2x2)O and the (2x1)O structures can be prepared on Rh(111). At 300 K and at the saturation coverage of  $\Theta(\text{O}) = 0.5$  ML large domains of the well ordered (2x1)O phase exist. The (2x2)O phase is only resolved at low temperatures, in agreement with the known order-disorder transition of this structure. The disordered phase at  $\Theta(\text{O}) = 0.25$  ML and 300 K is too mobile for resolution by STM. With respect to reactivity with O<sub>2</sub> the Rh(111) surface is thus more similar to Ru(0001), which also forms a (2x1)O phase at 300 K, than to Pd, which saturates at a (2x2)O structure.

The (2x2) structure observed at oxygen saturation in earlier STM work is caused by the (2x2)-(O+CO) phase. This structure easily forms by unnoticed CO formation or coadsorption during O<sub>2</sub> dosing even under seemingly acceptable vacuum conditions. This problem may have also existed in some of the previous structural and spectroscopic work on Rh(111)/O.



## Conclusions and outlook

In this work STM was employed to investigate fundamental aspects of catalyst poisoning and deactivation on two model systems, namely the Ru(0001) and the Rh(111) surfaces. It was shown that the Ru(0001) surface can become deactivated by graphitic carbon after prolonged annealing of the sample in UHV. Carbon segregates from the bulk of the crystal to the surface where the growth of graphite is self-limited to a monoatomic layer (graphene) covering the entire surface. The dependence of the graphene coverage on the annealing temperature was investigated with AES. It was shown that the threshold for C segregation is 1000 K while the total coverage is reached by annealing at 1400 K. The structure of graphene on the Ru(0001) surface was investigated in detail with STM and LEED. The lattice mismatch between graphene and Ru(0001) results in the formation of an (11x11) superstructure. The two lattices come into coincidence every 11 metal unit cells and every 12 graphene cells, corresponding to a periodicity of 3 nm. The superstructure is characterized by a pronounced apparent corrugation of up to  $\sim 1.5$  Å. Graphene has a preferential orientation aligned along the  $[10\bar{1}0]$  direction of the ruthenium lattice. Only in few cases a slight rotation of  $1^\circ$  between the two lattices was observed which nevertheless does not affect the 3 nm periodicity of the superstructure. The Ru surface restructures during the C segregation process so that the metal steps are aligned along the main directions of the overlayer. Images with atomic resolution display a moiré pattern and are characterized by the imaging of the two C atoms in the graphene unit cell depending on their relative position with respect to the

underlying metal sites. Only the C atoms lying above threefold hollow sites appear bright in the STM images while those directly above the metal atoms are not visible. Since the positions of the C atoms shift continuously with respect to the underlying lattice, the same STM image alternatively reveals the A and B atoms of the graphene unit cell. In intermediate regions both atoms (i.e. the entire graphene rings) are visible. Such a contrast shift from one type of carbon atom to the other within the same STM image has never been reported before neither in high resolution STM images of bulk graphite, nor in the case of graphene deposited on metal surfaces.

The perfect orientation of the (11x11) graphene structure, the absence of other moiré phases, the restructuring of the metal step edges and the relatively small ( $\sim 1.8$  Å) apparent height of the graphene layer above the metal measured by STM indicate a substantial interaction between graphene and ruthenium. In this respect, Ru behaves differently from Pt and Ir which display a weaker bonding between the metal and the graphene.

The system is characterized by strong voltage dependent imaging properties. For tunneling voltages above +0.6 V (empty states) pronounced rings appear around the moiré maxima. For this reason the surface electronic structure was investigated by Scanning Tunneling Spectroscopy. Indications of a gap opening at the K point of the graphene Brillouin zone at  $E_F$  were found. This result was confirmed by measuring the inverse decay length of the tunneling current for graphene on Ru(0001). It was shown that for voltages within the band gap only the metal states contribute to the tunneling current. This measurement also showed that for positive voltages above +1.0 V the graphene inverse decay length has a pronounced minimum indicating that the ring structure is connected with a state with low wave vector component parallel to the tunneling junction. It was postulated that this state corresponds to the surface state calculated for bulk graphite at  $\sim +3$  eV, and it was assumed that it is shifted down in energy upon bond formation between graphene and ruthenium.

A cooperation with the group of M. L. Bocquet (École Normale Supérieure de Lyon) performing DFT calculation, has been started. The aim is to get more insight into the structure of the moiré unit cell and to find out in how far the large corrugations measured by STM represent the geometry or are caused by electronic effects. It will be analyzed how one can understand the obvious deviations of the bond between the graphene and the metal from a Van-der-Waals interaction. The electronic structure of the system will be investigated as well to understand the STS results.

A further cooperation has been started with the group of N. Lorente (Institute of Material Science of Barcelona) in order to simulate STM images to characterize the imaging switch between the A and B atoms and to clarify the mechanism leading to the rings formation at positive tunneling voltages.

It has been shown that graphene on Ru(0001) fulfils a series of requirements as template for engineering nanostructures: it has an ordered structure over macroscopic areas of the sample, it is easy to prepare and chemically inactive. Its properties as template for the growth of ordered arrays of nanostructures are currently under investigation. Preliminary results for gold deposition at room temperature have been obtained. Gold forms islands with a compact shape on the graphene areas, unlike the characteristic fractal shape observed on the bare metal. However, the Au islands grown on graphene are still too large to investigate, e.g., size-dependent catalytic properties. For this reason in the future the deposition temperature will be lowered. Deposition of other metals will also be tried.

The poisoning effects of CO on oxygen adsorption on Rh(111) were investigated in the second part of this work. It was shown that the oxygen saturation coverage of the Rh(111) surface in clean conditions is 0.5 ML corresponding to the presence of a (2x1) structure. In this sense, Rh displays the same behavior as Ru, the left neighbor in the periodic table, while Pd, the right and therefore less active neighbor, has an oxygen saturation coverage of only 0.25 ML.

The mobility of oxygen on Rh(111) is very high at room temperature. The domain boundaries of the (2x1) structure display fluctuations on a time scale of  $\sim 0.1$  s. Oxygen mobility was also reported for low oxygen coverages and it was shown that, in order to resolve by STM the ordered (2x2) phase, corresponding to an oxygen coverage of 0.25 ML, it is necessary to lower the sample temperature to 60 K. Both structures are highly reactive to H<sub>2</sub> at room temperature.

In the presence of CO, a static (2x2) structure was observed. This structure corresponds to a coadsorbed (O+CO) phase with O atoms on fcc sites and CO molecules on top. TPD experiments on this system show desorption of CO and CO<sub>2</sub> while no oxygen desorption is observed. CO deactivates the surface with respect to H<sub>2</sub> by blocking empty sites necessary for the dissociative adsorption of H<sub>2</sub>, a fundamental step of the reduction reaction.



## Appendix A

### **Ru(0001) contamination at low temperature: the “gray atoms”**

After cooling the freshly prepared sample to 50 K, it appears as displayed in figure A.1. The surface is populated by a chemical species appearing as depression with triangular shape. All triangles have the same orientation. This shape suggests the adsorption in one of the two threefold hollow sites of the surface as observed, for example, for N atoms on Ru(0001) [143]. The coverage, obtained by averaging several images measured on several days, is about 0.08ML. The formation of ordered structures or of islands was never observed, but the particles are randomly distributed.

Since the STM technique does not allow identifying the chemical nature of species covering the surface, XPS and AES measurements were performed.

XPS was performed in a separate UHV chamber that is not equipped with facilities for sample cooling. The XPS spectra taken at room temperature do not show any other peaks than those coming from Ru, confirming the STM result that the surface at 300 K is clean. (A small carbon contamination can, however, not be ruled out because the C 1s peak unfortunately coincides with the  $3d_{3/2}$  peak of Ru).

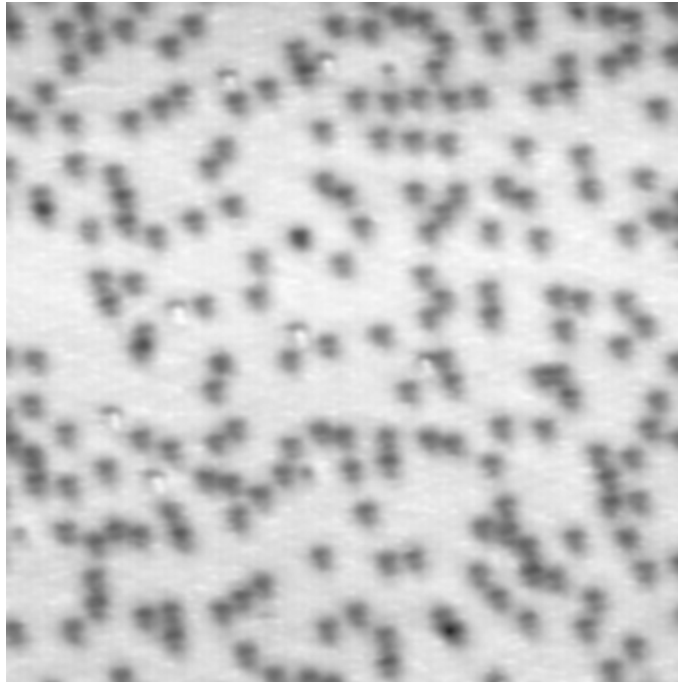
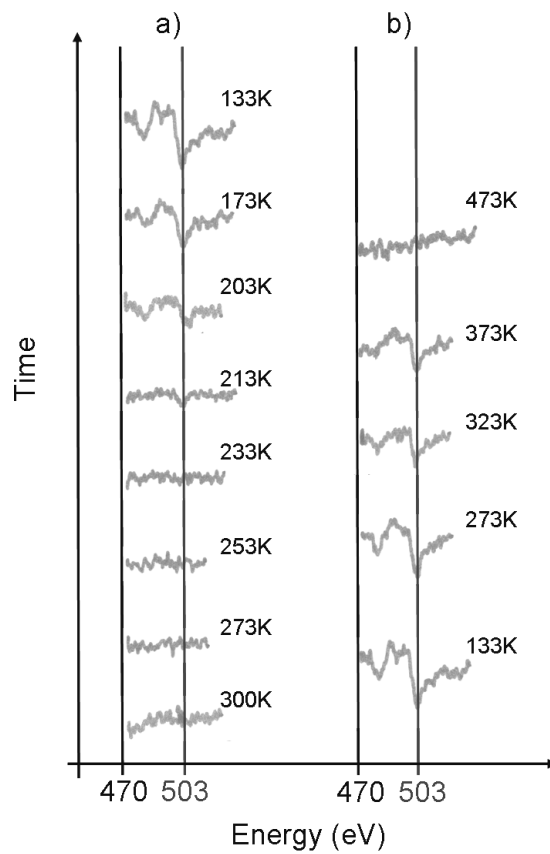


**Figure A.1:** STM image taken at 50 K. The surface is populated by a chemical species appearing as triangular depression. 20 nm x 20 nm,  $I_t = 1$  nA,  $U = +0.5$  V.

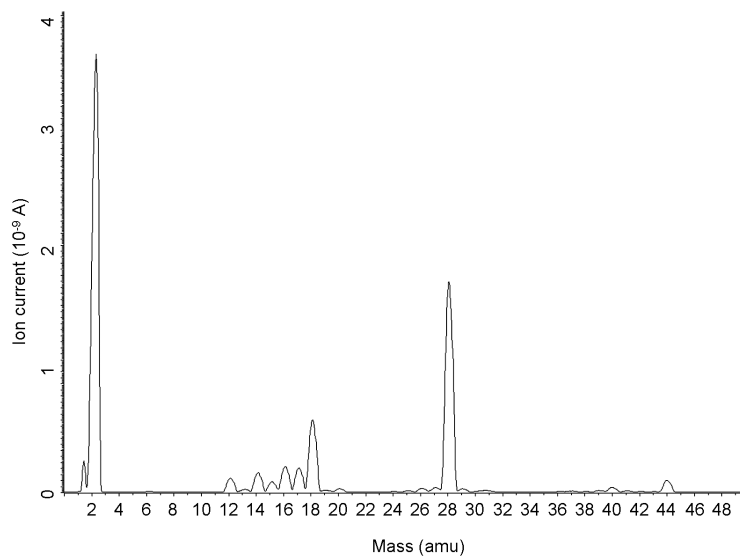
AES measurements were performed in the variable temperature STM chamber where it is possible to cool the sample with liquid nitrogen while measuring the spectra. The spectra taken at room temperature do not display the presence of contaminants on the surface. However, while cooling down the sample a transition at 503 eV appears, caused by the KLL transition of oxygen, which indicates the presence of an oxygen containing species [43] on the surface (figure A.2).

Figure A.2a displays several AES spectra in the region around 500 eV measured while cooling down from 300 K to 133 K. The spectra between 300 K and 233 K do not show any feature in this energy range. When the temperature reaches 213 K, a feature at 503 eV appears that increases in intensity when the temperature further decreases to 133 K. Figure A.2b displays spectra recorded upon annealing the sample and keeping it at the elevated temperature. The additional peak remains after the annealing stops at 273 K, 323 K and 373 K, but the intensity decreases. The flash to 473 K completely removes the oxygen containing species. This process is perfectly reversible: upon cooling the sample again the oxygen feature appears in the spectra when the temperature is lower than 230 K. The AES experiments clearly reveal an unintended adsorption of an oxygen containing species at temperatures below 230 K and its removal with a flash to 473 K.

Figure A.3 shows a typical background spectrum measured with the QMS when the pressure in the chamber is  $3 \cdot 10^{-10}$  mbar which is the maximum value during the sample cooling either in STM or in front of the AES optics.



**Figure A.2:** AES spectra taken in the region 470 eV–530 eV. a) Spectra measured during cooling of the sample. When the temperature is lower than 213 K a feature develops at 503 eV revealing the presence of an oxygen containing species on the surface. b) The sample cooled to 133 K is annealed and kept at higher temperatures. Annealing to 473 K removes the oxygen containing species from the surface.



**Figure A.3:** Mass spectrum measured at a background pressure of  $3 \cdot 10^{-10}$  mbar.

The main peaks are masses 2, 18 and 28 associated with hydrogen, water and carbon monoxide, respectively, in the residual gas of the chamber. Minor peaks at 12, 14, 15, 16, 17, 40, 44 are associated with low amounts of further chemical species or of cracking products of the main species ( $C^+$ ,  $CH_2^+$ ,  $CO_2^+$ ,  $CH_3^+$ ,  $O^+$ ,  $CH_4^+$ ,  $OH^+$ ,  $Ar^+$ ,  $CO_2^+$ ). The spectrum is a quite typical residual gas spectrum of a UHV chamber in the low  $10^{-10}$  mbar pressure range.

The presence of  $H_2O$ ,  $CO$  and  $CO_2$  in the residual gas suggests that the oxygen containing species that appears on the surface must be either water or carbon monoxide or dioxide or a dissociation product like  $OH$  or atomic oxygen adsorbed during the cooling procedure.

The identification of the “gray atoms” with atomic oxygen can be excluded for two reasons. The first reason is that the behavior of atomic oxygen on the  $Ru(0001)$  surface is not compatible with the observation in the AES spectra that the oxygen containing species has already desorbed from the surface after a flash to 473K. From the extensive literature about oxygen on  $Ru(0001)$  it is well known that oxygen is strongly bound to the metal [144], and as a consequence the desorption occurs at temperatures higher than 1100K [39]. The desorption temperature depends on the oxygen coverage, and it ranges from 1100 K for the saturated surface to 1500 K for low coverages [145]. The second reason can be seen in figure A.4. It shows an STM image of the surface at 50 K that was recorded after dosing 0.4L of  $O_2$  at the same temperature. The presence of atomic oxygen is clearly revealed by the presence of black features appearing as pairs or forming small islands. It is well known that adsorbed oxygen on metal surfaces is generally imaged dark, i.e. as a depression. This observation is an electronic effect caused by the electronegativity of the oxygen atoms that lowers the electron density at  $E_F$  [146]. Upon adsorption on  $Ru(0001)$ , molecular oxygen dissociates [147] and the pairs of atoms displayed in the image are single atoms of oxygen after the dissociation. It is also known that at low temperatures oxygen forms disordered islands with a disorder-order transition temperature of about 300K [39].

Figure A.5 shows the surface after dosing 0.5 L  $O_2$  at room temperature and cooling down to 150K. Oxygen atoms form (2x2) islands and display a circular shape with the typical pronounced depth in the STM images. The “gray atoms”, on the contrary, appear less deep than oxygen, have a triangular shape and, interestingly, some of them are incorporated in the (2x2) islands formed by oxygen suggesting the same adsorption site. Oxygen at low coverage at room temperature is known to form (2x2) islands on the  $Ru(0001)$  surface, with O atoms occupying the hcp sites [148, 149]. It can be concluded that the “gray atoms” are adsorbed in the hcp sites as well.

It is clear that the “gray atoms” are imaged differently from the oxygen atoms in the STM images and that they exhibit a different ordering behavior. The “gray atoms” are clearly not single oxygen atoms.

The desorption of the oxygen containing species at about 470 K as measured in the AES experiment of figure A.2b is compatible with the behavior of  $CO$  adsorbed on  $Ru(0001)$ . TDS experiments performed for several  $CO$  initial coverages show that the  $CO$  desorption temperature varies between 400 K and 530 K depending on the coverage [150].

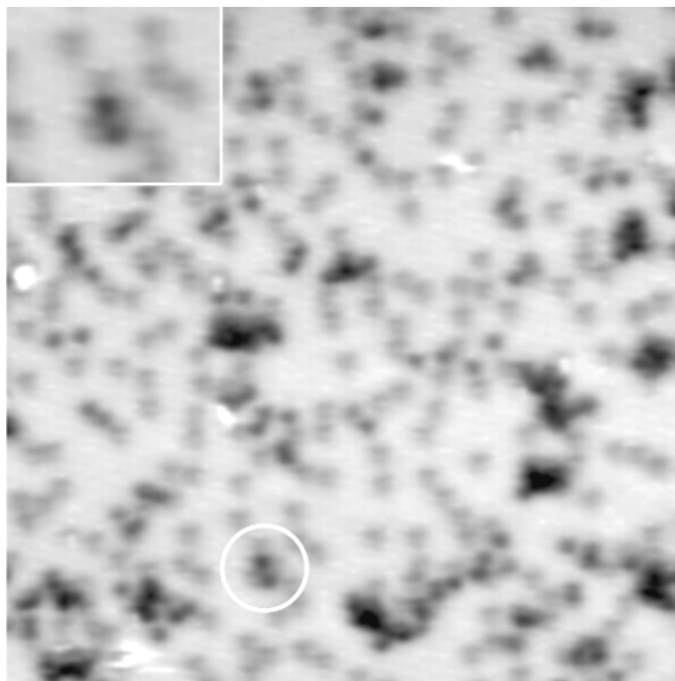


**Figure A.4:** STM image taken at 50 K after dosing 0.4 L O<sub>2</sub>. The atomic oxygen appears as deep depression on the surface and it is different from the “gray atoms”. The inset shows an enlargement of one of the oxygen’s pair (marked in the picture by the circle). 20 nm x 20 nm,  $I_t = 1$  nA,  $U = +0.4$  V.

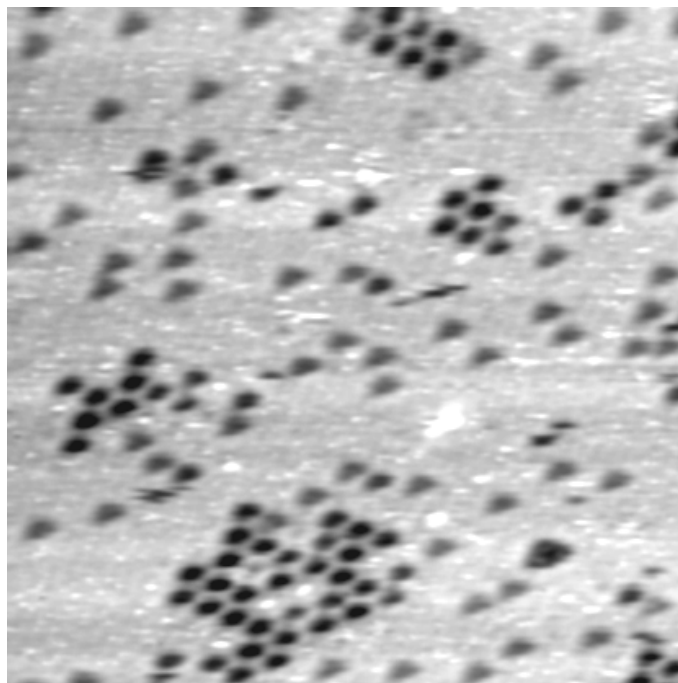


**Figure A.5:** STM image taken at 150 K after dosing 0.5 L O<sub>2</sub> at room temperature. Oxygen forms a (2x2) structure, and some of the gray atoms are incorporated into this structure suggesting the same hcp adsorption site as oxygen. 10 nm x 10 nm,  $I_t = 1$  nA,  $U = -0.8$  V.

For this reason CO was dosed at 50 K in order to compare its behavior in STM with the behavior of the “gray atoms”. One image is shown in figure A.6 displaying the surface after dosing 1 L CO at 50 K. The first hint that the “gray atoms” are not CO molecules is the fact that CO molecules are imaged as protrusions. Furthermore, CO forms ordered islands with  $(\sqrt{3} \times \sqrt{3})$  symmetry even at 50 K (in agreement with the results reported in the literature [59]), while the “gray atoms” are randomly distributed.

It is not likely that the “gray atoms” are due to CO<sub>2</sub> on the surface because CO<sub>2</sub> is known to dissociate into adsorbed CO and O even at low temperatures on metal surfaces like the Rh(111) [151] and the Re(0001) [152] surfaces. A similar behavior on the highly reactive Ru(0001) surface is expected but a dissociation of a “gray atom” into CO and atomic oxygen was never observed. Furthermore, the partial pressure of CO<sub>2</sub> in the background is lower than the partial pressure of CO (figure A.3) and, assuming similar sticking coefficients for both molecules, it would be expected to observe the adsorption of both of them during the cooling procedure.

The adsorption of water on the Ru(0001) surface and, in general, on transition metal surfaces, is an interesting problem and it has been widely investigated. The attention has been particularly focused on the high coverages systems ( $0.25 \text{ ML} < \Theta < 0.76 \text{ ML}$ ), and it has been found that water on ruthenium partially dissociates and organizes into supramolecular units. These consist of water molecules bonded by hydrogen bonds to OH groups in a hexagonal structure [153] with a  $(\sqrt{3} \times \sqrt{3})$  symmetry. This structure forms at temperatures as low as 105 K [154]. In the present context the behavior of water at very low coverages ( $\Theta \sim 0.08 \text{ ML}$ ) is important in order to understand whether the “gray atoms” could be interpreted as water monomers or hydroxyls groups. In a recent theoretical study [155], Michaelides and coworkers has determined that the most stable site for H<sub>2</sub>O monomers adsorption is the on top site with a binding energy of 0.38 eV and that the other sites, with adsorption energies of 0.1 eV or less, are disfavored. This property is in contrast to the observation in STM of the adsorption of the “gray atoms” in the hcp threefold sites. Furthermore, TDS experiments show that water desorbs at temperatures below 200 K [156] in contrast to the observation that the surface has to be annealed to 473 K in order to remove the oxygen containing species. Michaelides and coworkers [155] also investigated the dissociation of the H<sub>2</sub>O monomers. An activation energy for this process of 0.8 eV was found, suggesting that water should not dissociate at low temperatures. It was furthermore calculated that, once the activation barrier is overcome, the dissociation products OH and H are more stable than H<sub>2</sub>O by 0.27 eV, revealing a thermodynamic driving force toward the dissociation. The OH groups are strongly bound to the threefold sites with a slight preference for the fcc sites (adsorption energy of 3.21 eV) over the hcp sites (adsorption energy 3.10 eV). Since, according to the AES measurements of figure A.2, the adsorption of the oxygen containing species takes place at a temperature below 230 K, the work by Michaelides does not directly favor an interpretation of the “gray atoms” as OH groups deriving from the dissociation of H<sub>2</sub>O from the gas phase.

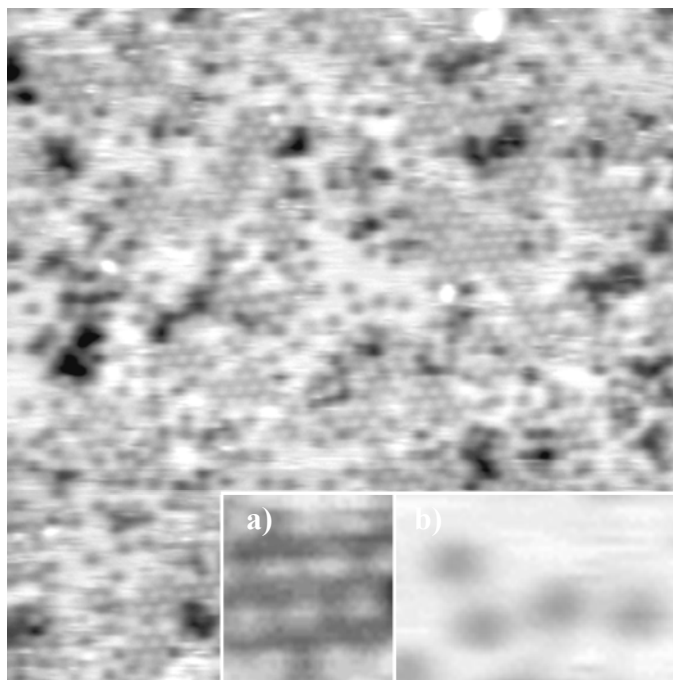


**Figure A.6:** STM image taken at 50 K after dosing 1L CO. CO molecules appear as protrusions (inset a) forming islands with a  $(\sqrt{3} \times \sqrt{3})$  structure. Inset b shows an enlargement of the “gray atoms”. Black islands indicate the presence of residual oxygen on the surface. 20 nm x 20 nm,  $I_t = 1$  nA,  $U = +0.4$  V.

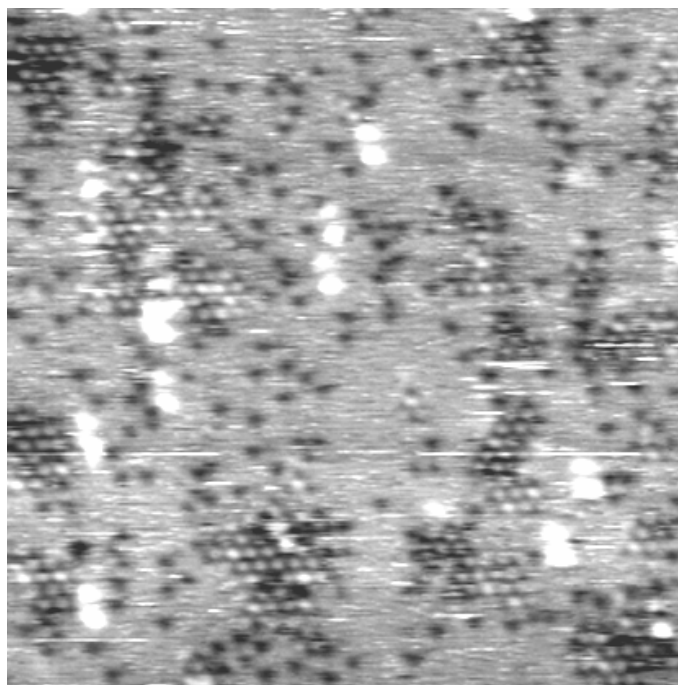


**Figure A.7:** STM image taken at 150 K after dosing 150 L of Ar. Ar forms islands with a  $(2 \times 2)$  structure. 20 nm x 20 nm,  $I_t = 1$  nA,  $U = -0.8$  V.

The adsorption in the threefold sites would explain the triangular shapes of the “gray atoms” in STM but images like the one shown in figure A.5 show clearly that the contaminants occupy the hcp sites. Nevertheless, from the current precision of DFT an hcp adsorption site of the OH fragment and a lower activation energy for the H<sub>2</sub>O dissociation can probably not be ruled out. Furthermore the “gray atoms” occur as the temperature is slowly decreasing, whereas their coverage does not further increase at a constant low temperature of 50 K.

Even though the AES experiment of figure A.2 points to a contamination by an oxygen containing species, the low temperature adsorption behavior of other gases was also checked.

First of all, since H<sub>2</sub> is the main component of the residual gas in the UHV chamber (figure A.3), H<sub>2</sub> was intentionally dosed at a partial pressure of  $1 \cdot 10^{-8}$  mbar while monitoring the surface in STM at 50 K. No increase in the coverage of the “gray atoms” was observed.

Finally, Ar was dosed at 50 K, as it is one of the gases employed in the sample preparation procedure and it is also present in the residual gas. However, the formation of (2x2) islands of protrusions was observed, which is again not consistent with the behavior of the “gray atoms” (figure A.7).

In conclusion, the “gray atoms” occurring at low temperatures on the Ru(0001) surface can not be identified with absolute certainty. The most likely interpretation is adsorbed OH from the H<sub>2</sub>O in the residual gas. Even by modifying the cleaning and cooling procedure it was not possible to reduce the coverage of this species below  $\sim 0.08$  ML. The presence of this contaminant may influence the catalytical properties of the surface and complicate STM experiments on the Ru(0001) surface at low temperatures.





## References

- [1] C. H. Bartholomew, *Applied Catalysis A-General* **212** (2001) 17.
- [2] C. J. H. Jacobsen, *Journal of Catalysis* **200** (2001) 1.
- [3] A. Haynes, P. M. Maitlis, G. E. Morris, et al., *Journal of the American Chemical Society* **126** (2004) 2847.
- [4] T. A. Pecoraro and R. R. Chianelli, *Journal of Catalysis* **67** (1981) 430.
- [5] S. Iijima, *Nature* **354** (1991) 56.
- [6] R. E. Smalley, *Reviews of Modern Physics* **69** (1997) 723.
- [7] K. S. Novoselov, A. K. Geim, S. V. Morozov, et al., *Science* **306** (2004) 666.
- [8] K. S. Novoselov, A. K. Geim, S. V. Morozov, et al., *Nature* **438** (2005) 197.
- [9] J. C. Meyer, A. K. Geim, M. I. Katsnelson, et al., *Nature* **446** (2007) 60.
- [10] A. K. Geim and K. S. Novoselov, *Nature Materials* **6** (2007) 183.
- [11] K. S. Novoselov, D. Jiang, F. Schedin, et al., *Proceedings of the National Academy of Sciences of the United States of America* **102** (2005) 10451.
- [12] J. V. Barth, G. Costantini, and K. Kern, *Nature* **437** (2005) 671.
- [13] B. D. Gates, Q. B. Xu, M. Stewart, et al., *Chemical Reviews* **105** (2005) 1171.
- [14] T. Ito and S. Okazaki, *Nature* **406** (2000) 1027.
- [15] M. Valden, X. Lai, and D. W. Goodman, *Science* **281** (1998) 1647.
- [16] N. Weiss, T. Cren, M. Epple, et al., *Physical Review Letters* **95** (2005).
- [17] G. Binnig, H. Rohrer, C. Gerber, et al., *Applied Physics Letters* **40** (1982) 178.
- [18] R. J. Behm and W. Hösler, *Chemistry and Physics of Solid Surfaces VI (Springer, Berlin)*, (1986).
- [19] R. Wiesendanger, *Scanning Probe Microscopy and Spectroscopy. Methods and Applications*, (1994).
- [20] J. Bardeen, *Physical Review Letters* **6** (1961) 57.

- [21] J. Tersoff and D. R. Hamann, *Physical Review Letters* **50** (1983) 1998.
- [22] J. Tersoff and D. R. Hamann, *Physical Review B* **31** (1985) 805.
- [23] R. J. Hamers, *Annual Review of Physical Chemistry* **40** (1989) 531.
- [24] N. D. Lang, *Physical Review B* **34** (1986) 5947.
- [25] R. M. Feenstra, J. A. Stroscio, and A. P. Fein, *Surface Science* **181** (1987) 295.
- [26] V. A. Ukraintsev, *Physical Review B* **53** (1996) 11176.
- [27] B. Koslowski, C. Dietrich, A. Tschetschetkin, et al., *Physical Review B* **75** (2007).
- [28] K. Besocke, *Surface Science* **181** (1987) 145.
- [29] J. Frohn, J. F. Wolf, K. Besocke, et al., *Review of Scientific Instruments* **60** (1989) 1200.
- [30] M. Rößler, P. Geng, and J. Wintterlin, *Review of Scientific Instruments* **76** (2005) 023705.
- [31] S. Günther (1995) Dissertation "Mikroskopische Aspekte beim Wachstum dünner Metallfilme"
- [32] S. Behler, M. K. Rose, D. F. Ogletree, et al., *Review of Scientific Instruments* **68** (1997) 124.
- [33] W. H. Press, S. A. Teukolsky, W. T. Vetterling, et al., *Numerical Recipes in Fortran 77: the Art of Scientific Computing* (Cambridge University Press, (1986).
- [34] A. Savitzky and M. J. E. Golay, *Analytical Chemistry* **36** (1964) 1627.
- [35] M. U. A. Bromba and H. Ziegler, *Analytical Chemistry* **53** (1981) 1583.
- [36] P. Marchand and L. Marmet, *Review of Scientific Instruments* **54** (1983) 1034.
- [37] C. H. Reinsch, *Numerische Mathematik* **10** (1967) 177.
- [38] T. Zambelli, J. Wintterlin, J. Trost, et al., *Science* **273** (1996) 1688.
- [39] T. E. Madey, H. A. Engelhardt, and D. Menzel, *Surface Science* **48** (1975) 304.
- [40] M. Rößler (2003) Dissertation "Rastertunnelmikroskopie bei hohen Drücken"
- [41] C. D. Wagner, W. M. Riggs, L. E. Davis, et al., *Handbook of X-ray photoelectron spectroscopy* (Perkin Elmer, (1979).
- [42] N. W. Ashcroft and N. D. Mermin, *Solid State Physics* (Saunders College Publishing, (1976).
- [43] L. E. Davis, N. C. MacDonald, P. W. Palmberg, et al., *Handbook of Auger Electron Spectroscopy*, (1978).
- [44] M. J. Van Staden and J. P. Roux, *Applied Surface Science* **44** (1990) 259.
- [45] L. Atanasoska, W. E. Ogrady, R. T. Atanasoski, et al., *Surface Science* **202** (1988) 142.
- [46] D. W. Goodman and J. M. White, *Surface Science Letters* **90** (1979) 201.
- [47] F. J. Himpsel, K. Christmann, P. Heimann, et al., *Surf. Sci.* **115** (1982) L159.
- [48] R. Rosei, M. D. Crescenzi, F. Sette, et al., *Phys. Rev. B* **28** (1983) 1161.
- [49] C. F. McConville, D. P. Woodruff, and S. D. Kevan, *Surf. Sci.* **171** (1986) L447.
- [50] T. A. Land, T. Michely, R. J. Behm, et al., *Surf. Sci.* **264** (1992) 261.
- [51] H. B. Lyon and G. A. Somorjai, *J. Chem. Phys.* **46** (1967) 2539.
- [52] J. C. Shelton, H. R. Patil, and J. M. Blakely, *Surf. Sci.* **43** (1974) 493.
- [53] J. C. Hamilton and J. M. Blakely, *Surf. Sci.* **91** (1980) 199.
- [54] J. T. Grant and T. W. Haas, *Surf. Sci.* **21** (1970) 76.
- [55] M. C. Wu, Q. Xu, and D. W. Goodman, *J. Phys. Chem.* **98** (1994) 5104.
- [56] J. Tersoff, *Phys. Rev. Lett.* **57** (1986) 440.

- [57] J. Wintterlin and T. Zambelli, *Z. Phys. Chem.* **219** (2005) 997.
- [58] K. Kobayashi, *Physical Review B* **53** (1996) 11091.
- [59] E. D. Williams and W. H. Weinberg, *Surface Science* **82** (1979) 93.
- [60] K. M. Ostyn and C. B. Carter, *Surf. Sci.* **121** (1982) 360.
- [61] D. Tománek and S. G. Louie, *Physical Review B* **37** (1988) 8327.
- [62] D. Tománek, S. G. Louie, H. J. Mamin, et al., *Phys. Rev. B* **35** (1987) 7790.
- [63] I. P. Batra, N. Garcia, H. Rohrer, et al., *Surface Science* **181** (1987) 126.
- [64] A. L. Tchougreeff and R. Hoffmann, *J. Phys. Chem.* **96** (1992) 8993.
- [65] F. R. Wagner and M. B. Lepetit, *Journal of Physical Chemistry* **100** (1996) 11050.
- [66] M.-H. Whangbo, W. Liang, J. Ren, et al., *J. Phys. Chem.* **98** (1994) 7602.
- [67] F. Atamny, O. Spillecke, and R. Schlögl, *Phys. Chem. Chem. Phys.* **1** (1999) 4113.
- [68] A. N'Diaye, S. Bleikamp, P. J. Feibelman, et al., *Phys. Rev. Lett.* **97** (2006) 215501.
- [69] M. Corso, W. Auwarter, M. Muntwiler, et al., *Science* **303** (2004) 217.
- [70] R. Laskowski, P. Blaha, T. Gallauner, et al., *Phys. Rev. Lett.* **98** (2007) 106802.
- [71] A. Goriachko, Y. He, M. Knapp, et al., *Langmuir* **23** (2007) 2928.
- [72] G. Boato, P. Cantini, and R. Tatarek, *Phys. Rev. Lett.* **40** (1978) 887.
- [73] M. Hasegawa and K. Nishidate, *Phys. Rev. B* **70** (2004) 205431.
- [74] P. J. Feibelman, *Surface Science Letters* **103** (1981) L149.
- [75] Y. Gamo, A. Nagashima, M. Wakabayashi, et al., *Surf. Sci.* **374** (1997) 61.
- [76] H. Zi-Pu, D. F. Ogletree, M. A. Van Hove, et al., *Surf. Sci.* **180** (1987) 433.
- [77] P. J. Feibelman, *Physical Review B* **26** (1982) 5347.
- [78] T. Aizawa, R. Souda, Y. Ishizawa, et al., *Surf. Sci.* **237** (1990) 194.
- [79] T. Aizawa, R. Souda, S. Otani, et al., *Phys. Rev. Lett.* **64** (1990) 768.
- [80] A. Nagashima, K. Nuka, K. Satoh, et al., *Surface Science* **287/288** (1993) 609.
- [81] C. Oshima and A. Nagashima, *Journal of Physics: Condensed Matter* **9** (1997) 1.
- [82] Y. Souzu and M. Tsukada, *Surf. Sci.* **326** (1995) 42.
- [83] B. Hammer and J. K. Nørskov, *Adv. Catal.* **45** (2000).
- [84] P. R. Wallace, *Phys. Rev.* **71** (1947) 622.
- [85] R. Rosei, S. Modesti, F. Sette, et al., *Phys. Rev. B* **29** (1984) 3416.
- [86] K. Kobayashi and M. Tsukada, *Phys. Rev. B* **49** (1994) 7660.
- [87] A. Nagashima, H. Itoh, T. Ichinokawa, et al., *Phys. Rev. B* **50** (1994) 4756.
- [88] A. Nagashima, N. Tejima, Y. Gamou, et al., *Phys. Rev. B* **51** (1995) 4606.
- [89] M. Posternak, A. Baldereschi, A. J. Freeman, et al., *Phys. Rev. Lett.* **52** (1984) 863.
- [90] T. Fauster, F. J. Himpsel, J. E. Fischer, et al., *Phys. Rev. Lett.* **51** (1983) 430.
- [91] B. Reihl, J. K. Gimzewski, J. M. Nicholls, et al., *Phys. Rev. B* **33** (1986) 5770.
- [92] Z. Klusek, *Appl. Surf. Sci.* **151** (1999) 251.
- [93] T. Straub, T. Finteis, R. Claessen, et al., *Physical Review Letters* **82** (1999) 4504.
- [94] P. Monceau, N. P. Ong, A. M. Portis, et al., *Physical Review Letters* **37** (1976) 602.
- [95] R. E. Thomson, B. Burk, A. Zettl, et al., *Physical Review B* **49** (1994) 16899.
- [96] A. H. Thompson, A. Zettl, and G. Gruner, *Physical Review Letters* **47** (1981) 64.
- [97] W. Sacks, D. Roditchev, and J. Klein, *Physical Review B* **57** (1998) 13118.
- [98] P. M. Echenique and J. B. Pendry, *Progress in Surface Science* **32** (1989) 111.

- [99] G. Binnig, K. H. Frank, H. Fuchs, et al., *Physical Review Letters* **55** (1985) 991.
- [100] R. S. Becker, J. A. Golovchenko, and B. S. Swartzentruber, *Physical Review Letters* **55** (1985) 987.
- [101] E. D. L. Rienks, N. Nilius, H. P. Rust, et al., *Physical Review B* **71** (2005).
- [102] M. Pivetta, F. Patthey, M. Stengel, et al., *Physical Review B* **72** (2005).
- [103] S. L. Weng, *Physical Review B* **25** (1982) 6188.
- [104] G. Seine, R. Coratger, A. Carladous, et al., *Physical Review B* **60** (1999) 11045.
- [105] N. A. W. Holzwarth and J. R. Chelikowsky, *Solid State Communications* **53** (1985) 171.
- [106] A. Selloni, P. Carnevali, E. Tosatti, et al., *Phys. Rev. B* **31** (1985) 2602.
- [107] R. E. Honig, *Rca Review* **23** (1962) 567.
- [108] R. Q. Hwang, J. Schroder, C. Gunther, et al., *Physical Review Letters* **67** (1991) 3279.
- [109] T. A. Witten and L. M. Sander, *Physical Review Letters* **47** (1981) 1400.
- [110] R. Q. Hwang, C. Gunther, J. Schroder, et al., *Journal of Vacuum Science & Technology a-Vacuum Surfaces and Films* **10** (1992) 1970.
- [111] R. Q. Hwang and R. J. Behm, *Journal of Vacuum Science & Technology B* **10** (1992) 256.
- [112] H. Xu and K. Y. S. Ng, *Surface Science* **375** (1997) 161.
- [113] S. Schwegmann and H. Over, *Surface Science* **393** (1997) 179.
- [114] H. Xu and K. Y. S. Ng, *Surface Science* **393** (1997) 181.
- [115] J. Gustafson, A. Mikkelsen, M. Borg, et al., *Physical Review Letters* **92** (2004).
- [116] H. Conrad, G. Ertl, J. Kupperts, et al., *Surface Science* **65** (1977) 245.
- [117] K. Meinel, H. Wolter, C. Ammer, et al., *Journal of Physics-Condensed Matter* **9** (1997) 4611.
- [118] C. Stampfl, S. Schwegmann, H. Over, et al., *Physical Review Letters* **77** (1996) 3371.
- [119] K. L. Kostov, M. Gsell, P. Jakob, et al., *Surf. Sci.* **394** (1997) L138.
- [120] Y. D. Kim, S. Wendt, S. Schwegmann, et al., *Surface Science* **418** (1998) 267.
- [121] H. Conrad, G. Ertl, and J. Kupperts, *Surface Science* **76** (1978) 323.
- [122] J. Mendez, S. H. Kim, J. Cerda, et al., *Physical Review B* **71** (2005).
- [123] K. D. Gibson, M. Viste, E. Sanchez, et al., *Journal of Chemical Physics* **112** (2000) 2470.
- [124] K. D. Gibson, M. Viste, E. C. Sanchez, et al., *Journal of Chemical Physics* **110** (1999) 2757.
- [125] S. Schwegmann, H. Over, V. DeRenzi, et al., *Surface Science* **375** (1997) 91.
- [126] K. C. Wong, W. Liu, and K. A. R. Mitchell, *Surface Science* **360** (1996) 137.
- [127] D. G. Castner and G. A. Somorjai, *Applied Surface Science* **6** (1980) 29.
- [128] X. P. Xu and C. M. Friend, *Journal of the American Chemical Society* **113** (1991) 6779.
- [129] K. A. Peterlinz and S. J. Sibener, *Surface Science* **344** (1995) L1239.
- [130] J. Wider, T. Greber, E. Wetli, et al., *Surface Science* **417** (1998) 301.
- [131] M. V. Ganduglia-Pirovano, M. Scheffler, A. Baraldi, et al., *Physical Review B* **6320** (2001).
- [132] M. V. Ganduglia-Pirovano and M. Scheffler, *Physical Review B* **59** (1999) 15533.
- [133] J. Wintterlin, R. Schuster, and G. Ertl, *Physical Review Letters* **77** (1996) 123.

- 
- [134] H. Over, S. Schwegmann, D. Cvetko, et al., *Physical Review B* **55** (1997) 4717.
- [135] J. T. Yates, P. A. Thiel, and W. H. Weinberg, *Surface Science* **82** (1979) 45.
- [136] L. A. D. Louise and N. Winograd, *Surf. Sci.* **138** (1984) 417.
- [137] D. G. Castner, B. A. Sexton, and G. A. Somorjai, *Surface Science* **71** (1978) 519.
- [138] T. Matsushima, T. Matsui, and M. Hashimoto, *Journal of Chemical Physics* **81** (1984) 5151.
- [139] L. H. Dubois and G. A. Somorjai, *Surface Science* **91** (1980) 514.
- [140] A. J. Jaworowski, A. Beutler, F. Strisland, et al., *Surface Science* **431** (1999) 33.
- [141] K. S. Hwang, M. C. Yang, J. Zhu, et al., *Journal of Molecular Catalysis a-Chemical* **204** (2003) 499.
- [142] M. Montano, M. Salmeron, and G. A. Somorjai, *Surface Science* **600** (2006) 1809.
- [143] J. Trost, T. Zambelli, J. Winterlin, et al., *Physical Review B* **54** (1996) 17850.
- [144] C. Stampfl, H. J. Kreuzer, S. H. Payne, et al., *Physical Review Letters* **83** (1999) 2993.
- [145] L. Surnev, G. Rangelov, and G. Bliznakov, *Surface Science* **159** (1985) 299.
- [146] N. D. Lang, *Commun. Condens. Matter Phys.* **14** (1989) 253.
- [147] W. J. Mitchell, J. Xie, K. J. Lyons, et al., *Journal of Vacuum Science & Technology a-Vacuum Surfaces and Films* **12** (1994) 2250.
- [148] C. Stampfl and M. Scheffler, *Physical Review B* **54** (1996) 2868.
- [149] M. Lindroos, H. Pfnur, G. Held, et al., *Surface Science* **222** (1989) 451.
- [150] J. A. Schwarz and S. R. Kelemen, *Surface Science* **87** (1979) 510.
- [151] L. H. Dubois and G. A. Somorjai, *Surface Science* **128** (1983) L231.
- [152] M. Asscher, C. T. Kao, and G. A. Somorjai, *Journal of Physical Chemistry* **92** (1988) 2711.
- [153] P. J. Feibelman, *Science* **295** (2002) 99.
- [154] J. Weissenrieder, A. Mikkelsen, J. N. Andersen, et al., *Physical Review Letters* **93** (2004).
- [155] A. Michaelides, A. Alavi, and D. A. King, *Journal of the American Chemical Society* **125** (2003) 2746.
- [156] Y. Lilach, L. Romm, T. Livneh, et al., *Journal of Physical Chemistry B* **105** (2001) 2736.



---

## Grazie!

Am Ende meiner Doktorarbeit möchte ich mich bei allen bedanken, die meine Arbeit in all den Jahren begleitet haben.

Mein besonderer Dank gilt „dem Chef“, meinem Doktorvater Prof. Joost Wintterlin.

Danke für Deinen Beistand und für Deine Unterweisung in das wissenschaftliche Arbeiten. Ich danke Dir auch für Deine Unterstützung dabei, all die kleinen und großen Probleme im Labor zu lösen, insbesondere beim Einrichten der Geräte damals, nach unserem Umzug von Berlin nach München. Danke dafür, dass Du geduldig Englisch mit mir gesprochen hast, auch wenn ich eigentlich „ins kalte Wasser springen“ und damit anfangen hätte sollen, Deutsch zu sprechen! Danke einfach dafür, dass du ein klasse Chef bist.

Des weiteren geht mein Dank an Dr. Sebastian Günther für die ertragreichen Gespräche und für Deine prompte Hilfe im Labor, wann immer ich diese gebraucht habe. Danke Dir auch für die schnelle Implementierung der IGOR Anwendungen, die für meine Arbeit unentbehrlich waren.

Ich danke Marianne Kardinal und Dr. Stephan Seidler für die Implementierung der Software, die ich für die Raster Tunnel Spektroskopie Messungen und deren Auswertung verwendet habe.

Danke auch an meine früheren und gegenwärtigen Kollegen, Mario, Robert, Sang Hoon und Sebastian, die viel zu der freundlichen Atmosphäre in unserer Arbeitsgruppe beigetragen haben und mich bei meinem (sehr langsamen...) Lernprozess der deutschen Sprache gefördert und unterstützt haben!

Ein besonderes Dankeschön an Dich Enrica, für Deine „italiensiche Kameradschaft“ auf dem 3. Stock des Insitutes für Physikalische Chemie, dafür dass Du in all den Jahren immer ein offenes Ohr für mich hattest und schließlich auch für alle die hilfreichen „Tricks“, um Microsoft Word so zum Laufen zu bringen, wie ich es wollte.

Zum Abschluss möchte ich mich bei all den mir nahestehenden Menschen für ihre moralische Unterstützung und Aufmunterung bedanken.



---

## Curriculum Vitae

Name: Stefano Marchini  
Date of birth: 26.09.1977  
Place of Birth: Casalmaggiore (Cr), Italy

1983-1991 Primary and Secondary Schools “A. De Giovanni”, Sabbioneta (Mn), Italy  
1991-1996 High School “Liceo Scientifico Statale P.A. Maggi”, Viadana (Mn), Italy  
Jul 1996 High School Diploma  
1996-2001 Università degli Studi di Trieste, Trieste, Italy, Studies in Physics  
Dec 2001 Laurea in Physics (Summa cum Laude), University of Trieste  
Diploma work in Surface Physics in the group of Prof. G. Comelli  
Title: “STM study of the interaction between ammonia and nitrogen monoxide on the Pt(111) surface”  
Since Jun 2002 PhD position at the Ludwig Maximilians Universität München, Fakultät für Chemie und Pharmazie, Abteilung Physikalische Chemie, Supervision Prof. Dr. J. Wintterlin.